Czech Technical University in Prague
Faculty of Nuclear Sciences and Physical Engineering

Katedra fyziky
Department of Physics

Studie transportu wolframu pomocí kombinace více diagnostik

Tungsten transport studies via multi-diagnostic approach

MASTER'S THESIS

Vypracoval/author: Bc. Jiří Malinak
Vedoucí práce/supervisor: Dr. Fabien Francis Eric Jaulmes
Rok/year: 2024

ZADÁNÍ DIPLOMOVÉ PRÁCE

I. OSOBNÍ A STUDIJNÍ ÚDAJE

Příjmení: **Malinak** Jméno: **Jiří** Osobní číslo: **486459**

Fakulta/ústav: **Fakulta jaderná a fyzikálně inženýrská**

Zadávající katedra/ústav: **Katedra fyziky**

Studijní program: **Fyzika plazmatu a termojaderné fúze**

II. ÚDAJE K DIPLOMOVÉ PRÁCI

Název diplomové práce:

Studie transportu wolframu pomocí kombinace více diagnostik

Název diplomové práce anglicky:

Tungsten transport studies via multi-diagnostic approach

Pokyny pro vypracování:

Vývoj a fyzikální aplikace nástroje Tomotok (sekce Tokamak, ÚFP AV ČR).
1. Cílem práce je vytvoření nové verze nástroje pro zpracování dat určeného pro ASDEX Upgrade s cílem kombinovat různé bolometrické diagnostiky (SXR, XUV (BLB pro ASDEX Upgrade), rychlé diody XVR pro ASDEX Upgrade), spektroskopii GIW (Grazing Incidence Spectroscopy) a další pro určení hustoty wolframu (W) v radiálním a poloidálním směru. Jedná se tedy o kombinaci fyzikálních a matematických modelů s cílem získat co nejvíce informací.
2. V rámci aplikace budou prozkoumána data získaná při experimentech MST-WPTE-RT03 v letech 2020-2022 na tokamaku ASDEX Upgrade. Cílem je porovnat experimenty s teoretickými modely týkajícími se transportu wolframu (W) ve vysokoteplotním plazmatu.
Na projektu se budou podílet další mezinárodní odborníci na transport W: Alex Jardin a Didier Mazon.

Seznam doporučené literatury:

[1] T. Odstrčil, T. Pütterich, M. Odstrčil et al., ASDEX Upgrade Team Rev. Sci. Instrum. 87, 123505 (2016)
[2] D. Fajardo et al 2022 Plasma Phys. Control. Fusion 64 055017
[3] U. A. Sheikh et al Rev. Sci. Instrum. 93, 113513 (2022); doi: 10.1063/5.0095907

Jméno a pracoviště vedoucí(ho) diplomové práce:

Fabien Francis Eric Jaulmes, Ph.D. Ústav fyziky plazmatu AV ČR, v.v.i.

Jméno a pracoviště druhé(ho) vedoucí(ho) nebo konzultanta(ky) diplomové práce:

RNDr. Jana Brotánková, Ph.D. katedra fyziky FJFI

Datum zadání diplomové práce: **31.10.2023** Termín odevzdání diplomové práce: **10.05.2024**

Platnost zadání diplomové práce: **31.10.2025**

Fabien Francis Eric Jaulmes, Ph.D. podpis vedoucí(ho) práce	podpis vedoucí(ho) ústavu/katedry	doc. Ing. Václav Čuba, Ph.D. podpis děkana(ky)

III. PŘEVZETÍ ZADÁNÍ

Diplomant bere na vědomí, že je povinen vypracovat diplomovou práci samostatně, bez cizí pomoci, s výjimkou poskytnutých konzultací. Seznam použité literatury, jiných pramenů a jmen konzultantů je třeba uvést v diplomové práci.

2. 2. 2024
Datum převzetí zadání

Podpis studenta

ČESKÉ VYSOKÉ UČENÍ TECHNICKÉ V PRAZE
Fakulta jaderná a fyzikálně inženýrská

Břehová 7
115 19 Praha 1

PROHLÁŠENÍ

Já, níže podepsaný

Jméno a příjmení studenta:	Bc. Jiří Malinak
Osobní číslo:	486459
Studijní program:	Fyzika plazmatu a termojaderné fúze
Studijní obor:	-
Specializace:	-

prohlašuji, že jsem diplomovou práci s názvem:

Studie transportu wolframu pomocí kombinace více diagnostik

vypracoval samostatně a uvedl veškeré použité informační zdroje v souladu s Metodickým pokynem o dodržování etických principů při přípravě vysokoškolských závěrečných prací.

Rovněž souhlasím s porovnáním textu mé kvalifikační práce s databází kvalifikačních prací Theses.cz provozovanou Národním registrem vysokoškolských kvalifikačních prací a systémem na odhalování plagiátů.

V Praze dne 04/05/2024

.....

podpis

Acknowledgements

I would like to express my gratitude to my thesis supervisor, Dr. Fabien Jaulmes, for his guidance throughout my thesis preparation. I am also grateful to Dr. Thomas Pütterich for providing the PEC50 data and Dr. Matthias Bernert for providing information on the diagnostics. I would also like to thank Eng. Axel Jardin, Ph.D., Ing. Jakub Svoboda and Ing. M.Sc. Matěj Tomeš, Ph.D. for the feedback.

Bc. Jiří Malinak

Název práce:
Studie transportu wolframu pomocí kombinace více diagnostik

Autor: Bc. Jiří Malinak

Studijní program: Plasma Physics and Thermonuclear Fusion
Obor: -
Druh práce: Master's Thesis

Vedoucí práce: Dr. Fabien Francis Eric Jaulmes
Ústav fyziky plazmatu AV ČR, v. v. i., oddělení Tokamak, Praha
Konzultant: RNDr. Jana Brotánková, Ph.D.
Katedra fyziky, Fakulta jaderná a fyzikálně inženýrská ČVUT v Praze

Abstrakt: Tato práce se věnuje měření a teoretickému popisu transportu wolframu. Je vytvořen nástroj, schopný vypočítat profil hustoty wolframu pro tokamak ASDEX Upgrade. Pro vytvoření tomografických rekonstrukcí je zahrnuta bolometrie, rychlé AXUV diody a kamery měkkého rentgenového záření. Na základě dat z Open ADAS je vytvořen model vyzařování plazmatu, pomocí něhož je vypočítán takzvaný cooling factor. Je analyzována asymetrie profilu vyzařování a jsou diskutovány hypotézy o profilu hustoty. Zpracována jsou data z experimentů s laser blow-off. Z experimentálních dat jsou vypočítány transportní koeficienty dvěma různými metodami. Pomocí modulu FACIT balíčku Aurora jsou vypočítány koeficienty neoklasického transportu. Za určitých předpokladů je provedena simulace transportu a její výstupy jsou srovnány s měřením. Shoda mezi naměřenými koeficienty s teorií je nízká.
Klíčová slova: transport wolframu, bolometrie, cooling factor, čárové záření

Title:
Tungsten transport studies via multi-diagnostic approach

Author: Bc. Jiří Malinak

Abstract: This thesis is focused on the measurement and theoretical description of tungsten transport. A tool capable of calculating the tungsten density profile for the ASDEX Upgrade tokamak is developed. Bolometry, fast AXUV diodes, and soft X-ray cameras are integrated to generate tomographic reconstructions. Based on Open ADAS data, a plasma radiation model is created using which the so-called cooling factor is calculated. The asymmetry of the emissivity profile is analysed, and hypotheses about the density profile are discussed. Data from laser blow-off experiments are processed. The transport coefficients are calculated from the experimental data by two different methods. The neoclassical transport coefficients are obtained using the FACIT submodule of the Aurora package. Under certain assumptions, a transport simulation is performed and its output is compared with the measurements. There is a low agreement between the measured coefficients and the theory.
Key words: tungsten transport, bolometry, cooling factor, line radiation

Contents

List of Figures

Introduction

The continuing global trend of increasing demand for electricity is pushing global society to build new power plants and develop new energy sources. With the increasing living standards in developing countries, the demand for electrical energy is expected to continue to increase. At the same time, ongoing electrification in various sectors, such as transport and heating, will further increase the demand for clean energy.

Simultaneously, changes in Earth's climate caused by human activities, primarily from the burning of fossil fuels, are being observed. One of the contributing factors is the energy sector, particularly fossil fuel power plants. In an effort to reduce or even prevent the resulting greenhouse gas emissions, there is a global trend toward abandoning the burning of fossil fuels and transitioning to green and renewable sources.

However, these sources come with several disadvantages, such as limitations due to geographical location. They are also heavily influenced by current weather conditions, seasons and a day cycle. Consequently, energy production may not always match energy demand, posing significant challenges for energy storage. Furthermore, despite emitting minimal greenhouse gases, they may not always be environmentally friendly.

One solution could be nuclear power plants. Following previous nuclear accidents such as the Three Mile Island, the Chernobyl and Fukushima disasters, which undermined public trust in nuclear technologies, many countries are moving away from nuclear power plants. Another option for utilising nuclear energy does not involve nuclear fission, but rather a process called nuclear fusion.

Like in the Sun, the future fusion power plant will use the energy released by merging light nuclei. The most promising reaction seems to be the fusion of deuterium and tritium through a process called thermonuclear fusion. Nuclear fusion is a low-emission energy source that is inherently safe. The achievement of a nuclear reaction is extremely challenging and any instability will result in the abrupt termination of the reaction. Materials for the fuel production of these power plants are accessible all over the world. In addition, no hazardous nuclear waste is generated during operation. Although it represents a huge technological challenge, it is highly likely that the first generation of fusion power plants will exist by the end of the century. The emergence of many private fusion startups in the last decade shows that fusion is an energy source to be reckoned with in the future.

The most promising concept for a future fusion power plant is the tokamak-type device. In this case, thermonuclear fusion will be achieved in a toroidally shaped plasma, which will be confined by a strong magnetic field. In order to achieve a net energy gain from the fusion reactions, some of the criteria described further below must be met. This means that very high temperatures in the range of 100 to 200

million degrees must be achieved. However, because the density of the plasma is low, the plasma must be kept in a vacuum vessel to separate it from the surrounding environment. Although the plasma is kept in a magnetic field, high requirements will be placed on the so-called plasma facing components. As a first wall material, tungsten was chosen for its capability to withstand high heat fluxes, its low erosion rate, and its other properties. Nevertheless, these fluxes cause sputtering of the tungsten and contamination of the core plasma. The presence of tungsten in the plasma is undesirable and is referred to as an impurity.

A sufficiently high fusion gain factor Q is required for the total energy gain of the future fusion plant:

$$Q = \frac{P_{fus}}{P_{aux}}, \tag{1}$$

where P_{fus} is the temperature dependent fusion power and P_{aux} is the auxiliary heating. For example, for the international project ITER, the world's largest tokamak under construction, a value $Q = 10$ is expected. Another term that plays a role in the energy balance is the plasma losses, specifically the radiated power. This loss term has to be compensated, for example, by external heating, otherwise the plasma will cool down and the reaction will stop. Although bulk plasma radiates naturally through bremsstrahlung, the main concern is the emission of impurities. High-Z impurities, including tungsten, are only partially ionised in the core plasma. As a result, they can emit very intense line radiation. The ability of a given impurity to radiate energy is described by the so-called cooling factor, illustrated in Fig. 1. Here we can see the difference between the low emitting low-Z impurities versus the very high emitting high-Z impurities. Thus, even very small concentrations of tungsten on the order of $c_W = 10^{-4}$ can lead to plasma collapse.

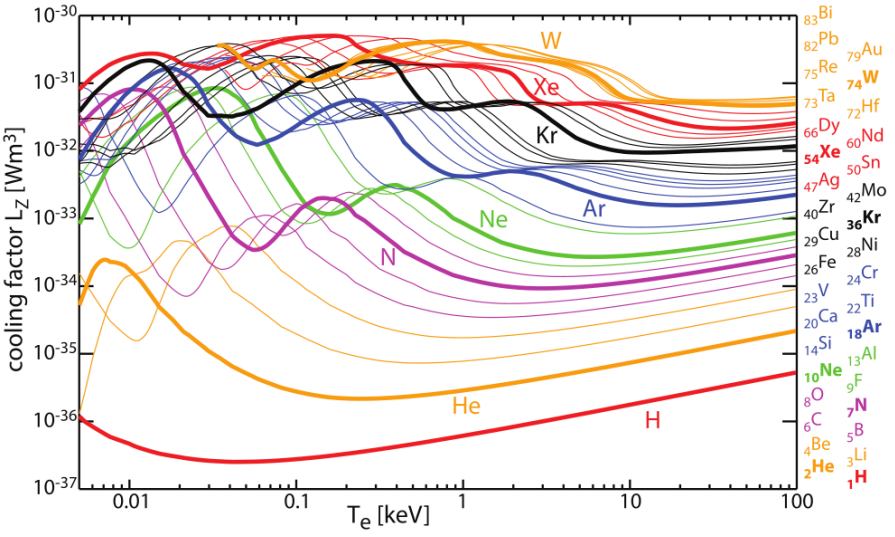

Figure 1: Calculated cooling factors L_Z for various elements as a function of electron temperature T_e at electron density $n_e = 5 \cdot 10^{19}$ m^{-3}. For future fusion power plants, the cooling factor of tungsten is the most important, and unfortunately it is almost the highest. Reprinted from [1].

Thus, it is necessary to somehow prevent the central accumulation of impurities. Clearly, the ability to understand their transport mechanisms is one of the key objectives of current fusion research. A possible way to do this is to develop

diagnostic tools that can be used to evaluate concentrations of, for example, tungsten. This thesis focusses on the development of such tools and their possible use in an experiment.

Chapter 1

Theory

The following chapter describes the theory necessary to understand and measure the transport mechanisms of tungsten on tokamaks. For its description it is essential to obtain the density profile of tungsten, in this thesis from tomography discussed in Sect. 1.6. The reconstructions must be properly interpreted according to the method described in Sect. 2.1.4. In Sect. 1.2.1 the particle orbits influencing the nature of impurity transport described in Sect. 1.7 are described.

1.1 Thermonuclear fusion

In most fusion reactions, two light nuclei merge to form two heavier particles. A reaction in which the final products are lighter than the initial nuclei is called an exothermic reaction. The energy Q released here is proportional to the difference in the binding energy between the initial reactants B_i and the final products B_f:

$$Q = \sum_f B_f - \sum_i B_i, \tag{1.1}$$

where the binding energy B corresponds to the mass difference Δm between the rest of the masses of the nucleons and the nucleus composed of them according to the well-known relation $B = \Delta m c^2$. For the fusion reaction to happen and the energy to be released, it is necessary for the two nuclei to come close enough to overcome the Coulombic barrier. Due to quantum mechanics, the barrier can be overcome by so-called quantum tunnelling, making fusion reactions easier to achieve.

The probability of a given type of reaction between two particles is given by the cross section $\sigma(v)$, which depends on the relative velocity of the particles v. Since the relative velocity of each pair of particles is different, averaged reactivities are introduced:

$$\langle \sigma v \rangle = \int_0^\infty \sigma(v) v f(v) \mathrm{d}v, \tag{1.2}$$

where $f(v)$ is the distribution function of relative velocities, for example, in a thermal plasma the Maxwellian velocity distribution. The reaction of deuterium with tritium (DT) reaches the highest reactivity up to temperature 400 keV:

$$\mathrm{D} + \mathrm{T} \rightarrow {}^4\mathrm{He}\,(3,52\,\mathrm{MeV}) + \mathrm{n}\,(14,07\,\mathrm{MeV}). \tag{1.3}$$

It peaks at temperature 64 keV and in the temperature range 10 to 20 keV it is 100 times higher than the second most probable reaction of deuterium and

deuterium (DD) [2]. For this reason, the most suitable reaction for future fusion power plants is the DT reaction.

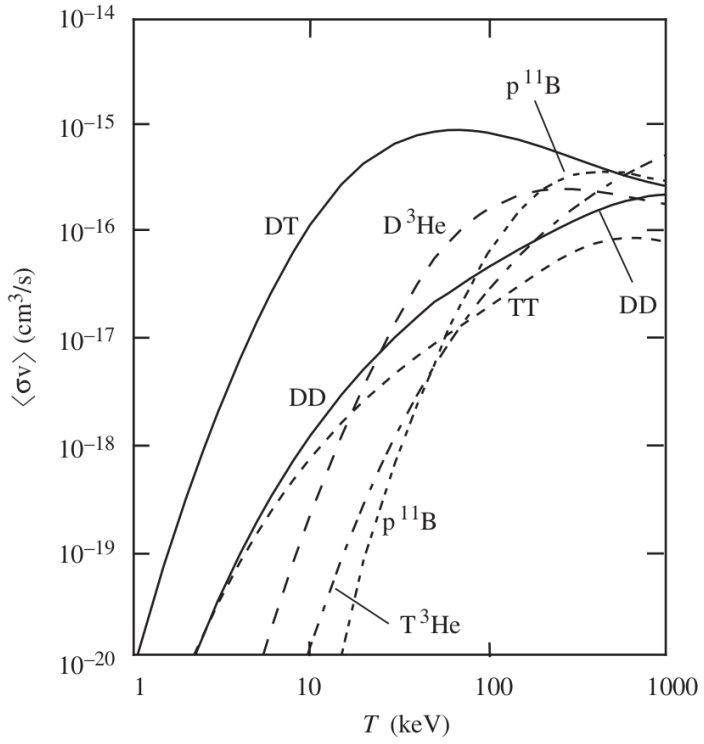

Figure 1.1: Maxwell-averaged reactivities for different fusion reactions as a function of temperature. The most suitable reaction for fusion power plants is DT with the highest reactivity up to 400 keV. Reprinted from [2].

A neutron that is not confined in a magnetic field takes away 4/5 of the energy (14.07 MeV) from the reaction, which it carries away from the plasma. The fast neutrons will stop in the volume of the reactor wall, damaging it in the long term. The remaining 1/5 of the energy (3.52 MeV) in the α-particles remains confined in the plasma that will be heated.

Since deuterium and tritium are hydrogen isotopes, they have a nuclear charge number $Z = 1$. Therefore, their braking radiation is the lowest possible. Deuterium is present in high amounts in the water on Earth. Tritium is almost non-existent in nature, is a beta emitter with a half-life of 12.3 years, and will be produced directly in power plants, for example, from ^{6}Li:

$$^6\mathrm{Li} + \mathrm{n} \rightarrow \mathrm{T} + {}^4\mathrm{He} + 4.8\,\mathrm{MeV}. \tag{1.4}$$

The world's lithium reserves are sufficient to last for thousands of years [3].

1.1.1 Lawson criterion

The remaining question is what the fuel parameters must be for the energy gain from the fusion reaction. Conditions under which the energy released in a fusion reactor is higher than the energy required to heat the fuel are described by the Lawson criterion. Thus, it is mostly the energy balance of the plasma:

$$\frac{\mathrm{d}W_p}{\mathrm{d}t} = P_{aux} + P_\alpha - P_{rad} - P_{trans}. \tag{1.5}$$

An increase in the internal kinetic energy of the plasma occurs if the external heating P_{aux} and the heating of the α particles from the fusion reaction P_α overcome the loss terms due to radiation P_{rad} and other transport processes P_{trans}. When the so-called ignition is reached, the plasma heating by fusion reactions and the plasma loss power are balanced. For the reaction chosen from deuterium and tritium in the temperature region around $T = 14$ keV, an inequality can be derived:

$$nT\tau_E \geq 3 \cdot 10^{21}\ \mathrm{keV\,s\,m^{-3}}. \tag{1.6}$$

where τ_E is the confinement time, which describes how the plasma loses energy W [4, 5]:

$$\tau_E = \frac{W}{P_{loss}} \tag{1.7}$$

This condition can be met in several ways. One possibility is to choose high values of plasma density with a short confinement time. This approach is called inertial fusion and is typically done using powerful lasers that heat and compress the target in the form of a pellet. The second option, the most promising for a future power plant, is magnetic confinement, where the plasma is confined by a magnetic field created by external coils and with the current generated in the plasma.

Since in magnetic confinement the maximum plasma density is constrained by the Greenwald limit and the maximum plasma temperature is given by the fuel cross sections, the main way to meet the Lawson criterion is to increase the confinement time τ_E. This can be achieved by decreasing the loss terms in the power balance.

1.2 Tokamaks

Tokamaks are devices used for plasma confinement, mainly to achieve thermonuclear temperatures and energy production via thermonuclear fusion. Currently, they are the most advanced thermonuclear fusion devices in terms of energy confinement time. Tokamaks are axisymmetric devices based on plasma confinement using a high toroidal magnetic field and a low toroidal current.

In the case of no collisions, electrically charged particles are confined in a direction perpendicular to the magnetic field, while in a direction parallel to the magnetic field they can move freely. To trap the plasma, the magnetic field lines in the tokamaks are closed. The toroidal magnetic field B_φ is generated by external coils winded around the toroidal chamber of the tokamak and depends on the distance from the symmetry axis $B_\varphi \sim 1/R$. The resulting vertical drift leads to charge separation, leading to a drift of $\vec{E} \times \vec{B}$. The plasma is thus unstable, and a poloidal field B_θ must be introduced, resulting in a helical magnetic field. This is characterised by the safety factor q, defined by the toroidal magnetic flux Φ and the poloidal magnetic flux ψ:

$$q(r) = \frac{\mathrm{d}\Phi}{\mathrm{d}\psi} \approx \frac{rB_\varphi}{R_0 B_\theta}, \tag{1.8}$$

where R_0 is the major radius and the radius of the outermost surface $r = a$ is called the minor radius. The machine and its plasma are characterised by the inverse

aspect ratio $\varepsilon = r/R_0$. Magnetic field lines follow helical paths and form magnetic surfaces, which are at the same time surfaces of constant pressure $\vec{B} \cdot \nabla p = 0$. The poloidal magnetic field is generated in tokamaks by the plasma current I_p. This is generated by a toroidal electric field induced by a transformer. It is created by the time variation of the magnetic flux that passes through the torus [6]. In addition to stability, the plasma current serves as heating of the plasma via Ohmic heating. For higher plasma temperatures, Ohmic heating is insufficient, and additional heating is necessary. This can be neutral beam injection (NBI), electron cyclotron resonance heating (ECRH), and ion cyclotron resonance heating (ICRH).

The most important tokamak today is the international ITER project that is being constructed in southern France. Its goal is the technological demonstration of a large fusion reactor and the achievement of a fusion energy gain factor $Q \geq 10$. With its magnetic field $B \approx 5.3$ T and major radius $R_0 = 6.2$ m, it will be the largest tokamak ever built.

Another important European tokamak is the ASDEX Upgrade tokamak, located in Garching, Germany. Its purpose is to prepare the physics base for ITER. The data used in this thesis are obtained from experiments conducted on this tokamak. Its parameters are $B \approx 3.1$ T, the major radius $R_0 = 1.65$ m, and the minor radius $a = 0.4$ m. It is equipped with an all-tungsten first wall and NBI, ICRH, and ECRH type external plasma heating systems.

The Czech Republic also has two tokamaks. The first is a small tokamak GOLEM operated by FNSPE CTU. It serves mainly for educational purposes to students from all over the world via remote control. The second tokamak is the currently constructed COMPASS Upgrade tokamak. It will have ITER relevant geometry, high magnetic field, and one of its objectives is to study a high-density divertor.

1.2.1 Particle orbits

For the cyclotron motion alone, the guiding centres of the charged particles will follow the magnetic field lines, whereas the particles themselves will be up to a Larmor radius ρ_L away from the magnetic surfaces. After taking into account the gradient and curvature of the toroidal magnetic field, guiding centre drifts occur. The guiding centres of the particles now follow the surfaces that are shifted with respect to the magnetic surfaces. This phenomenon is important in describing particle transport in plasmas.

Now the toroidal magnetic field $B_\varphi \sim 1/R$ and the collisionless situation are considered. Particles with a sufficient parallel velocity $v_\parallel$ to the magnetic field to complete the circular motion in the poloidal direction are called passing particles. Due to the effect of vertical drift v_d, their guiding centres are shifted by a distance d:

$$|d| = \left|\frac{v_d}{\omega}\right| \sim q\rho_L. \tag{1.9}$$

The magnetic field increases when moving along magnetic flux surfaces towards the high-field side (HFS). As the particle moves into the high magnetic field, its $v_\parallel$ decreases. If the particle has a kinetic energy $E \leq \mu B_{max}$ and therefore a small parallel velocity $v_\parallel$, it is reflected from the high magnetic field, and magnetic mirror reflection occurs. A periodic motion emerges, shaped like a banana in a poloidal

cross section. Such particles are called trapped particles. These banana orbits have a width Δ_b in the large aspect ratio limit (Ref. [7]):

$$\Delta_b \sim \frac{q}{\sqrt{\varepsilon}}\rho_L, \tag{1.10}$$

and reflects with bounce frequency ν_b (Ref. [6]):

$$\nu_b = \sqrt{\frac{\varepsilon}{2}}\frac{v_\perp}{2\pi q R_0}. \tag{1.11}$$

For the perpendicular velocity, this applies $v_\perp = \sqrt{2}v_{th}$, where v_{th} is the thermal velocity. The width of the banana orbit is wider than the shift of the passing particle's trajectory, so it can play a significant role in particle transport. Through collisions, particles can move between different orbits. The trapping condition determines whether a given particle is passing or trapped. Trapped particles have a velocity in the loss cone:

$$\left.\frac{v_\parallel^2}{v_\perp^2}\right|_{\theta=0} \leq 2\varepsilon. \tag{1.12}$$

Their total number can be found from the isotropic Maxwellian distribution function and is approximately $f_t \simeq \sqrt{2\varepsilon}$ [5]. Through collisions, trapped particles move from the loss cone to the passing particle region. In the velocity space, diffusion occurs, which is characterised by the effective collision frequency for detrapping ν_{eff}:

$$\nu_{eff} \approx \frac{\nu_{coll}}{2\varepsilon}, \tag{1.13}$$

where ν_{coll} is the collision frequency described in Sect. 1.7.

1.2.2 Coordinates

Since toroidal geometry is the key concept for most descriptions of plasma confinement, a suitable coordinate system must be chosen. The most basic are the cylindrical coordinates (R, ϕ, z), where R points away from the major axis, z points upward in its direction, and ϕ is mathematically positive from the top view. The coordinate (R, z) gives the poloidal plane of the tokamak and the symmetry in the toroidal direction ϕ is assumed.

With the magnetic field lines lying on toroidal surfaces, canonical coordinates can be taken. The poloidal flux is given by the magnetic field passing through a surface S perpendicular to the axis of symmetry and enclosed by a point in the (R, z) plane:

$$2\pi\psi = \int_S B_\theta \cdot \mathrm{d}S. \tag{1.14}$$

In magnetic coordinates, the poloidal flux is just a function of the toroidal flux, and the magnetic surfaces are given by $\psi(R, \phi, z) = const$. Thus, all magnetic field lines lie on these magnetic surfaces, i.e. $\nabla\psi \cdot B = 0$. Now we can index the individual magnetic flux surfaces.

We can introduce the coordinates (r, θ, ϕ), where r is the local minor radius and θ the poloidal angle. For more complex geometry, such a radius $[r] =$ m can

be defined as the radius of a circle that surrounds the same surface S in a poloidal cross section:

$$r = \sqrt{\frac{S}{\pi}}. \tag{1.15}$$

Thus, the normalised effective minor radius $[\rho] = 1$ is introduced:

$$\rho = \frac{r}{r_{max}}, \tag{1.16}$$

where r is the mean effective minor radius of the magnetic flux surface and r_{max} of the last closed flux surface [8, 9]. It is also possible to introduce the normalised flux coordinates ρ_{pol} based on the normalised poloidal flux ψ_N:

$$\rho_{pol} = \sqrt{\psi_N} = \sqrt{\frac{\psi - \psi_{core}}{\psi_{LCFS} - \psi_{core}}} \tag{1.17}$$

and similarly ρ_{tor} for the normalised toroidal flux Φ_N:

$$\rho_{tor} = \sqrt{\Phi_N}, \tag{1.18}$$

where ρ_{tor} best describes the edge of the plasma from the mentioned coordinates ρ, ρ_{tor} and ρ_{pol}. They are identical for circular geometry [10].

1.2.3 Impurities

Impurities in tokamak-type thermonuclear reactors originate mainly from the plasma-wall interaction (PWI). As a result of the transport processes, impurities reach the core plasma, where they may accumulate. This occurs in both the limiter and divertor configurations. While in the limiter configuration the last closed flux surface (LCFS) is determined by the limiter surface, in the divertor configuration the LCFS is determined by the magnetic field. This is created by a conductor under the tokamak chamber, which creates the X-point, the point where there is a null in the poloidal field. Thus, there is a separation of the open and closed magnetic field lines and hence a separation of the main plasma from the wall by a boundary called the separatrix. Also in the vicinity of the X-point there is an increase in the length of the field lines that the particles must cross to pass over the separatrix.

The plasma is diverted to the divertor target, and the plasma-wall interaction is therefore distant from the core plasma. Due to the high heat flux, erosion, such as sputtering, occurs on the target plate. The released impurities are immediately ionised after exiting the wall and can be carried back to the divertor by the flow. Impurities from the residual plasma wall interaction are also ionised in the scrape-off layer (SOL) and guided along the magnetic field lines to the divertor. Another source of impurities is the helium ash from the fusion reaction. It mainly dilutes the fuel and one of the tasks of the divertor is to remove it [6].

Plasma low-Z impurities dilute the fusion fuel and in addition high-Z impurities cause radiation losses. As they move towards the plasma centre, they enter regions with increasing temperature. The neutral atoms are thus ionised to high-ionisation states. The fully ionised low-Z ions in the core cause radiative cooling through Bremsstrahlung. The heavy ions with $Z \geq 40$ are not fully ionised even at fusion temperatures; thus, the centre of the plasma radiates with line radiation, which is

more important for high-Z. A comparison of the cooling factors for various Z is shown in Fig. 1. For this reason, it is very important to understand the transport mechanisms of high-Z impurities.

1.3 Ionisation balance

Knowledge of ionisation equilibrium is very important for the study of plasma radiation. For each state, there is an equation:

$$\frac{\mathrm{d}n_{I,Z}}{\mathrm{d}t} = \Lambda_{I,Z} + R_{source} - R_{sinks}, \tag{1.19}$$

where R_{source} and R_{sinks} represent all positive and negative contributions of a given state. The term $\Lambda_{I,Z}$ is the flux of a given population by diffusion and convection. The populations are assumed to reach steady state faster than the plasma conditions change. Therefore, the temporal change is assumed to be zero $\frac{\mathrm{d}n_{I,Z}}{\mathrm{d}t} = 0$. The same can also be said for the flux $\Lambda_{I,Z}$. These assumptions are wrong for metastable and ground states. This means that this assumption may not be correct for the application in this work [11].

For low plasma densities, the coronal equilibrium model (CE) can be used. The main idea of this model is that all transitions to higher states are driven by collisional processes, whereas transitions to lower states are via radiative processes. The so-called Coronal approximation also states that all excitation is done from the ground state [1]. This approximation can be justified by the fact that the radiation density is low. For optically thin plasmas, most photons escape and thus no absorption occurs. At the same time, since the electron density is low and spontaneous decay does not depend on it, collisional deexcitation becomes negligible [12].

Since in tokamaks the assumptions for coronal equilibrium (CE) are generally not satisfied, a collisional radiative (CR) model has to be chosen. In the CR model, additional excitation channels via metastable states are already considered, which can account for a substantial part of the ion population and thus affect the total radiated power. The CR model thus includes the rate equations for each state [1]. In it, for the excited states, electron collisional transitions and radiative decay are taken into account. Furthermore, collisional processes are taken into account, namely electron impact ionisation, three-body recombination, and dielectronic and radiative recombination.

Radiative recombination occurs when an electron collides with an ion, trapping the electron and radiating energy, which is given by the kinetic energy of the electron and the energy of the bound state.

$$A^{(Z+1)+} + e^- \rightarrow A^{Z+} + h\nu \tag{1.20}$$

Dielectronic recombination is a two-step process in which an electron is resonantly captured in a doubly excited state. The second step is decay to a lower excited state, and thus emission of radiation.

$$A^{(Z+1)+} + e^- \rightarrow \left(A^{Z+}\right)^{**} \rightarrow A^{Z+} + h\nu \tag{1.21}$$

Electron impact ionisation is caused by the collision of an electron with an ion. The kinetic energy of the electron is transferred to another bound electron, which goes into a free state. The ion enters the ground state of the next ionisation stage.

$$A^{Z+} + e^- \rightarrow A^{(Z+1)+} + e^- + e^- \tag{1.22}$$

Naturally, these processes also have inverse processes, i.e. the arrows can be in both directions. The inverse process of electron impact ionisation is a three-body recombination. This must already be included for higher electron densities [11]. By introducing generalised ionisation and recombination coefficients, one can extend the applicability of the coronal model [12].

For calculating equilibrium ionisation balance fractional abundances, the generalised collisional radiative coefficients provided by the Open ADAS database (Ref. [13]) in the ADF11 files are used. The procedure for their derivation is described, for example, in Ref. [14]. They are computed from several semiempirical formulas using generalised collision-radiative (GCR) models. The suffix CD here means that dielectronic recombination is included. The tabulated coefficients for α_{CD} recombination and S_{CD} ionisation of the 50 series are used. Both are functions of temperature and density, and therefore the tabulated values must be interpolated.

Effective ionisation coefficients S_{CD} include electron impact ionisation and, in addition, excitation autoionization. Effective recombination coefficients α_{CD} include dielectronic recombination and radiative recombination. To find the equilibrium, a system of equations [15] must be solved:

$$\frac{\mathrm{d}n^{(i)}}{\mathrm{d}t} = n_e \left[S_{cd}^{(i-1,i)} n^{(i-1)} + \alpha_{cd}^{(i+1,i)} n^{(i+1)} - S_{cd}^{(i,i+1)} n^{(i)} - \alpha_{cd}^{(i,i-1)} n^{(i)} \right]. \tag{1.23}$$

The quasi-steady state is assumed to be acquired very quickly, and therefore $\frac{\mathrm{d}n^{(i)}}{\mathrm{d}t} = 0$ is considered. The following relations can be easily derived:

$$n^{(i)} = \frac{\alpha_{cd}^{(i+1,i)}}{S_{cd}^{(i,i+1)}} n^{(i+1)} \tag{1.24}$$

The ionisation equilibrium is independent of the electron density and proportional to the rate coefficients. The fractional abundance $f_i = \mathrm{FA}_i$ is introduced, which expresses the fraction of a given state with respect to all present states of the same species:

$$f_i = \frac{n^{(i)}}{\sum_i n^{(i)}} \tag{1.25}$$

The system of equations can be solved by rewriting it in matrix form:

$$\begin{pmatrix} f_0 \\ f_1 \\ \vdots \\ f_{n-1} \\ f_n \end{pmatrix} = \begin{pmatrix} 0 & \alpha_{cd}^{(1,0)}/S_{cd}^{(0,1)} & 0 & \cdots & 0 \\ 0 & 0 & \alpha_{cd}^{(2,1)}/S_{cd}^{(1,2)} & \cdots & 0 \\ \vdots & \vdots & \vdots & \ddots & \vdots \\ 0 & 0 & 0 & \cdots & \alpha_{cd}^{(n,n-1)}/S_{cd}^{(n-1,n)} \\ -1 & -1 & -1 & \cdots & 0 \end{pmatrix} \cdot \begin{pmatrix} f_0 \\ f_1 \\ \vdots \\ f_{n-1} \\ f_n \end{pmatrix} + \begin{pmatrix} 0 \\ 0 \\ \vdots \\ 0 \\ 1 \end{pmatrix} \tag{1.26}$$

where the matrix is denoted as $\mathbb{M}$:

$$\vec{f} = \mathbb{M} \cdot \vec{f} + \vec{b} \tag{1.27}$$

and by inversion the ionisation fractional abundances $\vec{f}$ for the individual states are found:

$$\vec{f} = (\mathbb{I} - \mathbb{M})^{-1} \cdot \vec{b} \tag{1.28}$$

1.4 Radiative Processes

Every plasma emits electromagnetic radiation in different regions of the spectrum. The following part of this thesis focusses on the different types of radiation caused by electron transitions. The first of these is the bound-bound transition, also known as line radiation, caused by the transitions of bounded electrons between the levels of atoms with, ideally, a discrete spectrum. The transition between free and bound states is known as free-bound or recombination radiation and is characterised by a continuum with an edge. The last type is braking radiation, better known as bremsstrahlung or as a free-free transition. Each of these processes has an opposite process, in which radiation is absorbed. As will be discussed later, such a case is not considered in tokamak plasma.

1.4.1 Line emission

The working gas and the impurities mostly in the plasma radiate because of the transition of electrons between energy levels. If it is a bonded-bonded type transition, the radiation will be in the form of narrow spectral lines. This radiation will be very different for different types of ions and their ionisation states and will be determined by their energy level structure.

Let us consider an atom with two energy levels i and j and one bonded electron. Now there can be in total three radiative transitions between these levels. For the purposes of this work, the most important is spontaneous decay, which can be described in the following relation from left to right:

$$\left(A^{Z+}\right)^* \rightleftarrows A^{Z+} + h\nu \tag{1.29}$$

If the electron is in the excited state at the higher level, a spontaneous decay to the lower level can occur by emitting a photon ν_{ij} of energy equal to the energy difference of the two levels E_i and E_j:

$$h\nu_{ij} = \Delta E = E_i - E_j. \tag{1.30}$$

Photon emission is associated with each individual transition, which is determined by the atomic transition probability also known as the Einstein coefficient for spontaneous emission A_{ji}:

$$\varepsilon_{ji}^{bb} = \frac{h\nu_{ij}}{4\pi} A_{ji} n_j, \tag{1.31}$$

where n_j is the population density of the excited state j. To determine the total emission, the sum of all the rates for each of the processes populating the state j must be calculated [11].

To calculate the emissivity of the spectral line ε_{ji}^{bb} from state j to state i, the photon emissivity coefficient $\mathrm{PEC}_{ji}(T_e, n_e)$ is used [12]. This is a temperature and density dependent function, and in this work the values tabulated in the Open ADAS database are used, Ref. [13]. The photon emissivity coefficient of the spectral line ε_{ji}^{bb} can be calculated assuming that n_Z is the density of the emitting ionisation stage Z of the species I. Thus, $n_{I,Z} = f_Z \cdot n_I$ where f_Z is the local fractional abundance. Then we can compute ε_{ji}^{bb} as [16]:

$$\varepsilon_{ji}^{bb} = n_e n_Z \mathrm{PEC}_{ji}^{Z}(T_e, n_e) \tag{1.32}$$

1.4.2 Bremsstrahlung

Radiation from electron-ion encounters, called bremsstrahlung (German word for braking radiation), is emitted when an electron is accelerated in the electric field of an ion. Radiation originating from the interaction of a pair of free electrons is neglected for non-relativistic velocities because there is no overall acceleration of the centre of gravity. There is also an inverse process, and it is called inverse-bremsstrahlung:

$$A^{Z+} + e^- \rightleftarrows A^{Z+} + e^- + h\nu \tag{1.33}$$

In tokamaks, bremsstrahlung is one of the dominant sources in the soft X-ray range and has a continuous spectrum. Unlike other types of radiation, even fully ionised ions can emit it.

In the following section, the derivation for bremsstrahlung is only hinted at, since it is not the subject of this thesis. The classical bremsstrahlung is presented here, which will be subsequently modified using the Gaunt factor to quantum-mechanical bremsstrahlung. The solution is based on the description of the trajectory of an incoming particle, i.e. an electron with velocity v towards an ion with charge Ze, which interacts via the Coulomb field. First, a description of the parabolic trajectory without radiation loss is given by the impact parameter b. Then the radiated power for a given relative velocity is derived. A formula integrated over the solid angle can be used to calculate the radiation from the encounter, since in the following steps we will consider an isotropic electron distribution. The law of conservation of energy in collision is used and since we want to determine the radiation of one electron in a system of some density n_i, we multiply by the product of density and velocity. This collision is still determined by the choice of the collision parameter b, so to determine the total power it is necessary to integrate over the collision parameter. Integration leads to the so-called Hankel function of the first kind $H(x)$ in factor $G(u)$. In the resulting integrated relation, it appears as a function u_{90}, which is the nondimensionalized frequency for the impact parameter b_{90} for $\pi/2$ scattering:

$$\frac{\mathrm{d}P}{\mathrm{d}\nu} = \frac{Z^2 e^6}{(4\pi\varepsilon_0)^3} \frac{32\pi^2}{3\sqrt{3}} \frac{n_i}{m^2 c^3 v} \cdot G(u_{90}) \tag{1.34}$$

Because radiation emission is highest when the electron is at the closest point to the ion on its trajectory, a peak in the spectrum of the emitted energy can be derived. For practical use, approximations are made for high and low frequency. If the collision parameter is much larger than b_{90}, we speak of a straight-line collision, and it is the

low-frequency regime. If it is smaller than b_{90}, it is closer to the ion and the trajectory is more parabolic. These approximations give the shape of the approximated Gaunt factor G^{ff}. For low frequencies, $G^{ff} > 1$, while for high frequencies the Gaunt factor converges to $G^{ff} = 1$ [12]. Non-relativistic quantum derivation of the Gaunt factor leads to solutions with hypergeometric functions and is simplified using the Born approximation.

To obtain the radiated power from the plasma in thermal equilibrium, one needs to integrate over the distribution function. Considering the Maxwell-Boltzmann distribution, the resulting spectral emissivity $[\varepsilon] = \mathrm{W} \cdot \mathrm{m}^{-3} \cdot \mathrm{eV}^{-1}$ emerges:

$$\begin{aligned} \varepsilon_Z^{ff}(E) &= \left[\frac{32\sqrt{\pi}(\alpha a_0)^3 E_R}{3\sqrt{3}hc}\right] n_e n_Z Z^2 \frac{G^{ff}}{\sqrt{T_e}} \exp\left(-\frac{E}{T_e}\right) \\ &= 1.54 \cdot 10^{-38}\, n_e n_Z Z^2 \frac{G^{ff}}{\sqrt{T_e}} \exp\left(-\frac{E}{T_e}\right) \end{aligned} \tag{1.35}$$

It is also possible to estimate the emission of the braking radiation for the effective charge Z_{eff}:

$$Z_{eff} = \frac{\sum_s Z_s^2 n_s}{\sum_s Z_s n_s}, \tag{1.36}$$

where we need to replace $n_Z Z^2$ with $n_e Z_{eff}$ [11]. In this work, the tabulated values in Ref. [17] were used, which are applied, for example, in the Cherab code. These are temperature-averaged Gaunt factors that have been interpolated.

1.4.3 Radiative recombination

Recombination radiation is produced by the capture of a free electron with kinetic energy E_{kin} to the bound excited state j. The photon of energy $h\nu$ is emitted:

$$A^{(Z+1)+} + e^- \rightleftarrows A^{Z+}(j) + h\nu. \tag{1.37}$$

This is given by the kinetic energy of the free electron and the ionisation potential of the final bound state j:

$$h\nu = E_{kin} + [E(\infty) - E(j)]\,. \tag{1.38}$$

Because the electron energy distribution function is continuous, the recombination radiation is also continuous. However, since the atomic-level structure is discrete, the recombination radiation is discontinuous.

The cross section for recombination can be calculated on the basis of the inverse process, i.e. from photoionisation. In the case of semiclassical calculations, the transition from a bound state described as an elliptical orbit to a free state described as a hyperbolic orbit can be assumed. Thus, a sharp threshold frequency for ionisation can be obtained. Similarly to the case of braking radiation, an analytical formula can be derived for the spectral emission coefficient of radiative recombination $\varepsilon_Z^{fb}(h\nu)$. Here, the so-called bound-free Gaunt factor G^{bf} appears and, in contrast to bremsstrahlung, the characteristic edge structure of the spectrum has to be considered [11].

In this work, the emission coefficient of radiative recombination is not calculated, but tabulated data are used. The first source is the Open ADAS database;

see Ref. [13]. The coefficients for recombination-bremsstrahlung PRB(T_e, n_e) are used, specifically from the PRB50 series for tungsten. Both radiative recombination and dielectronic recombination are included. It also includes the contribution of Bremsstrahlung, which is considered hydrogenic, with a Gaunt factor of unity of [14].

The second source is tabulated data from Ref. [18]. The coefficient used is $C_{rb}(T_e)$, which is the cooling factor for radiation due to recombination including bremsstrahlung. An approximation using the value $f_{rec-rad} = 1.2$ is used to calculate the radiation emitted by recombination. The cooling factor for radiative recombination is then calculated as the product of $f_{rec-rad}$ times the ionisation potential times the recombination rate A_{cd}.

1.4.4 Cooling factor

The total spectral emissivity ε_I of a given species I is equal to the sum of the spectral emissivities of all types of emission of individual ionisation states Z. The ε_I includes the bound-bound $\varepsilon^{bb}_{I,Z}$, free-bound $\varepsilon^{fb}_{I,Z}$ and free-free $\varepsilon^{ff}_{I,Z}$ types of radiation:

$$\varepsilon_I(h\nu) = \sum_{Z=0} \left[\varepsilon^{bb}_{I,Z}(h\nu) + \varepsilon^{fb}_{I,Z}(h\nu) + \varepsilon^{ff}_{I,Z}(h\nu)\right] \tag{1.39}$$

The spectral emissivity ($[\varepsilon] = \mathrm{W \cdot m^{-3} \cdot eV^{-1}}$) is measured by the detector with spectral response $0 \leq \eta(h\nu) \leq 1$ as the observed filtered emissivity Σ^η, ($[\Sigma^\eta] = \mathrm{W \cdot m^{-3}}$):

$$\Sigma^\eta = \int \eta(h\nu)\varepsilon(h\nu)\mathrm{d}h\nu \tag{1.40}$$

The total radiated power density Σ_I of species I can be interpreted using the cooling factor L_I ($[L_I] = \mathrm{W \cdot m^3}$) [16]:

$$\Sigma_I = n_e n_I L_I(T_e, n_e), \tag{1.41}$$

where $L_I(T_e, n_e)$ is a function of temperature and density. For tungsten, the dependence of L_W on temperature is considered low in the region relevant for bolometric cameras on the AUG tokamak. In the shots processed in this work, no seeding is used, and therefore only hydrogen plasma with only tungsten impurities can be considered. Then, the total radiated power density is:

$$\Sigma^\eta = n_e^2 \left[L^\eta_H(T_e) + c_W \cdot L^\eta_W(T_e)\right]. \tag{1.42}$$

From the measurement of the radiated power, the knowledge of the cooling factors and the electron density and temperature, the concentration of tungsten c_W can be found [15]:

$$c_W \approx \frac{\Sigma^\eta - L^\eta_H(T_e) \cdot n_e^2}{L^\eta_W(T_e) \cdot n_e^2} \tag{1.43}$$

In this thesis, the tabulated values of the cooling factor L_W are used from the article Ref. [18]. For level-resolved calculations of the cooling factor of the line radiation, the Cowan code was used. The collisional radiative model and configuration averaged calculations (CA) were used. For some ionisation states, the computational demands are too large to perform level-resolved (LR) calculations,

and thus the calculations have to be performed with sets of configurations. The total cooling factor L_W includes the recombination and bremsstrahlung radiation from C_{rb}.

The second source of tabulated values is the article Ref. [19]. This contains polynomial fit coefficients for calculating the cooling factors of various elements, including tungsten. An average-ion model was used for the calculations, which replaces the different ionic species for each element by a single fictitious average ion. The latter is the average of all possible charge states of the element. In addition to the line radiation, the emission from bremsstrahlung, radiative recombination, and dielectronic recombination are included.

1.5 Detectors

A direct way to determine the total radiation loss of the plasma is to use a radiative bolometer. Bolometers measure radiation in a wide range of spectra from the visible to the soft X-rays. Specifically, they measure the total escaping energy flux (or irradiance flux density $[E] = \mathrm{W} \cdot \mathrm{m}^{-2}$) preferably with a uniform spectral response. This in order to allow an absolutely calibrated measurement [12]. However, that means that no spectral information can be obtained from them.

The majority of the power is radiated from the divertor region, where most of the atoms are partially ionised due to the relatively low temperature of the order 10 to 100 eV. Therefore, the ions effectively radiate in the vacuum ultraviolet (VUV) region, that is, in the region of 5 to 100 eV. Similarly, the scrape off layer (SOL) also radiates in the VUV region. In the core plasma, the temperature is already much higher and the emission is primarily from the soft X-ray region, i.e. 100 eV to 3000 eV [20]. The sensitivity of the detectors to different photon energies is called the efficiency $\eta(h\nu)$ ($[\eta] = 1$) or the spectral response and is defined as the ratio of the signal power P_{bolo} to the radiant flux (or power) P_0:

$$\eta = \frac{P_{bolo}}{P_0}. \tag{1.44}$$

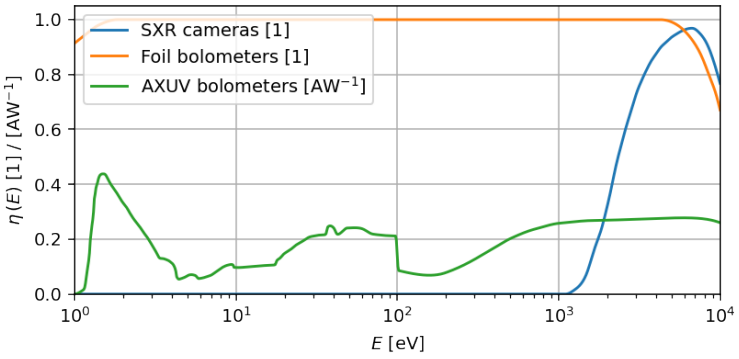

Figure 1.2: Detection probability for SXR camera, spectral responsivity for AXUV diodes and efficiency for foil bolometers.

1.5.1 Foil bolometer

A common type of bolometer used on many tokamaks is the foil bolometer, which consists of a thin foil (on AUG 4.5 μm thick) from a chemically inert metal such as gold or platinum. This is placed on a substrate of mica, Kapton, or SiN-membranes. Photons hit the foil on the front side, heating it up, and this is then measured by the change in resistivity on the back side [21].

A characteristic of foil bolometers is the almost constant spectral response. It is only limited by the reflectivity of the metal for photons with low energy ≤ 1 eV and the transmission of photons with high energy ≥ 8 keV through the foil. Due to the linear response to the photon energy, the foil bolometers can be absolutely calibrated. The upper limit of the spectral sensitivity curve is given by the absorber thickness and is based on measurements in Ref. [21] for a similar platinum bolometer with the same absorber thickness of 4.5 μm. The assumption was made that the sensitivity for both types has a similar shape and, in addition, that it is equal to one in the main region of the spectrum [22]. To reduce the lower limit, the bolometer is improved with carbon-coated gold absorber, which reduces the lower limit to 1 eV. The resulting spectral response curve is plotted in Fig. 1.2.

However, the time resolution is on the order of a few milliseconds because of the principle described above. The resolution limit is given by the heat transport time within the detector. However, the time scales of the events in a tokamak plasma are shorter, and therefore a replacement for this type of detector must be found.

1.5.2 AXUV bolometer

The second option to measure the total radiated power is to use diodes based on the AXUV (Absolute eXtended UltraViolet). They are based on the formation of electron-hole pairs in the active regions when a photon hits the diode. This type of diode is specifically designed to be sensitive even in the VUV region. In addition to photons, they can also be sensitive to electrons, ions, and neutrons, which create parasitic currents. They can achieve resolutions down to a few microseconds, but at the cost of absolute calibration capability. The dependence on radiation wavelength is not linear, and their sensitivity decreases very rapidly.

The sensitivity decrease is described in Ref. [20] and occurs already during the first 50 s of operation. After a degradation by a factor of 2.5 of the original value, which occurs after 300 s, no further degradation occurs. The resulting spectral response curve was obtained by combining the manufacturer's data with the measured values in Ref. [20] and is plotted in Fig. 1.2. The curve does not include the strong decrease in the VUV region, which was not measured. Because the drop in sensitivity no longer changes, AXUV bolometers can be calibrated using foil bolometers. An example of such a procedure is RADCAM [23] combining three different types of diagnostics.

1.5.3 SXR cameras

Soft X-ray cameras observe plasma in the region 100 eV to 10 keV only. They measure the integrated total radiated power similar to bolometers, except that a beryllium filter foil 75 μm thick is placed in front of the diode. This blocks photons up to 1 keV and together with the diode parameters gives the spectral

response or detection probability $\eta(h\nu)$. In this region of the spectrum, only heavy impurities, such as tungsten, produce line radiation. Light impurities emit only via continuous radiation, and this radiation is often exceeded by line radiation. Like bolometers, these detectors work on the pinhole camera principle, except that the pinhole contains the previously mentioned beryllium filter.

The low limit for photon detection is given by the thickness of the beryllium foil d_{Be}. The upper limit is, as for AXUV diodes, given by the thickness of the active layer d_{active} of the silicon diode. This thickness can be less than the thickness of the diode itself. Furthermore, the radiation passes through the passivation layer $d_{Si_3N_4}$ and the dead layer d_{dead}. The calculation of the detection probability can be given by the expression:

$$\eta(h\nu) = \exp(-\mu_{Be}d_{Be} - \mu_{Si}d_{dead} - \mu_{Si_3N_4}d_{Si_3N_4}) \cdot (1 - \exp(-\mu_{Si}d_{active})), \quad (1.45)$$

where the thickness of the active layer $d_{active} = 200\ \mu$m was chosen. The spectral response can also be affected by the impact of photons at large angles. This contribution can be neglected, since only photons outside the camera sensitivity range are affected. Again, the spectral response is plotted in Fig. 1.2. The sampling frequency of the acquisition system is 2 MHz [24].

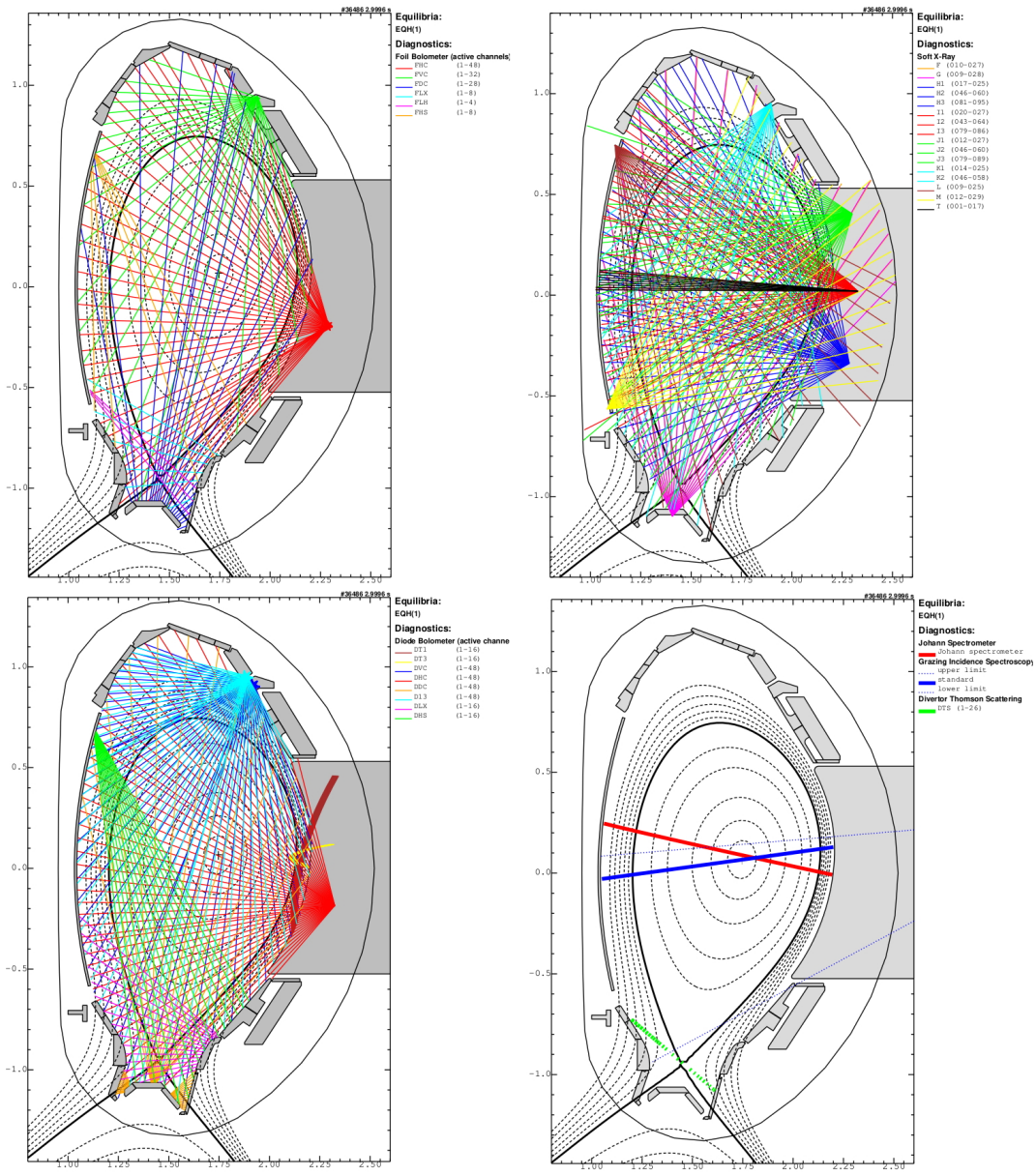

Figure 1.3: Illustrated LOS of the (a) foil bolometers BLB, (b) the soft X-ray cameras SXR, (c) AXUV diode bolometers XVR, and (d) Johann and Grazing Incidence spectroscopes, JOH and GIW respectively. Figures were plotted in Diaggeom tool.

1.5.4 Étendue

As described in previous sections, the plasma volume emits radiation in a broad region of the spectrum at some power, which we call emissivity $[\Sigma] = \mathrm{W} \cdot \mathrm{m}^{-3}$. Radiation from a plasma is typically measured as incident radiation of some frequency ν given by the type of source, the optical elements, and the sensitivity of the detector of an area A from a solid angle Ω. The solid angle is then determined by collimating optics, for example, the pinhole area S_A and its distance from the detector d.

The resulting signal and power at the detector are given by the incident radiance $[J(\nu)] = \mathrm{W} \cdot \mathrm{m}^{-2} \cdot \mathrm{sr}^{-1}$, which is the radiant flux $[\Phi] = \mathrm{W}$ received from the solid angle to the detector area. Thus, $\Phi = J(\nu)A\Omega$, where the product $[A\Omega] = \mathrm{m}^2 \cdot \mathrm{sr}^{-1}$ sometimes also denoted E is called the geometrical étendue or also the geometrical

factor [12]. This étendue gives the ability of the system to gather light from its surroundings and can be defined in a simple approximation as:

$$E = A \cdot \Omega = S_D \cdot |\cos(\alpha)| \frac{S_A \cdot |\cos(\gamma)|}{4\pi d^2} \tag{1.46}$$

where S_D is the detector area at an angle α with respect to the line of sight and S_A is the aperture area at a distance d at an inclination γ. Dimensions of the detector and aperture can also be taken into account. For the rectangular shape of the SXR camera components, an extension is used:

$$E = \frac{P_x P_y D_x D_y \cos^4\alpha}{4\pi d^2} \left[1 - \frac{1}{6}\frac{D_y^2 + P_y^2}{d^2}\cos^2\alpha + \frac{D_x^2 + P_x^2}{d^2}\left(\sin^2\alpha - \frac{1}{6}\right)\right]. \tag{1.47}$$

Relating the emissivity to the photon energy interval, we call it the spectral emissivity $[\varepsilon] = \mathrm{W} \cdot \mathrm{m}^{-3}\mathrm{eV}^{-1}$. The power P detected by the detector looking at the solid angle Ω along the LOS denoted by S will be equal to:

$$P = \int_S \mathrm{d}r \int \mathrm{d}E \, \frac{\Omega(r)}{4\pi} \varepsilon(r, E) \cdot \eta(E). \tag{1.48}$$

This expression can be simplified by assuming that the field of view of the detector is sufficiently narrow and the emissivity does not vary much across the LOS:

$$P \approx \frac{A\Omega}{4\pi} \int_S \mathrm{d}s \int \mathrm{d}E \; \varepsilon(s, E) \cdot \eta(E). \tag{1.49}$$

Finding the spatial distribution of the plasma emissivity $g = \Sigma = \int \varepsilon(E)\,\mathrm{d}E$ based on the integral values of f (brightness) in mathematical terms means solving a system of integral equations:

$$f_i = \int_{S_i} \mathrm{d}s \, g(r), \tag{1.50}$$

which is a set of the so-called Fredholm integral equations of the first kind, also known as the tomography problem [25].

1.6 Computer tomography

The aim of tomographic reconstruction is to find the spatial distribution of the scalar field in the plane of interest. This reconstruction is based on the knowledge of integrals along the lines of sight (LOS). However, the use of computer tomography in devices with magnetic confinement faces several obstacles.

An insufficient number of views into the tokamak chamber and their uneven distribution result in a lack of lines of sight and overall directions of view. The number of LOS is usually limited to the order of 100, and cameras are often positioned in such a way that views are limited to horizontal and vertical perspectives. Fortunately, this is not the case with the ASDEX Upgrade tokamak, where, for example, SXR cameras are compact enough to fit into the existing gaps between the tiles. This allows them to be placed on the high-field side and in the area under the divertor. Some camera systems can be compact enough and at the same time combine several measurement techniques. For example, RADCAM [23]

combines foil bolometers, AXUV diodes, and soft X-ray diodes while maintaining a small size.

The cost of individual cameras also plays a role. A uniform design of camera heads reduces their acquisition costs, allowing a higher number of chords. Some chips used in cameras may show signs of degradation after only a few weeks. They need to be replaced every 1-2 years, again putting pressure on the low price of the camera chip [24]. Noise in the detectors is also a significant problem for subsequent evaluation and tomographic reconstruction. Its level is very difficult to determine and changes over time with gradual degradation of the detector [26].

The tomography problem is always underdetermined since an infinite number of integral values would be needed to find an exact solution. A solution may be to reduce the number of degrees of freedom by, for example, dividing the poloidal cross section into pixels. Furthermore, inversion of these equations is an ill-posed problem because of finite sampling. The differential operator in the inversion causes an amplification of the noise of the data and therefore the solution is not unique [27]. By linear regularisation of the problem, we insert additional information or assumptions about the solution. Specifically, it is a requirement for the smoothness of the solution by minimising the gradient [25].

1.6.1 Tomographical inversion code

Tomotok [28], a Python package, was created at the Institute of Plasma Physics of the CAS and is openly accessible under the EUPL. It is organised into distinct and autonomous repositories. The primary one is the Core package, which contains algorithms for tomographic inversion used for diagnostics of radiation from plasmas on tokamaks. It incorporates a variety of inversion techniques, including Minimum Fisher regularisation for sparse matrices utilising Tikhonov regularisation. It also includes the Biorthogonal Basis Decomposition (BOB) for dense matrices, the Generalised Eigenvalues (GEV), and the SVD method. Beyond the inversion algorithms, it offers additional support features. For instance, it includes functions for creating phantoms, i.e. synthetic radiation profiles. These can be either isotropic or anisotropic, meaning that they can align with the magnetic flux surfaces. Another notable feature is the computation of the geometry matrix using a single-line-of-sight approximation. The Core package is complemented by packages specifically designed for individual tokamaks. These packages offer tools for retrieving data from diagnostic systems and obtaining device geometry.

An alternative to the Tomotok package is the more advanced pyTomo [29] code, which is mainly developed for DIII-D and AUG tokamaks and is specialised for line integrated diagnostics. Its strengths are a functional GUI and a number of implemented features. As in the case of Tomotok, it implements Tikhonov regularisation with Minimum Fisher Information regularisation. In addition to direct regularisation, it also includes improved sparse singular value decomposition (sSVD) and sparse QR decomposition (sQR). These take advantage of the fact that geometric matrices usually have less than 5 % non-zero elements and regularisation matrices even less. Therefore, it is possible to use the sparse Cholesky decomposition. In addition, the generalised eigenvalues (GEV) and the generalised SVD (GSVD) methods are implemented. Several methods are used to find the regularisation parameter as well, for instance, the Morozov discrepancy principle, the predicted residual error sum of squares, and the corrected Akaike information criterion.

1.6.2 MFR algorithm

The algorithm selected for tomographic inversion in this thesis is minimum Fisher regularisation, which uses Tikhonov regularisation with minimisation of Fisher information and is well described in Refs. [27] and [25]. It uses square pixels, called nodes, as basis functions, which must be small enough to consider uniform emissivity in each of them. The problem can be expressed by the following equation:

$$f_i = \sum_j^N T_{ij} g_j + \xi_i, \tag{1.51}$$

where f_i are the integral values along the chord i (LOS), that is, the signal measured by the detector i and g_j are the emissivity elements sought in a node j of the poloidal cross section. The geometry matrix $\mathbb{T}$ describes the spatial distribution of the lines of sight and the element T_{ij} has the meaning of the length of the chord i passing through node j. In addition, one has to consider the systematic error and the noise ξ_i of the signal i. If the values $\vec{f}$ are defined as the brightness $[f_i] = \mathrm{W} \cdot \mathrm{m}^{-2}$ given by:

$$f_i = \frac{4\pi P_i}{(A\Omega)_i}, \tag{1.52}$$

then $\vec{g}$ will be the emissivity in units $[g_j] = \mathrm{W} \cdot \mathrm{m}^{-3}$ and the elements of the geometric matrix $\mathbb{T}$ in units $[T_{ij}] = \mathrm{m}$. But if the values of $\vec{f}$ are the power $[f_i] = \mathrm{W}$, then the components of the geometry matrix $\mathbb{T}$ will be in units $[T_{ij}] = \mathrm{m}^3 \cdot \mathrm{sr}$ and $[g_j] = \mathrm{W} \cdot \mathrm{m}^{-3} \cdot \mathrm{sr}^{-1}$.

The second case can occur for the ray-tracing technique. An example from the ASDEX Upgrade on the foil bolometer cameras is in Ref. [30]. Ray-tracing technique inversion (also sensitivity or geometric) matrices are generated by a path-tracing algorithm that uses a Monte Carlo approach to send an ensemble of rays from the detector, thus replacing the single optical path of the detector. A 3D model is used for this purpose, so optical effects such as occlusion and vignetting, or in advanced algorithms reflections, are included. Such a geometric matrix can be built using the CHERAB code with the Raysect ray-tracing package.

The advantage of the ray-tracing technique is that it dominates when the solid angle of the detectors is large and covers steep and spatially diverse gradients. When the detector field of view is strongly collimated, the ray-tracing and analytic formulas for étendue agree, and the advantages of the ray-tracing technique are not as significant. For the sake of simplicity, only the single-ray model was used in this work.

A straightforward inversion of the matrix $\mathbb{T}$ is almost impossible because the problem is underdetermined and poorly conditioned. After finding the reconstruction matrix $\mathbb{M}$, for example, by minimising χ^2, it is feasible to obtain the unknown g_j:

$$g_j = \sum_i^P M_{ji} f_i. \tag{1.53}$$

However, since the number of solutions is infinite, it is possible to achieve $\chi^2 = 0$, the so-called overfitting. The matrix $\mathbb{T}$ has many small eigenvalues, and so regularisation of the problem is necessary [27]. To obtain a realistic result, instead of minimising χ^2, the functional $\phi = \frac{1}{2}\chi^2 + \alpha R$ must be minimised. The positive

parameter α is the weight between the two constraints and R is another functional that represents a requirement such as smoothness. After regularisation, the problem looks as follows:

$$\sum_{j}^{N}\left(\sum_{l}^{P} T_{kl}^{T} T_{lj} + \alpha H_{kj}\right) g_j = \sum_{i}^{N} T_{ki}^{T} f_i, \tag{1.54}$$

where this form is convenient from the point of view of calculating only one inversion and where the matrix $\mathbb{H}$ is a regularisation matrix that can take different forms. Minimum Fisher regularisation differs from linear regularization in the regularization matrix containing the weights $\vec{w}$. For the isotropic case, the regularisation matrix $\mathbb{H}$ looks as follows:

$$H_{kj} = \sum_{m}^{N} B_{x,km}^{T} w_m B_{x,mj} + \sum_{m}^{N} B_{y,km}^{T} w_m B_{y,mj} \tag{1.55}$$

Here, matrices $\mathbb{B}_x$ and $\mathbb{B}_y$ are called smoothing matrices and represent finite-difference matrices along the Cartesian coordinate system [25]. Another possibility is to assume a smooth emissivity profile along magnetic flux surfaces. The anisotropic regularisation matrix $\mathbb{H}$ then looks as follows:

$$H_{kj} = S(\eta) \sum_{m}^{N} B_{\parallel,km}^{T} w_m B_{\parallel,mj} + S(-\eta) \sum_{m}^{N} B_{\perp,km}^{T} w_m B_{\perp,mj}, \tag{1.56}$$

where the matrix $\mathbb{B}_{\parallel}$ represents the finite-difference smoothing matrix along the magnetic flux surfaces and the matrix $\mathbb{B}_{\perp}$ across [26]. The function $S(\eta) \in (0, 1)$ gives weight to the perpendicular and parallel components and is chosen as the sigmoid function:

$$S(\eta) = \frac{1}{1 + e^{-\eta}} \tag{1.57}$$

The mathematical meaning of anisotropic regularisation is that the diffusion is higher along the magnetic field. The ratio between parallel and perpendicular diffusion can be adjusted not only for the entire cross section, but it can be tuned for individual pixels or entire regions separately, as described in Ref. [31]. For example, in the X-point region, a higher diffusion across the magnetic field can be chosen compared to the core plasma. However, compared to the implementation in Tomotok, such an algorithm may have up to 24 parameters for the regularisation.

To minimise the Fisher information of the reconstructed emissivity profile, it is necessary to find the $\vec{w}$ weights iteratively. In the first step, the problem of Eq. 1.54 is solved with the weights $w_m = 0$. The solution of these equations $\vec{g}$ is used to compute the new weights $\vec{w}$ as follows:

$$w_i = \begin{cases} \frac{1}{g_i}, & \text{if } g_i > 0 \\ \max(\vec{w}), & \text{if } g_i \leq 0 \end{cases} \tag{1.58}$$

This is iterated until the difference $\vec{g}$ satisfies the condition. The search is based on the Pearson χ^2 test:

$$\chi^2 = \frac{1}{P} \sum_{i}^{P} \left(\frac{(\vec{f} - \mathbb{T}\vec{g})_i}{\sigma_i} \right)^2 = \frac{1}{P} \sum_{i}^{P} \left(\frac{\xi_i}{\sigma_i} \right)^2 \approx 1, \tag{1.59}$$

where σ_i represents the standard deviation of the signal f_i. Therefore, the process of finding the reconstructed profile involves minimising the Fisher information and minimising the functional ϕ. Thus, the optimal α and the weights $\vec{w}$ are found [25].

The residual χ^2 should ideally be $\chi^2 \approx 1$. An overfitted model is said to be $\chi^2 < 1$ and it represents a nonphysical result with a high error that is too dependent on the data. An underfitted model is when $\chi^2 > 1$ and it represents a wrong model that does not adequately describe the measured data.

1.7 Transport

Radial transport perpendicular to the magnetic flux surfaces of impurities n_Z is described by the conservation law of particle density as follows:

$$\frac{\partial n_{I,Z}}{\partial t} = -\nabla \Gamma_{I,Z} + Q_{I,Z}, \tag{1.60}$$

which can also be interpreted as Fick's second law. The quantity $\Gamma_{I,Z}$ is the radial impurity flux density and Q_Z is the sink and source term that originates from ionisation, recombination, and charge exchange. The convention of the sign of the flux is adopted such that the positive flux represents an outward flow of particles. Since this relationship is true for an impurity of a given species and stage of the ion Z, the set of these equations is thus coupled with each other. It may be assumed that, because of the large transport coefficients in the direction parallel to the magnetic field, the density of n_Z is constant along them. This may also be true for the term Q_Z, but not for the term $\Gamma_{I,Z}$. This is because of the dependence of the toroidal magnetic field on $1/R$ and also because the flux surfaces are shorter on the outside than on the inside.

The flux surface averaged continuity equation in cylindrical geometry, where r is the coordinate defined by 1.15 and where $\Gamma_{I,Z}$ is the flux surface averaged density looks as follows:

$$\frac{\partial n_{I,Z}}{\partial t} = -\frac{1}{r}\frac{\partial}{\partial r} r \left(\Gamma_{I,Z}\right) + Q_{I,Z} \tag{1.61}$$

The particle flux density Γ_Z can be written using the ansatz stating that Γ_Z depends on the density and that it is composed of diffusive and convective parts:

$$\Gamma_{I,Z} = -D_{I,Z}\frac{\partial n_{I,Z}}{\partial r} + V_{I,Z} n_{I,Z}, \tag{1.62}$$

where D is the radial diffusion coefficient and V the radial convection velocity. The resulting equation for radial impurity transport, for a given ion stage of a given species or for the sum of the ionisation stages with averaged values weighted over fractional abundances, becomes the following [32]:

$$\frac{\partial n_I}{\partial t} = \frac{1}{r}\frac{\partial}{\partial r} r \left(D_I \frac{\partial n_I}{\partial r} - V_I n_I \right) + Q_s \tag{1.63}$$

1.7.1 Classical transport

Electrically charged particles interact with each other through Coulomb collisions, leading to particle transport. Collisions are characterised by the collision

frequency ν_{col}. In each of such collisions, the particle in the magnetic field is displaced in the radial direction by up to the Larmor radius ρ_L. A series of such collisions in a random direction is represented by a random walk, which results in a classical diffusion characterised by a diffusion coefficient D^{class}:

$$D^{class} \approx \rho_L^2 \nu_{col}. \tag{1.64}$$

The binary collision frequency ν_{ab} between the particles of species a and b can be determined as follows:

$$\nu_{ab} = \frac{4\sqrt{2\pi}e^4}{3(4\pi\varepsilon_0)^2}\sqrt{\frac{m_a m_b}{m_a+m_b}}\frac{Z_a^2 Z_b^2}{T^{3/2}}\frac{n_b}{m_a}\ln\Lambda_{ab}, \tag{1.65}$$

where the temperatures of the two species of particles are assumed to be equal [32]. The Coulomb logarithm $\ln\Lambda$ for thermal ion-ion collisions can be determined from [33]:

$$\ln\Lambda = 23 - \ln\left(n_e^{1/2} T_i^{-3/2}\right), \quad [\,\mathrm{cm}^{-3}; \mathrm{eV}] \tag{1.66}$$

and for mixed ion–ion collisions [34]:

$$\ln\Lambda_{ab} = 23 - \ln\left[\frac{Z_a Z_b(\mu_a+\mu_b)}{\mu_a T_{i,a} + \mu_b T_{i,b}}\left(\frac{n_{i,a}Z_a^2}{T_{i,a}} + \frac{n_{i,b}Z_b^2}{T_{i,b}}\right)^{1/2}\right] \tag{1.67}$$

1.7.2 Neoclassical transport

The ratio of the effective collision frequency for detrapping ν_{eff} and the bounce frequency ν_b is called the normalised collision frequency ν^*, or collisionality:

$$\nu^* = \frac{\nu_{eff}}{\nu_b} \tag{1.68}$$

and is used to determine in which regime the transport is [6]. In Fig. 1.4, the different transport regimes described in the following are plotted versus collisionality and normalised radius. Furthermore, using the collision frequency ν_{DW} and ν_{DD}, the main ion collisionality can be defined as follows [32]:

$$\nu_D^* = \frac{\nu_{DD}+\nu_{DW}}{v_{th}\varepsilon^{3/2}} q\pi R_0 \tag{1.69}$$

and the tungsten impurity collisionality as follows:

$$\nu_W^* = \frac{\nu_{WD}}{v_{th}\varepsilon^{3/2}} q\pi R_0. \tag{1.70}$$

For low collision rates, trapped particles can complete multiple bounce orbits before colliding again. This is called a banana regime or a weakly collisional regime. It occurs when the effective collision frequency for detrapping ν_{eff} from Eq. 1.13 is less than the bounce frequency ν_b of Eq. 1.10:

$$\nu_{eff} \ll \nu_b \iff \nu^* < 1. \tag{1.71}$$

Transport in such a regime is given by banana orbits. However, there are only f_t trapped particles. With each collision, their orbit changes slightly. After being detrapped, they are in an orbit of a different radius than initially shifted by the

banana orbit width Δ_b from Eq. 1.10. The diffusion coefficient can be determined from the random walk using the orbit width, bounce frequency, and fraction of trapped particles:

$$D^B \approx \frac{q^2 \rho_L^2}{\varepsilon^{3/2}} \nu_{col}. \tag{1.72}$$

The diffusion coefficient D^B is larger than the classical diffusion coefficient D^{class} by a factor $q^2 \varepsilon^{-3/2}$. The opposite is the strongly collisional regime, where collisions occur so frequently that no banana orbit is completed, and the effect of trapped particles is negligible. This is the so-called Pfirsch-Schlüter regime and occurs when the collisionality condition is satisfied:

$$\nu^* \gg \varepsilon^{-3/2}. \tag{1.73}$$

The radial shift caused by vertical drift plays an major role here. The particle is shifted with respect to the magnetic surface by a distance d for half of a revolution in the poloidal direction. Since collisions are very frequent, it is necessary to consider that the particle does not complete the entire revolution of the orbit. The resulting diffusion coefficient for the Pfirsch-Schlüter regime then looks as follows:

$$D^{PS} \approx \pi^2 q^2 \rho_L^2 \nu_{col}, \tag{1.74}$$

where it differs by a factor of $\pi^2 q^2$ compared to D^{class}. Between the two extremes lies the intermediate (plateau) regime. In this region, diffusion is mainly driven by particles with slow circulation. The plateau diffusion coefficient D^P is independent of the collision frequency [6]:

$$D^P \approx \frac{q \rho_L^2}{R} v_{th} \tag{1.75}$$

In the framework of the neoclassical theory, the ratio of diffusion coefficients for the Pfirsch-Schlüter regime can be determined as follows:

$$\frac{V_{I,Z}^{PS}}{D_{I,Z}^{PS}} = Z \left[\frac{\mathrm{d} \ln n_D}{\mathrm{d}r} + \frac{H^{PS}}{K^{PS}} \frac{\mathrm{d} \ln T}{\mathrm{d}r} \right] \tag{1.76}$$

where the ratios K^{PS} and H^{PS} in the drift term are functions:

$$H^{PS} = -\frac{1}{2} + \frac{0.29 + 0.68 \cdot \alpha}{0.59 + \alpha + 1.34 \cdot (\varepsilon^{3/2} \nu_D^*)^{-2}} \approx -\frac{1}{2}. \tag{1.77}$$

$$K^{PS} = 1 - \frac{0.52 \cdot \alpha}{0.59 + \alpha + 1.34 \cdot (\varepsilon^{3/2} \nu_D^*)^{-2}} \approx 1. \tag{1.78}$$

and are functions of the impurity strength parameter α [32, 35]:

$$\alpha = \frac{n_W Z_W^2}{n_D}. \tag{1.79}$$

The radial impurity flux exhibits both diffusive and convective characteristics, regardless of the type of regime the plasma is in. As can be seen from Eq. 1.76, the radial drift velocity depends on the normalised gradients, which after inversion is also called the length of the gradient. After substituting Eq. 1.76 to Eq. 1.7.3 it follows that for the peaked profile, the gradients are negative and the convective

term is also negative. Thus, there is impurity convection towards the plasma centre and a so-called impurity accumulation. However, if the drift term ratio is negative: $\frac{H^{PS}}{K^{PS}} \approx -1/2$, the direction of this convection can be reversed and a temperature screening can occur. Such a temperature screening was measured in Ref. [36] or modelled in Ref. [35] with analytical model and with the drift kinetic code NEO.

One way to reduce high-Z impurities from the plasma involves central wave heating, either through electron cyclotron heating (ECH) or ion cyclotron resonance heating (ICRH). Using ECH can reduce the neoclassical inward pinch for impurities by flattening the main ion gradients [37].

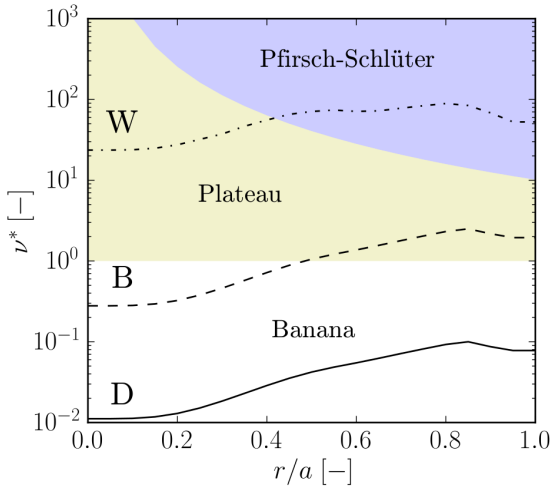

Figure 1.4: The collisionality evaluated for tungsten (W), boron (B) and deuterium (D) in AUG discharge #30812 at time 4.6 s. Reprinted from [38].

Experimentally, the transport coefficients D and V can be estimated by linear regression of the measured flux of impurities particles Γ of a given species. The exact procedure is described in Chapter 3.

In addition to neoclassical theory, turbulence-driven radial transport also plays a role. The total measured impurity flux is the sum of the neoclassical flux and this turbulence-driven flux: $\Gamma_Z = \Gamma_Z^{neoc} + \Gamma_Z^{turb}$. This is possible assuming that momentum exchange among different species should remain unaffected by the transport induced by fluctuations. For the radial impurity flux, then the following will be true:

$$\Gamma_Z = -(D_Z^{neoc} + D_Z^{turb})\nabla n_Z + (V_Z^{neoc} + V_Z^{turb})n_Z \tag{1.80}$$

Although there is no experimental method to distinguish the contribution of collision-driven and turbulence-driven transports, it can be assumed that the deviation from neoclassical theory is due to turbulence-driven transport [36].

1.7.3 Experimental methods

The tungsten transport can be experimentally studied using different methods. The first one is the sublimation probe, which is a tungsten pin placed at the strike point. In Ref. [39] an experiment where divertor retention R is measured using this device is described. In these experiments the strike point is moved towards the pin, causing melting of it and hence massive injection of tungsten impurities. The second type of experiment is the laser blow-off (LBO). Using a high power laser, tungsten is

released through ablation from a thin layer deposited on a glass plate. The duration of this laser pulse is 10 ns and the position of this device on the LFS is shown in Fig. 1.5 [39]. For this type of experiment, a short source function is important for proper evaluation of the transport.

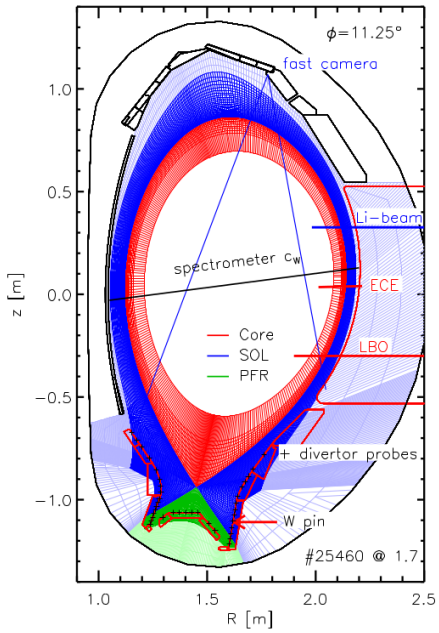

Figure 1.5: The injection of tungsten impurities into the plasma can be achieved by melting a tungsten pin or with the laser blow-off (LBO) device. Reprinted from [39].

Two phases can be distinguished in the impurity injection. First, there is a rapid increase in tungsten concentration caused by high influx, which is mainly due to diffusion. Subsequently, there is a slow exponential decrease in concentration, which is caused by diffusive and convective terms equally. In this thesis, the discharges from the AUG tokamak where the LBO type of experiment was performed are analyzed. Then, only those LBOs where there were not too high changes in density and temperature were selected from the particular discharges [37].

Chapter 2

Methodology

In the following chapter, the calculation of the cooling factor for tungsten is presented in Sect. 2.1. It is calculated for various diagnostics with their own spectral response. The model includes calculation of ionisation balance, line radiation, and bremsstrahlung. In Sect. 2.2 the resulting tomographic reconstructions and the application of the different diagnostics are discussed.

In this chapter and in the following one, the results of the discharges performed on the ASDEX Upgrade tokamak as part of the MST1-Topic 10/WPTE-RT03 in 2019 and 2020 are presented. The analysis in this chapter is mainly demonstrated in the discharge #37614, whose overview is plotted in Fig. 2.1. It is an experiment with a successfully performed laser blow-off of tungsten at time 3.15 s and 4.198 s. In this discharge, radiation P_{tot} and the concentration of tungsten c_W gradually increase until disruption. It can be seen that both LBOs are performed at different ICRH heating settings and that the density and temperature are constant at both times.

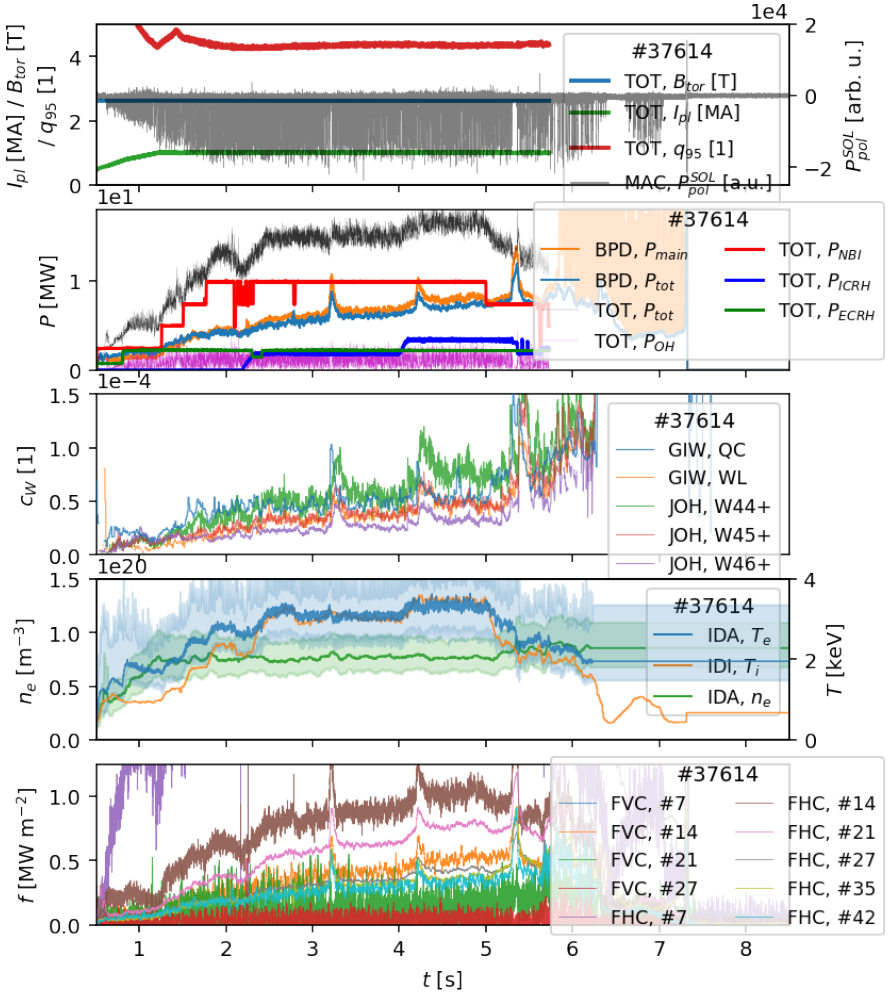

Figure 2.1: Overview of the discharge #37614. (a) toroidal magnetic field B_{tor}, plasma current I_{pl}, safety factor q_{95} and signal from RT diagnostics for halo current measurements P_{pol}^{SOL}. (b) total radiated power P_{tot} from BPB, radiated power P_{main} in main plasma from BPD, ECRH, NBI, ICRH and Ohmic power including total plasma power from TOT. (c) Tungsten concentration from Johann spectrometer JOW from single line diagnostics and the grazing incidence spectrometer GIW from quasicontinuum QC and line emission. (d) Electron temperature T_e and density n_e from IDA integrated data analysis and ion profile T_i from IDI. (e) Selected channels from foil bolometers of vertical camera FVC and horizontal camera FHC which LOS can be seen in Fig. 1.3.

The electron temperature and density profiles for the first LBO are plotted in Fig. 2.2. The time evolution of the variables during LBO development is shown in Fig. 3.17. The selection of time steps for the plotting includes a time 3.15 s at the beginning of the LBO for the intact profile, a maximum at time 3.22 s and then an exponential decrease at time 3.25 s with a time 3.3 s when the steady state should have already re-emerged. The tungsten density profile was obtained from GIW and JOH spectrometry, and the procedure is described in Sect. 3.1. The sections hatched in the plots represent local error bars from the integrated diagnostics and have the meaning of inconsistency between the data from the various diagnostics. They are therefore primarily for an informative purpose.

In addition, discharge #37639 with successful LBO at time 3.149 s was selected for analysis (represented in Fig. 29). Furthermore, two discharges without LBO are

included: #36476 and #36486, presented in Figs. 30 and 31.

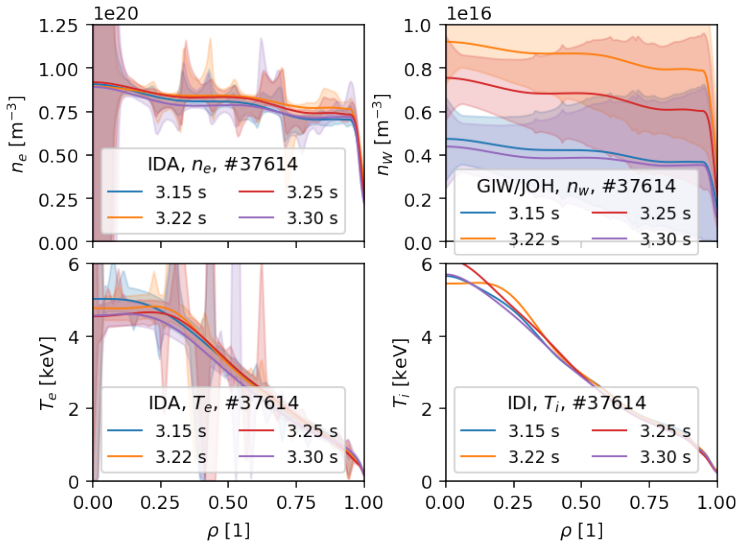

Figure 2.2: Electron density n_e and temperature T_e profiles and tungsten density profiles n_W for selected times in the #37614 discharge. The selected time steps cover the development of the first LBO.

2.1 Cooling factor of tungsten

In the following part of the thesis the input data and results of the model of high-temperature plasma radiation will be described. The radiation source investigated is mainly tungsten. Its radiation only weakly depends on the electron density n_e, thus in the graphs the dependence on the electron temperature T_e is shown mainly, which in many cases is also weak. For AUG tokamak data analysis, the region of interest is from ~ 10 eV to about 5 keV.

The primary source of data is the ADAS (i.e. Atomic Data and Analysis Structure) system from the Ref. [13]. This is a set of codes for modelling the radiating properties of ions and atoms in plasmas. Its applications are very broad, from astrophysics to technological plasmas, and it is also suitable for thermonuclear fusion devices. The output of ADAS is used in many plasma modelling codes, such as STRAHL and Aurora. It includes a large database of fundamental or derived atomic data in Open ADAS. In this work, only these processed data are used. Thus, neither the codes for the calculation of fundamental atomic data nor the subroutine libraries are used.

Another possible source of atomic data is the FLYCHK code from Ref. [40]. Like ADAS, it can generate atomic-level populations and charge-state distributions. It can be used on Maxwellian or non-Maxwellian electron distributions or even on optically thin or thick plasmas. It can therefore be used as an alternative data source for a radiative plasma model or for verification of results. Unfortunately, this was not possible in this work due to time constraints.

For a double check of the resulting cooling factor from Open ADAS, the results from Ref. [18] are used. The cooling factor of tungsten evaluated using state-of-the-art data, which are benchmarked with experimental results, is presented here. These are calculated using the Cowan code and the ADAS system. In this

thesis, these data are considered as reference. A second source for comparison is Ref. [19], where tabulated tungsten cooling factor data are also presented.

2.1.1 Ionisation fraction

The first step to study the plasma emission is to establish the ionisation balance, i.e. to find the fractional abundance as a function of temperature. Based on the procedure described in Sect. 1.3, the fractional abundance is found, which is plotted in Fig. 2.3 for a wide range of temperatures and in Fig. 2.4 for the range of temperatures relevant to the AUG tokamak discharge. It is calculated based on the data provided by the Open ADAS database (Ref. [13]) in ADF11. The effective recombination coefficients α_{CD} and effective ionisation coefficients S_{CD} of data set 50 are used.

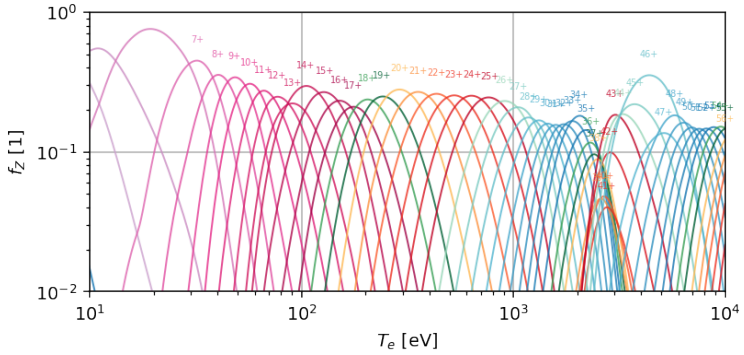

Figure 2.3: Fractional abundance f_Z of tungsten as a function of electron temperature T_e for the temperature range from 10 eV to 10 keV.

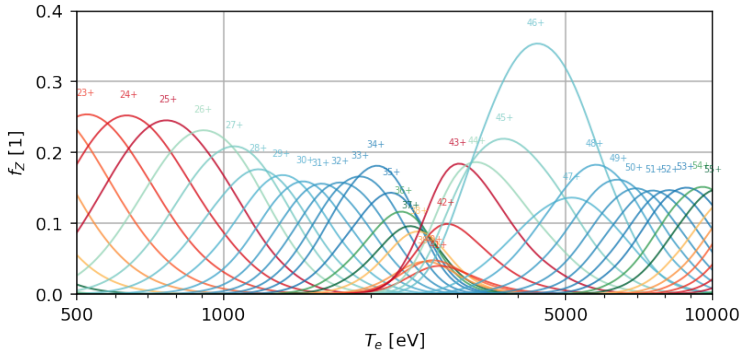

Figure 2.4: Fractional abundance f_Z of tungsten as a function of electron temperature T_e for the temperature range from 500 eV to 10 keV.

After plotting the dependence of f_Z (Fig. 2.5) not on the temperature T_e, but on the normalised radius ρ for discharge #37614 at time $t = 3.15$ s, it is clear that the most abundant ionisation states of tungsten in the centre range from W^{40+} to W^{50+}, specifically in the centre, is Ni-like W^{46+}.

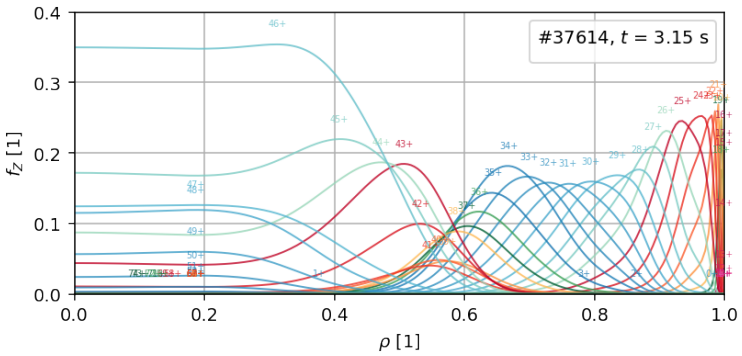

Figure 2.5: Fractional abundance f_Z of tungsten as a function of normalised radius ρ for the discharge #37614 at time $t = 3.15$ s.

The validity of the ionisation balance found is verified according to Ref. [16]. In this reference, adjustments to the recombination rates are done, a comparison is made with the measured spectra, and their modification according to the experiment. The ionisation balances calculated in this thesis from the Open ADAS data are compared with the CADW + modified ADPAK data from Ref. [16] in Fig. 2.6. An reasonably good agreement is found for the ionisation states W^{24+} to W^{46+}, which is sufficient for the purpose of this work.

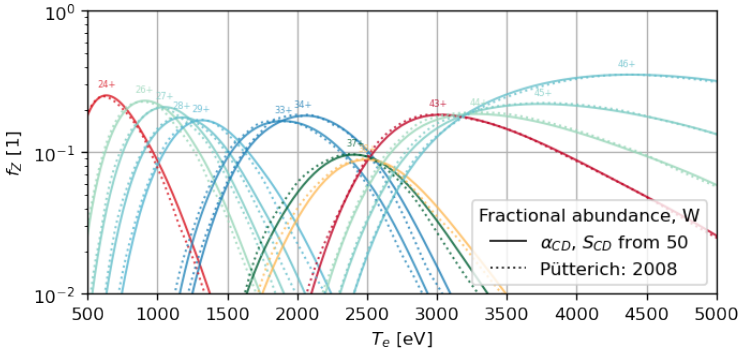

Figure 2.6: Comparison of fractional abundance f_Z of tungsten for selected ionization states calculated from Open ADAS data and from Ref. [16].

Comparison of the W mean charge of the ionisation equilibrium $\bar{Z}$ with the values published in Ref. [18] is also done. In the investigated temperature range, there is good agreement as shown in Fig. 2.7. This suggests that the fractional abundances calculated f_Z from the Open ADAS data are well-determined.

$$\bar{Z}(T_e) = \sum_Z Z \cdot f_Z(T_e) \tag{2.1}$$

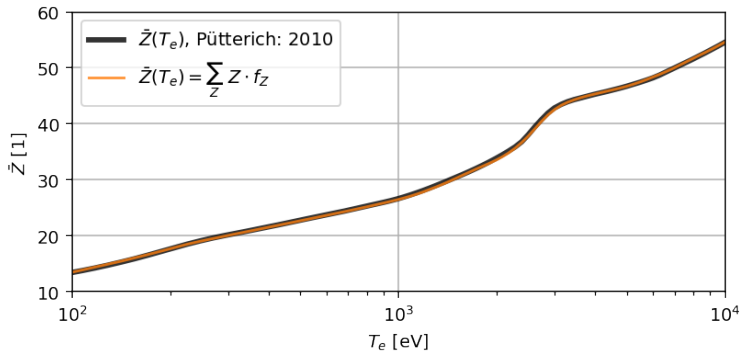

Figure 2.7: Comparison of the mean charge of the ionization equilibrium of tungsten $\bar{Z}$ calculated from Open ADAS data and from Ref. [18].

2.1.2 Photon emissivity coefficients

The calculations can be performed using the configuration average (CA) approximation or as a level-resolved (LR). For the same input electron configurations, it follows that the total radiated power of CA agrees well with the LR calculations. The advantage of configuration average over level resolved is that the computational size and requirements are much smaller. Although LR calculations must keep the number of input configurations low for a smaller computational complexity, a much larger number of configurations can be chosen within CA. This higher number of configurations makes a big difference in the resulting total radiated power by up to a factor of 2. The difference is especially notable for partially filled $4f$, $4d$, or $3d$-shells. The recommendation for calculating the cooling factor is to select a higher number of configurations using the CA model. In contrast, level-resolved data are more suitable for modelling spectra and for the interpretation of broadband soft x-ray emission [1].

The PEC40 data used were calculated with different resolution and complexity. The highest resolution, especially for heavy ions, is provided by intermediate coupling (*ic*-resolution). These include fine-structure level populations and are assumed to describe the true radiated power for all configurations included. The LR calculations bundle levels together in a logical way, and thus allow one to determine the missing power due to missing configurations. Within such an approximation, atomic levels are irrelevant [41, 14].

For light ions or for high collisionality, a term population resolution (*ls*-resolution) is suitable. Also, configuration-average populations (*ca*-resolution) and large configuration-average populations (*cl*-resolution) are available. The population calculations are truncated, and the infinite number of levels is reduced to a finite number for computational feasibility. Levels are thus grouped into bundles, with the necessity to somehow take into account the influence of all higher shells up to infinity. Thus, in the point of view of computational complexity, *ca* or *cl* may include a larger set of excited atom shells than *ic* or *ls*, but at the same time their resolution decreases [41]. For most ionisation states, the difference between *ic* and *ca* is very small, and moreover, it decreases as the number of configurations increases. However, for some configurations, the difference is much greater, such as those with open $4f$ or d shells [14]. For W^{56+} and above, the radiated power from LR and CA is already the same as the number of included configurations is the same.

Although *ca* cannot be used for spectroscopy, the difference in radiated power between two configuration average calculations such as *ca* and large *cl* can be used to calculate the difference due to missing configurations. This difference can then be added to the *ic* calculation to obtain a better estimate [14].

After personal communication with PD Dr. Thomas Pütterich, a more recent and much more extensive PEC50 data set was obtained that is not included in Open ADAS. It was created by first performing level-resolved calculations to obtain the electronic structure. Afterwards, calculations were done to model the electron density-dependent emissions. The resulting cooling factor was benchmarked here using measured experimental data.

Although the typical number of lines for a single state of the PEC40 data set is $n_{line} = 50$, for PEC50 it is much higher, as represented in Fig. 2.8. While uncompressed PEC40 data occupies approximately 6 MB of memory, PEC50 data take up approximately 3.5 GB. Due to its high extent, the PEC50 can be used to model tungsten spectra as shown in Fig. 2.14.

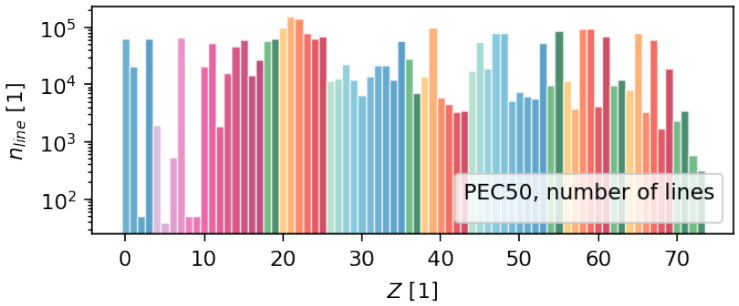

Figure 2.8: Number n_{line} of photon emissivity coefficients PEC for each ionization Z state in PEC50.

The comparison between the PEC50 and *cl*-resolved PEC40 data is shown in the plot of Fig. 2.9. For the electron temperature $T_e = 4$ keV and the ionisation state W^{+46}, the photon emissivity coefficients PEC ($[\mathrm{PEC}] = \mathrm{m^3 s^{-1}}$) are plotted there. It can be seen here that the PEC50 data have a higher resolution compared to PEC40. In Figs. 2.10 and 2.11, the difference between the *cl*-resolved PEC40 and the PEC50 is visualised by using the cooling factor, where the ionisation balance is already taken into account:

$$L_Z = \sum_{line} f_Z(T_e) \cdot \mathrm{PEC}^Z_{line}(n_e, T_e) \cdot E_{line}, \tag{2.2}$$

where E_{line} is the energy of the given spectral line in units of $[E_{line}] = \mathrm{J}$. For the ionisation states W^{+36} to W^{+46} the difference between the PEC50 and PEC40 data is minor, and for states below it is more significant.

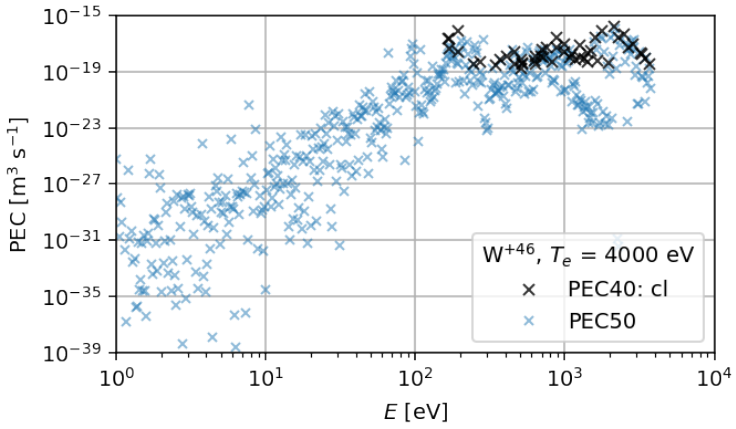

Figure 2.9: Comparison of the values and number of photon emissivity coefficients PEC for the PEC50 and PEC40 datasets in the *cl*-resolution. The data are plotted for temperature $T_e = 4$ keV and ionization state of tungsten W^{+46} only.

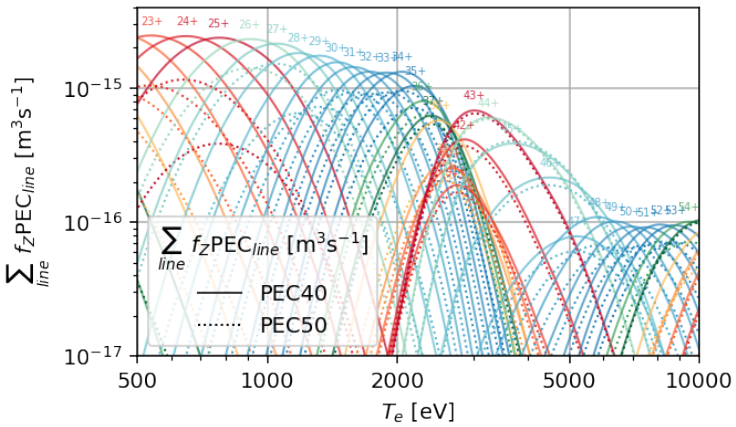

Figure 2.10: The sum of ionization abundances f_Z multiplied by photon emissivity coefficients PEC for each ionization state based on *cl*-resolved PEC40 and PEC50 data.

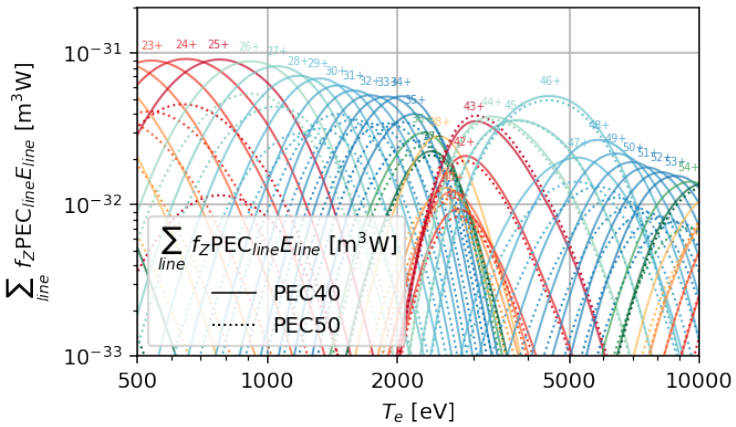

Figure 2.11: Sum of ionization abundances f_Z multiplied by photon emissivity coefficients PEC and transition energy E_{line} for each ionization state based on *cl*-resolved PEC40 and PEC50 data.

The resulting spectral emissivities of the PEC50 and *cl*-resolved PEC40 data are plotted in Fig. 2.12 and Fig. 2.13. Here, tungsten spectral emissivity ε_W^{bb} as a function of electron temperature T_e and with respect to emission energy. This shows that the typical energy of line emission increases with the rising temperature. Higher temperature corresponds to an advancing towards the centre of the plasma. The emission of high-energy radiation is reasonable here because the mean impurity charge increases with rising electron temperature, i.e., the impurities are highly ionised. The electrons in these higher ionisation stages are strongly bound, and the transitions between levels are more energetic.

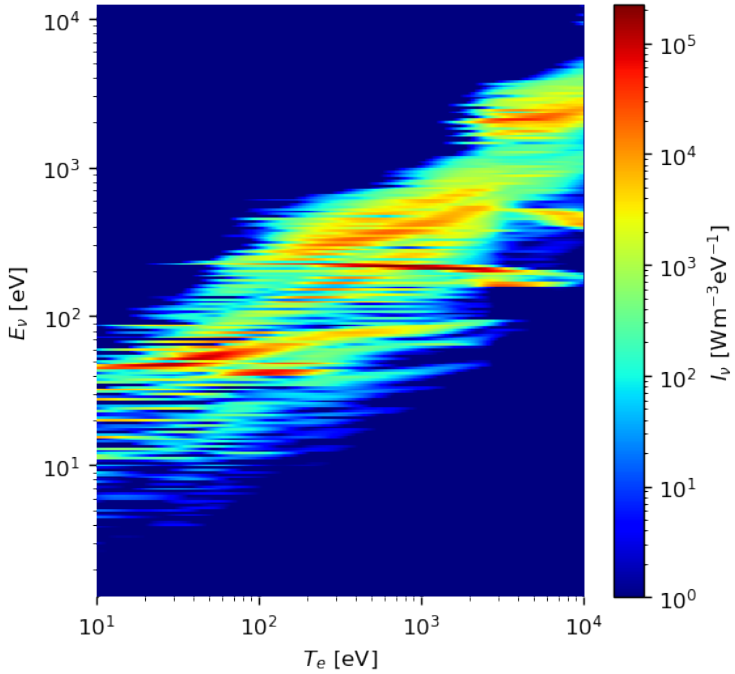

Figure 2.12: Spectral emissivity as a function of electron temperature T_e and emission energy E_ν based on *cl*-resolved PEC40 data.

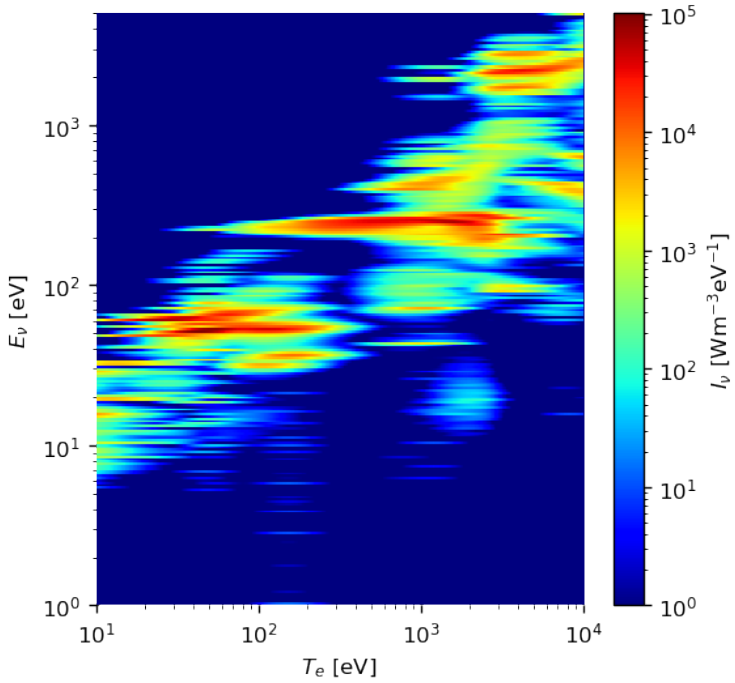

Figure 2.13: Spectral emissivity as a function of electron temperature T_e and emission energy E_ν based on PEC50 data.

The fact that the PEC50 data are much more suitable for the modelling of the spectra is supported by Fig. 2.14. Here, the modelled spectrum region using PEC40 and PEC50 is plotted. In this range around 5 nm, there is a quasicontinuum formed by hundreds of spectral lines from W^{21+} to W^{38+} [16]. The graph reveals that PEC40 describes the quasicontinuum in a different region.

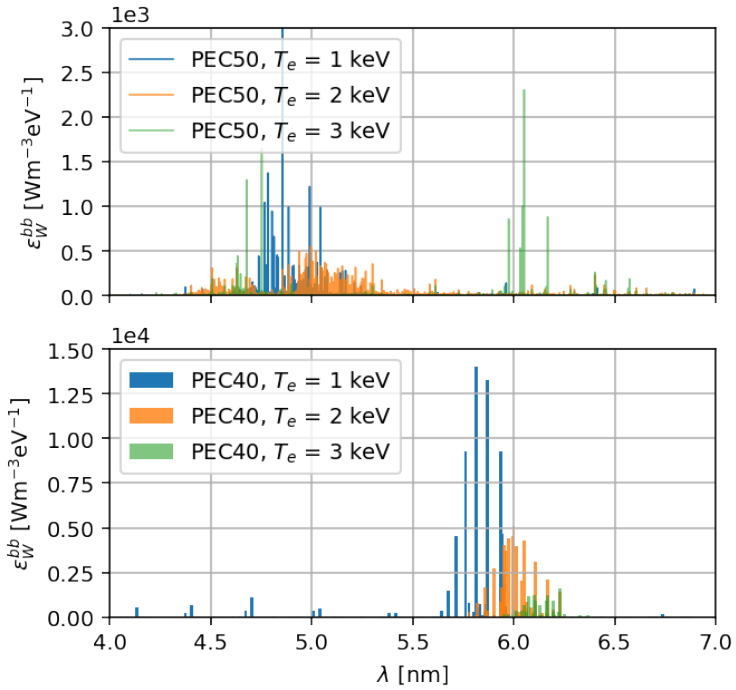

Figure 2.14: Comparison of line spectral emissivities calculated from PEC40 and PEC50 data for three different electron temperatures. The region of quasicontinuum around 50 Å and significant spectral lines of states up to W^{45+} are visualized.

For the following data analysis, it is necessary to decide which data set of photo emissivity coefficients will be primarily used for the calculation of the cooling factor. The PEC40 data were chosen for radiative modelling. The arguments will refer to the results of the following sections.

The first argument is that the cooling factor from the PEC40 data most accurately describes the one published in Ref. [18]. This article is selected for comparison and is considered as the main reference.

The second argument is the shape of the cooling factor graph. As can be seen in Fig. 2.17, for high temperatures above 3 keV the cooling factors are almost identical and their choice has no significant effect. For lower temperatures, the PEC40 data approximately match the cooling factor from Ref. [18] and also Ref. [19]. Both of these references, including the PLT50 data set (which is not calculated from PEC50), suggest that the cooling factor should have a moderate peak around 1 keV. This is not seen in the PEC50 data set, which favours PEC40.

The third argument is that the measured tungsten concentrations in Section 3.1 are overestimated in the pedestal region compared to the measurements from the grazing incidence spectrometer. From Eq. 1.43 it is clear that the calculated concentration is lower for a larger cooling factor. Thus, it seems that the cooling factor in the pedestal region is actually higher. Thus, the PEC40 option is preferred.

In summary, the publicly available PEC40 data from Open ADAS are adopted. It can also be mentioned that they are easier to work with in terms of computer memory compared to the non-public PEC50. Also, it should be taken into account that the PEC40 data was prioritised in terms of total radiated power. If the ability to model the spectra were considered, the PEC50 dataset would have been preferred.

2.1.3 Bremsstrahlung

The braking radiation is modelled on the basis of the relation Eq. 3.2 for bulk plasma and for tungsten impurity. The spectral emissivity for the hydrogen ε_H^{ff} and tungsten ε_W^{ff} plasma is plotted in Fig. 2.15 for different electron temperatures T_e selected. The bremsstrahlung for an impurity with different ionisation states can either be calculated using the effective charge Z_{eff} from Eq. 1.36 or for individual ionisation states. The resulting spectral emissivity is then the sum of the individual emissivities with respect to the ionisation balance of the impurity of interest, in this case tungsten:

$$\varepsilon_W^{ff} = \sum_Z f_Z \cdot \varepsilon_{W,Z}^{ff}. \tag{2.3}$$

As can be seen in Fig. 2.15, as the energy emitted increases, the emissivity decreases very rapidly. As the electron temperature T_e increases, the spectral emissivity for both hydrogen and tungsten increases dramatically. The difference between the emission of tungsten and hydrogen is approximately three orders of magnitude. However, it should be noted that the concentration of tungsten in the selected discharges is approximately $c_W \approx 0.5 \cdot 10^{-4}$. This results in the bulk plasma emission exceeding the tungsten braking radiation emission.

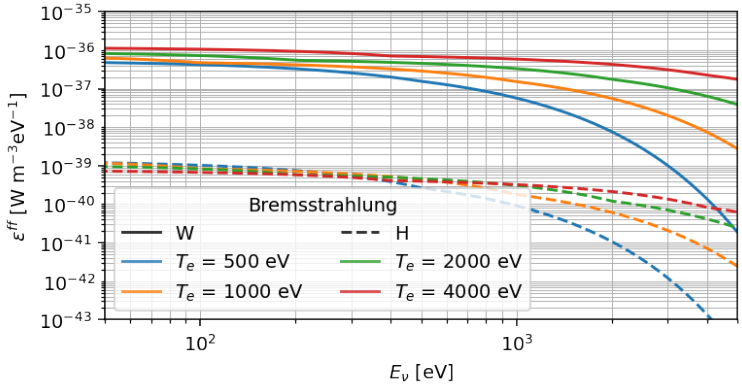

Figure 2.15: Spectral emissivity values ε^{ff} from tungsten and hydrogen braking radiation for selected electron temperatures T_e calculated based on the analytical formula.

2.1.4 Cooling factor

The total radiated power density of tungsten Σ_W by line emission is calculated using its cooling factor L_W:

$$\Sigma_W = n_e n_W L_W(n_e, T_e) = c_W n_e^2 L_W(n_e, T_e), \tag{2.4}$$

where c_W is the concentration of tungsten. Although the cooling factor depends on the electron density n_e, this dependence is so weak that it can be neglected in this work and observation can be directed exclusively to the dependence of the electron temperature. The cooling factor curves are obtained from Ref. [19] and Ref. [18] and are plotted in Figs. 2.16 and 2.17. The power coefficients of the collisional radiative excitation line PLT from PLT40 and PLT50 are also plotted, which are provided in ADAS. These describe the total emission of the individual ionisation states of tungsten and give the cooling factor after considering the ionization balance. In

particular, from Fig. 2.17 it is clear that by choosing the dataset, different values of the cooling factor can be derived, up to a factor of two.

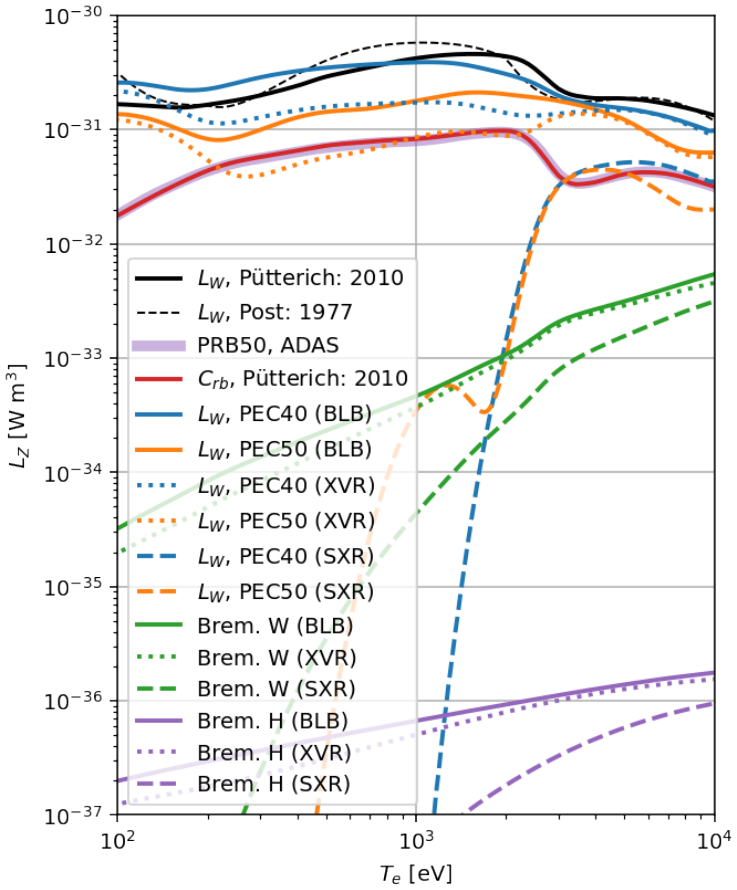

Figure 2.16: Cooling factor obtained from Ref. [18] and Ref. [19], calculated from Open ADAS PEC50 and *cl*-resolved PEC40 data and for H and W bremsstrahlung. The calculated cooling factors are filtered by the spectral response of the detector, i.e. for BLB, AXUV (XVR) and SXR.

For this work, data from Ref. [18] are chosen as the primary reference source. Of course, this can only be used until the moment when data from bolometric cameras are evaluated, which have a broad-spectral and nearly constant spectral response function. However, if data from other cameras, such as diode AXUV or SXR cameras, are used, it is necessary to consider their spectral response according to Eq. 1.40. These are shown in Fig. 1.2.

The original objective of this thesis was to reconstruct a cooling factor based on Open ADAS data as in Ref. [18]. Subsequently, to create a tool that allows us to use the known or predicted spectral response to construct a cooling factor for a given diagnostic. Although the data from Ref. [18] were also generated from the ADAS project, the data used have not been published. The PEC50 data were used, which are discussed in Section 2.1.

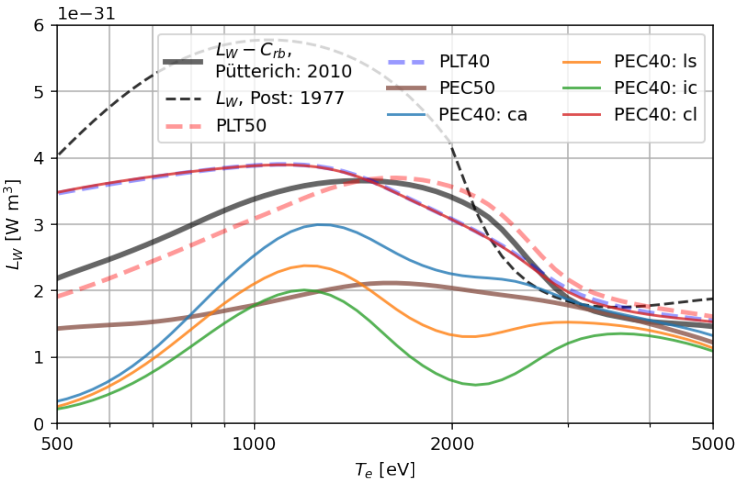

Figure 2.17: Cooling factor for line emission obtained from Ref. [18], Ref. [19] and calculated from Open ADAS PEC50 and PEC40.

In Fig. 2.17, the difference between the cooling factor obtained from PEC50 and the one from Ref.[18] is visible. The *cl*-resolved PEC40 data were used for the subsequent analysis and evaluation of the tungsten concentration of the experimental data. The PLT40 data were based on these data. A characteristic of the analysed tungsten cooling factors is that in the range of interest for the AUG tokamak, that is, the temperature range from 500 eV to 5 keV, the magnitude does not change by more than a factor of two. It can be said that the cooling factor has a weak dependence on temperature. This can be clearly seen in Fig. 2.16 and Fig. 2.17.

The electron density profile and tungsten concentration also play a role in the total radiated power from the plasma. These can be peaked or hollow. In Fig. 2.18 an example was taken for discharge #37614 and time $t = 3.15$ s. It is demonstrated that in the plasma centre the models are almost in agreement, while the main differences are seen at the edge.

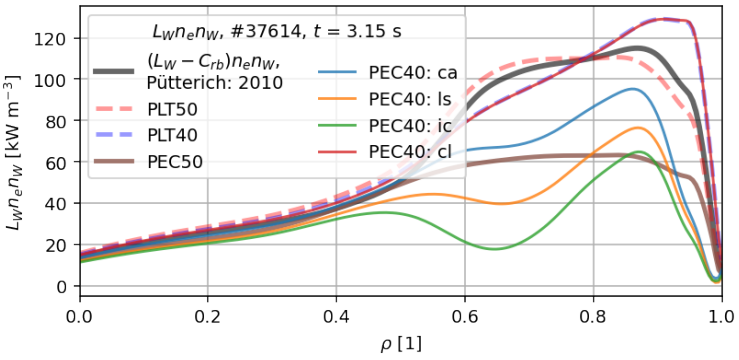

Figure 2.18: Cooling factor for line emission obtained from Ref. [18] and calculated from Open ADAS PEC50 and PEC40 data for discharge #37614 and $t = 3.15$ s.

The cooling factors in Fig. 2.16 filtered by the spectral response η according to Eq. 1.40 are also plotted. This is done for foil bolometers (BLB), for AXUV diodes (XVR) and for soft X-ray (SXR) cameras. The cooling factors are very similar for foil and diode bolometers, with the difference being higher for low temperatures. As mentioned in the Sect. 1.5, AXUV diodes are subject to severe degradation.

Although this degradation in the VUV region has been observed, for example, in Ref. [20] or in this thesis, it has not been quantified. Since it is not included in the spectral response function, a source of measurement processing error can be expected here.

The difference in cooling factor filtered by the spectral response of SXR cameras compared to bolometers is much higher. The discrepancy is especially significant for the line radiation as shown in Fig. 2.16. For electron temperatures below 2.5 keV, the filtered cooling factor is so low that SXR cameras are almost insensitive in this region. There is a very sharp edge in this region, causing a drop of up to two orders of magnitude. This practically corresponds to a normalised radius of approximately $\rho \approx 0.7$. For bremsstrahlung originating from both tungsten and hydrogen plasmas, the difference between SXR and bolometers is smaller.

2.2 Tomography

In this thesis, the tomographic reconstructions generated by the Tomotok tool described in Sect. 1.6 are used to find the tungsten concentration. The main algorithm for tomographic inversion is minimum Fisher regularisation with Tikhonov regularisation.

Data from foil bolometers (BLB), AXUV diodes (XVR), and soft X-ray (SXR) cameras are used. Data preprocessing is required before performing tomographic inversion. An example of raw data from a BLB cameras for discharge #37614 is shown in Fig. 2.19. Some camera channels need to be removed as they are considered dead. There is no signal on them, even though their LOS is directed towards the area where the plasma is expected. In some cases, it may occur that there is an offset on the channels that can be detected and estimated from the preplasma phase. The statistical error can also be determined from this phase as the standard deviation.

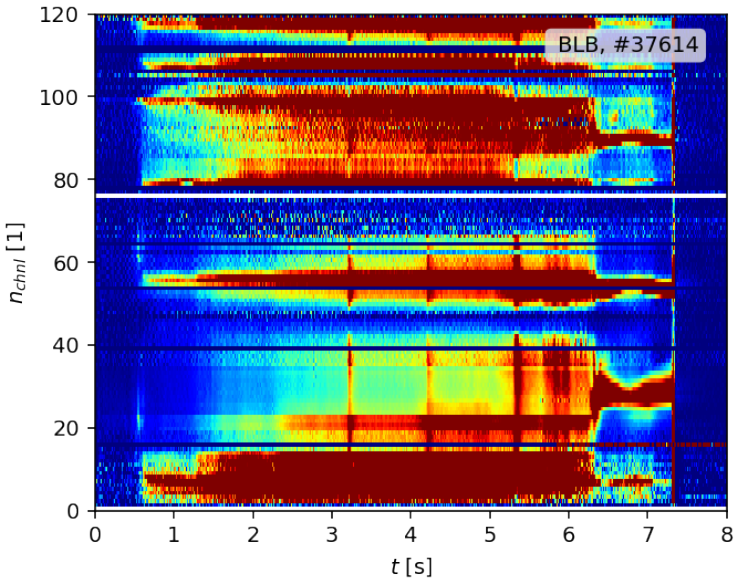

Figure 2.19: Raw data from BLB cameras from discharge #37614. The FHC camera has assigned channels 1 to 48, the FVC camera channels 49 to 80, the FDC camera channels 81 to 108, the FLX camera channels 109 to 116 and the FLH camera channels 117 to 120.

An example of tomographic reconstructions from the foil bolometer (BLB) and the soft X-ray cameras (SXR) for the 3.15 s time of the #37614 discharge are shown in Figs. 3.5 and 3.6, respectively. In the BLB tomogram, it is clear that most of the emission comes from the vicinity of the divertor. As shown in Fig. 1.3, the BLB camera array has a large coverage around the divertor, allowing us to reconstruct the details. Here, the MFR algorithm meets its limitations as it was developed primarily for soft X-ray data. Tomographic algorithms typically have a problem with large differences in emissivity, such as the small-volume region around the divertor versus the larger-volume main plasma. Since the absolute reconstruction error is similar for the higher-emissivity region as for the low-emissivity region, the relative error for bulk plasma will be large. At the same time, the integral along the LOS is affected by the error due to the high emissivity region [27]. For this reason, the tomographic reconstruction from foil bolometers may not be accurate.

Soft X-ray data are not affected by this issue. Therefore, details such as asymmetries in the profile can be reconstructed more easily. From Fig. 2.16, it is evident that on SXR cameras, emission can only be observed from a region with a temperature higher than 2.5 keV. This can be seen in the reconstruction in Fig. 3.6.

The retrofit of both tomographic reconstructions from Figs. 3.5 and 3.6 is presented in Fig. 2.20. Here, the last χ^2 is also plotted, which for an ideal reconstruction with well-estimated measurement error should be equal to one. Otherwise, it is either overfitting or underfitting. The poloidal flux contours from the EQH diagnostics were used to calculate the anisotropy matrix. A constant anisotropy coefficient $\eta = 3$ was chosen for tomographic reconstructions of foil bolometers and $\eta = 3.5$ for SXR cameras.

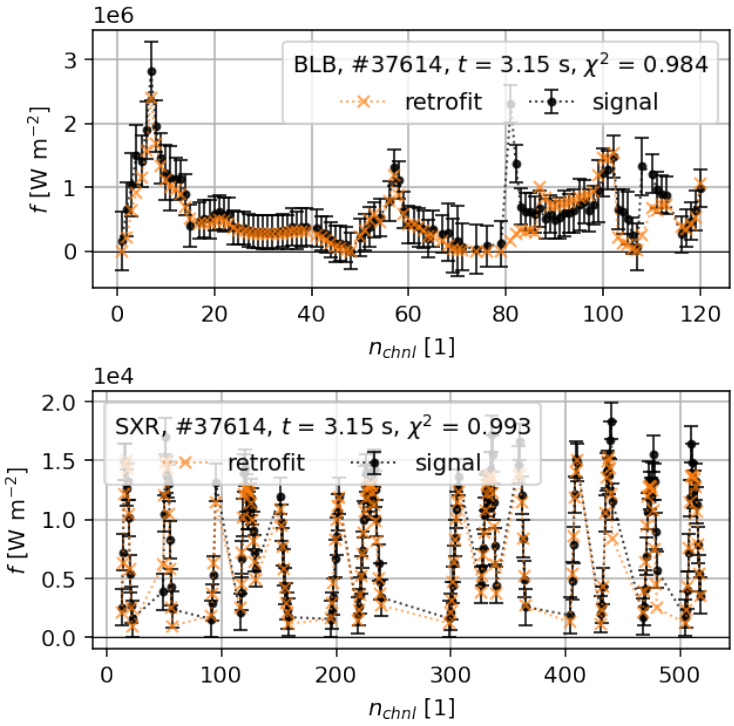

Figure 2.20: Retrofit of tomographic reconstructions from Figs. 3.5 and 3.6 .

The total radiated power of the tomographic reconstructions is compared with the BPD diagnostics in Fig. 2.21. For comparison, the processed signal $P_{rad} = P_{main}$

called the estimated radiated power in the main plasma and $P_{rad,tot} = P_{tot}$ called estimated total radiated power were selected from BPD. From the tomographic reconstructions, the radiated power in the whole plasma volume P_{tot} and then the power radiated outside the *main* region were extracted. The latter is shown in Fig. 2.22. The *main* region is determined by the position of the separatrix and the surface labelled $\rho = 0.85$, i.e. it depends on the given time. This region is determined differently for the BPD diagnostics.

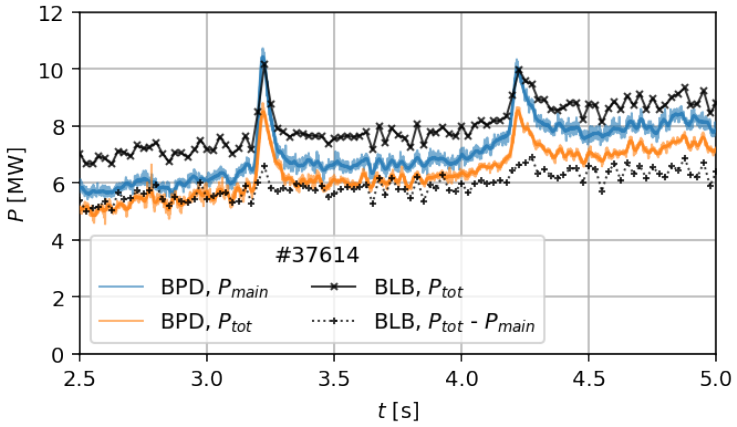

Figure 2.21: Total radiated power determined from tomography of bolometric cameras for different timesteps compared with BPD diagnostics.

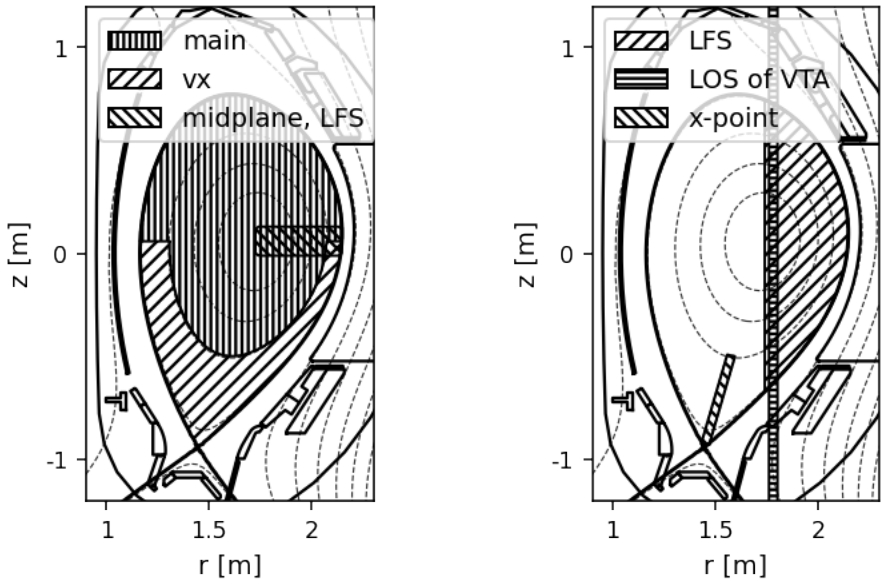

Figure 2.22: The regions used for evaluating the total radiated power from tomographic reconstructions.

The effect of radiation from the SOL on the total radiated power was discussed during the analysis of the obtained tomographic reconstructions. The question was whether most of the radiated power comes from the divertor region rather than from the core plasma. This can be observed and confirmed from the raw data. In Fig. 2.23 the decrease in emissivity in the SOL can be observed.

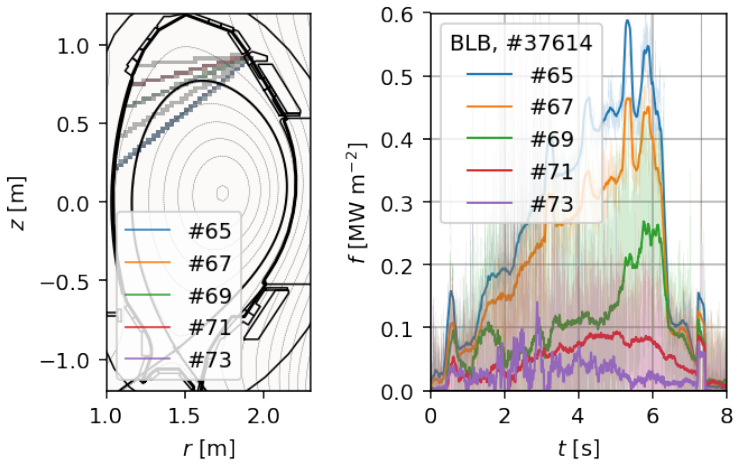

Figure 2.23: Selected channels from the FVC bolometric camera and the corresponding LOS capturing the amount of emissivity in the SOL.

The original objective of this thesis was the use of AXUV cameras for the evaluation of tungsten transport. The cameras can be calibrated using absolutely calibrated foil bolometers. However, as discussed in Sect. 1.5, the spectral response of the AXUV diodes is not precisely known. Because the degradation of the diodes is not the same for different parts of the spectrum and some areas of the spectral response function are not measured after degradation, there is a non-linear dependence.

The measured signals for the calibrated foil bolometer and AXUV diodes are compared in Figs. 2.24, 2.25, and 2.26. An analysis similar to that in Ref. [20] is also done for discharge #37614. The comparison is performed for channels with LOS passing through the plasma centre, X-point, and SOL on the LFS. For the plasma centre, the signal on the AXUV diodes is lower by a factor of 6.7, as can be seen in Fig. 2.24. In which spectral range the plasma emits can be determined from Fig. 2.12. In the comparison at the edge of the plasma in Figs. 2.25 and 2.26, it can be seen that the signal on the AXUV diodes is lower than on the foil bolometers even after applying a scaling factor of 6.7. This can be explained by the dominant emission in the VUV range, where the degradation of the diodes is severe. For the divertor region, the diode signals need to be re-scaled by a factor of up to 44.

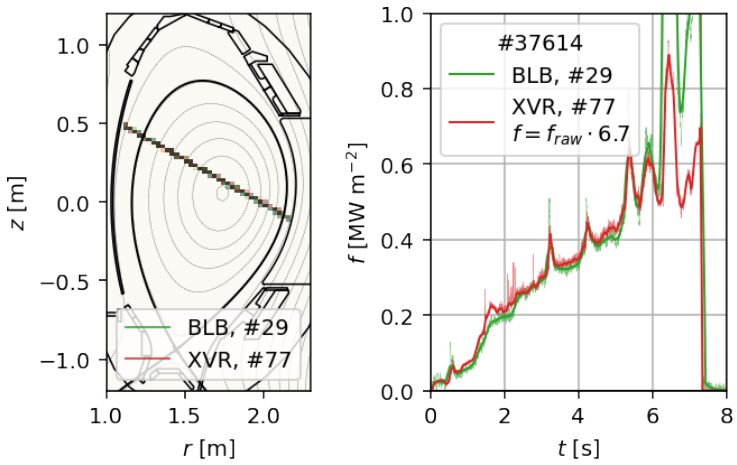

Figure 2.24: Comparison of bolometer and AXUV diode signals with the same LOS for identical discharge. The diode signals are rescaled by a factor 6.7.

The absolute calibration of AXUV diodes is described in Ref. [20]. The scaling factor for each channel can be found. This will be determined by comparing the measurements of the BLB and XVR cameras for nearby LOS. When applied, it can be found that the signals between the camera systems do not differ by more than 30 %. This difference is assumed to be due to the weakly varying VUV background. As a result, the scaling factor can be applied to the entire discharge. In order to analyse the different discharges, the factor must be recalculated.

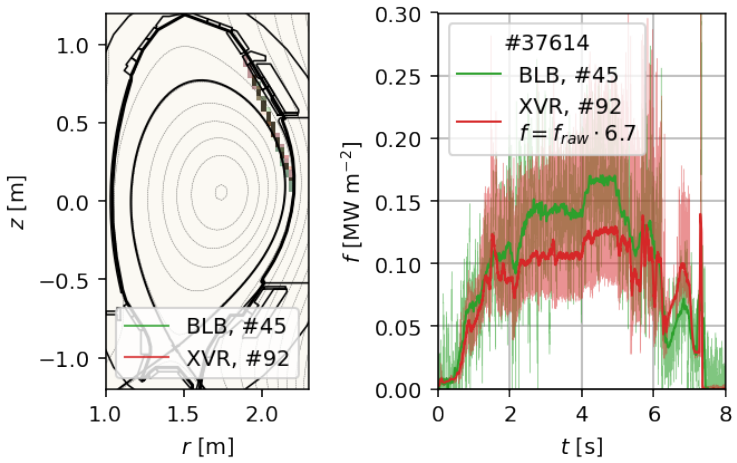

Figure 2.25: Comparison of bolometer and AXUV diode signals with the same LOS for identical discharge. The diode signals are rescaled by a factor 6.7.

The advantage of AXUV diodes over foil bolometers is the high sampling rate, which can reach up to 2 MHz. As a result, they can be used to analyse the emission during edge localised modes. Since this work is focused on LBO analysis, such high temporal resolution is not necessary.

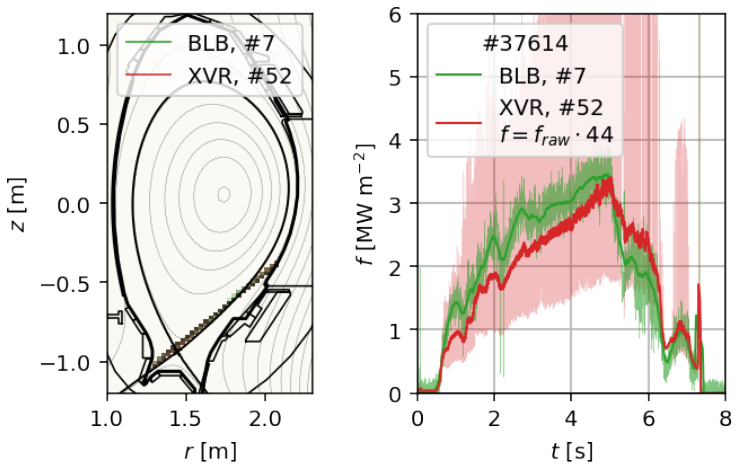

Figure 2.26: Comparison of bolometer and AXUV diode signals with the same LOS for identical discharge. The diode signals are rescaled by a factor 44.

Despite the complexity in correctly interpreting the AXUV diode data, tomographic reconstructions were obtained from them as shown in Fig. 3.7. A high emissivity region around the separatrix at the top of the profile can be seen there, whose origin has not been explained. An explanation could be a swapped order of the DHC channels, but since the channel numbers match those provided by the Diaggeom tool, this version is not true. Simultaneously, as a further argument, it can be said, for example, that the comparison in Figs. 2.24 and 2.26 is consistent. Yet, the quality of the reconstructions from the AXUV diodes seems to be questionable.

2.3 Summary

In this chapter, the procedure for obtaining the cooling factor from the photon emissivity coefficients is described. The publicly available data from the Open ADAS database, specifically PEC40, are adopted. A comparison of these PEC40 data with the new PEC50 data is discussed. These were obtained through personal communication with PD Dr. Thomas Pütterich. In Sect. 2.1.2 the arguments for the choice of PEC40 are made. Moreover, the calculation of the ionisation equilibrium and its comparison with Ref. [18] is discussed.

Furthermore, the possibility of using data from individual diagnostics for tomographic reconstruction is discussed in Sect. 2.2. Foil bolometers are chosen as the main diagnostics for the evaluation of tungsten concentration. Soft X-ray cameras provide reduced coverage in the pedestal region because of their spectral response. In contrast, while AXUV diodes have a wider range, unfortunately their spectral response is not well measured, and they need to be calibrated. Their advantage is their high sampling rate, but this is not necessary for the analysis of the LBO experiments. Absolutely calibrated foil bolometers will be primarily used for the following analysis.

Chapter 3

Results

The following chapter describes the discharge analysis done using the methodology described in the previous chapter. In Sect. 3.1 the calculated tungsten density profiles are presented according to the procedure described in Sect. 2.1.4. In Sect. 3.2 a similar analysis of radiation localised above the X-point as in Ref. [42] is performed. Tungsten transport is investigated, and transport coefficients are estimated in laser blow-off experiments in Sect. 3.3. The experimental results are compared with the Aurora transport model in Sect. 3.4.

3.1 Tungsten density profile

The following section focusses on the evaluation of the tungsten concentration from the tomographic reconstructions. The cooling factors from Sect. 2.1.4 are used to model the radiation. The calculated tungsten concentrations are validated using data from the Johann spectrometer (JOW) and the grazing incidence spectrometer (GIW). The tungsten concentrations obtained from these diagnostics are plotted in Fig. 3.1.

The GIW data labelled with *QC* are obtained from the quasi-continuum formed by the ionisation states W^{27+} to W^{35+}, which are located in the region marked in Fig. 3.2. This is the radiation in the range 50 Å. Furthermore, GIW diagnostics provide tungsten concentration values from the line radiation > 20 keV of ionisation states W^{40+} to W^{45+}. The Johann spectrometer also gives the concentration of tungsten, but from specific lines. It evaluates the state W^{44+} from the spectral line 5.749 Å, W^{45+} from the spectral line 5.723 Å and W^{46+} from the spectral line 5.687 Å. In Fig. 3.2 the fractional abundances of the mentioned states are plotted.

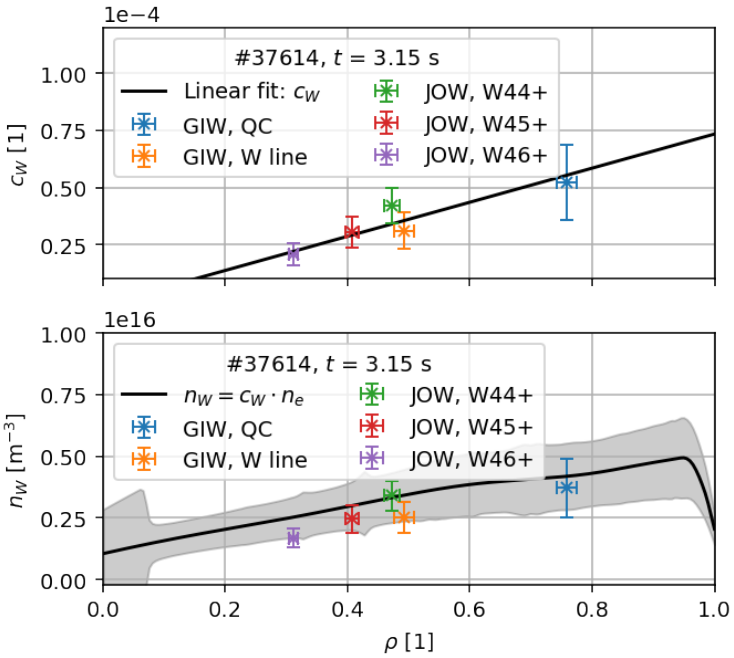

Figure 3.1: The tungsten concentration taken from the Johann spectrometer (JOW) and the grazing incidence spectrometer (GIW) is extrapolated by a linear fit. Based on the extracted concentration profile c_W, the density n_W is also estimated.

The tungsten concentration profile was obtained by linear regression of the points obtained from JOW and GIW. The radial positions of the points are loaded from the given diagnostics. Subsequently, the tungsten density $n_W = c_W \cdot n_e$ is calculated from the extrapolated concentration profile. The resulting profile is also plotted in Fig. 3.1 and is essentially illustrative in nature. Most likely, it does not correctly reflect the actual values at the edge of the plasma.

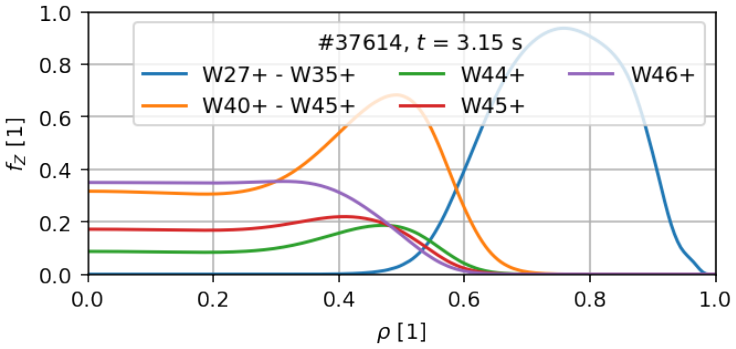

Figure 3.2: Fractional abundance relevant for diagnostics Johann spectrometer (JOW) and the grazing incidence spectrometer (GIW).

The tungsten density was analysed in the discharges #37614 (overview in Fig. 2.1), for #36476 (overview in Fig. 30) and #36486 (overview in Fig. 31). For discharge #37614, the first LBO was analysed, that is, times from $t = 3.15$ s to 3.3 s are considered. Selected tomographic reconstructions are shown in Fig. 3.3.

The tungsten concentration is determined from the emissivity Σ according to Eq. 1.43. Thus, a 2D tungsten density profile can be acquired directly as in Figs. 3.5, 3.6, and 3.7. For a given reconstruction node, the local electron temperature

and density are found, and then the W concentration. For subsequent analysis, a 1D density profile is produced. It is created using masks defined by the minimum and maximum radius values. These are additionally chosen as subsets of the regions denoted as *main* and *midplane* on LFS and plotted in Fig. 2.22 or as the hatched regions in Fig. 3.3. The constructed tungsten concentration profiles for discharge #37614 are plotted in Fig. 3.4. The cooling factor is used exclusively from the *cl*-resolved PEC40 data set.

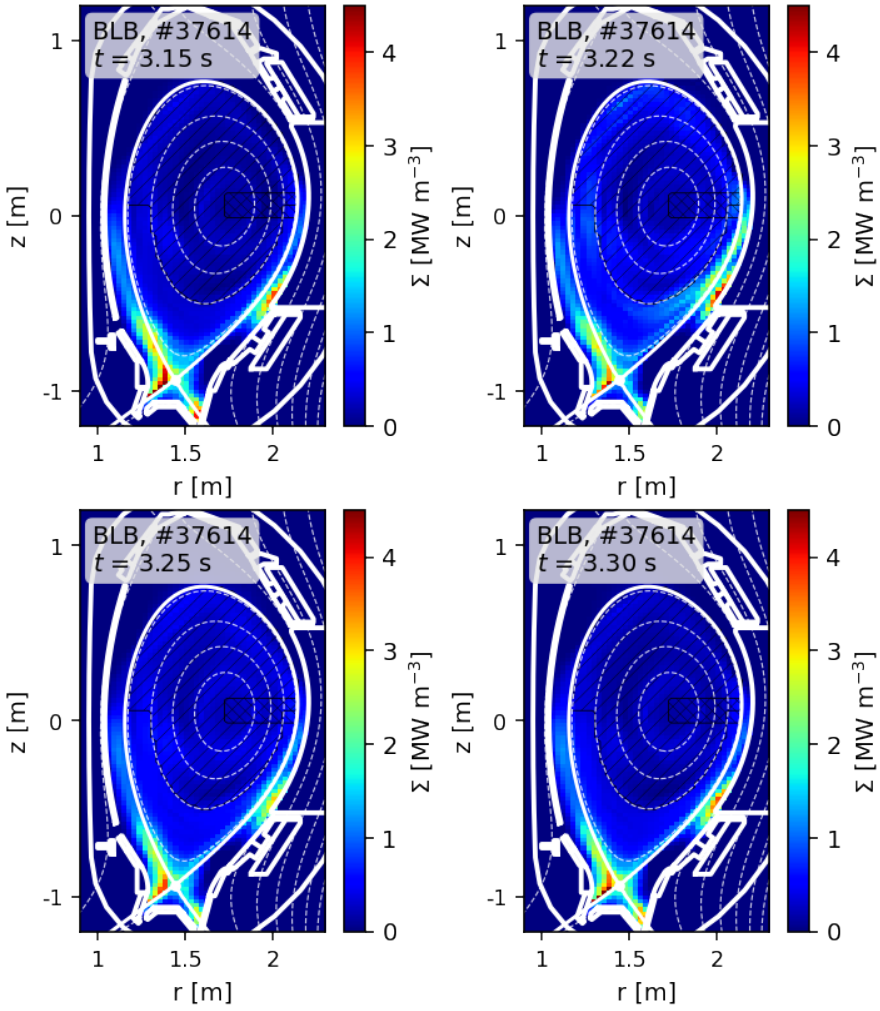

Figure 3.3: Selected tomographic reconstructions from BLB bolometric cameras for LBO analysis in the #37614 discharge. The resulting tungsten density profiles are shown in Fig. 3.4.

In Fig. 3.4, the profiles are evaluated for the *main* region and plotted using points with error bars that were determined as the standard deviation of the given masks. For the LFS *midplane* region, the profile is plotted in the same graph using dashed lines. This was done because of possible asymmetry that could affect the density profile. As can be seen from the plot, the asymmetry in the main region is not significant and does not change the impurity density values drastically.

Soft X-ray cameras detect radiation only from a region with a temperature higher than 2 keV. This means that the region they cover is well localised in space, as shown in Fig. 2.16. Thus, only values up to a radius of $\rho \approx 0.7$ are relevant. In the region $\rho = 0.7$ to $\rho = 1$, the values are strongly dependent on the spectral

response in Fig. 1.2, which is calculated using an analytical formula under certain assumptions.

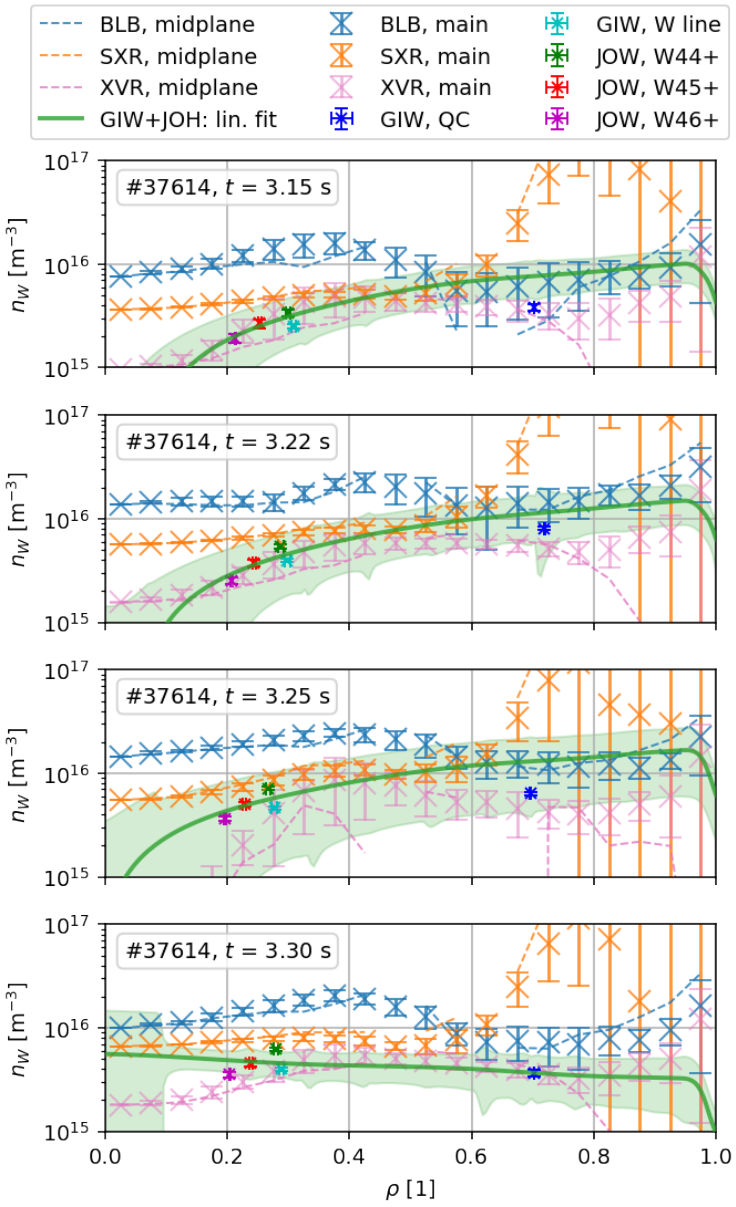

Figure 3.4: Tungsten density profile obtained from three different diagnostics: foil bolometers BLB, AXUV diodes XVR and SXR cameras. For different time steps, the profiles are calculated from the main and midplane regions shown in Fig. 3.4. A comparison is made with the results of the JOW and GIW diagnostics.

In addition, discrepancies can be observed in the evaluated concentrations from different diagnostics. An interesting difference is between the foil bolometer and the SXR cameras. The tungsten concentration in the bolometer results is approximately twice as high in the centre of the plasma. In general, the tungsten concentration of BLB is higher compared to other diagnostics. This is concerning since foil bolometers should be absolutely calibrated. Looking at Eq. 1.43, it can be deduced that the concentration estimate depends primarily on the quality of the tomographic reconstruction, on a correctly calculated cooling factor for the line and braking radiation, and on a correct electron density profile.

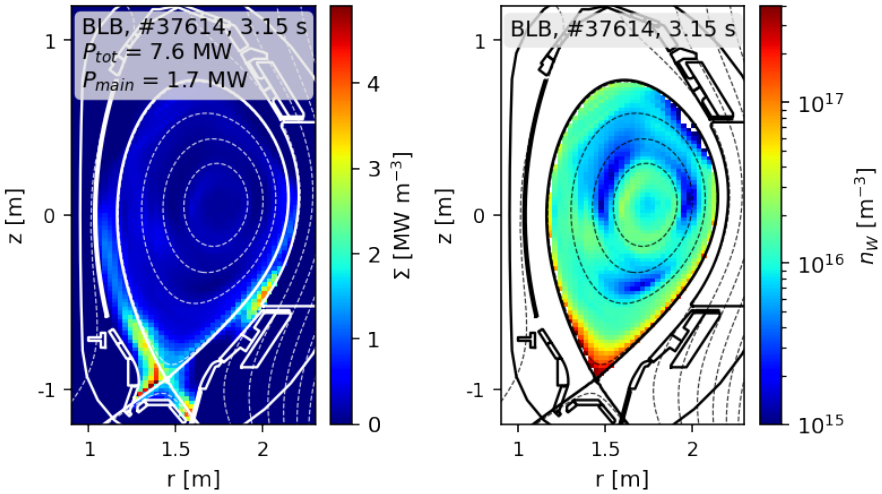

Figure 3.5: (a) example of tomographic reconstruction from BLB foil bolometers for time 3.15 s of discharge #37614. (b) calculated W concentration based on tomography from (a) and Eq. 1.43.

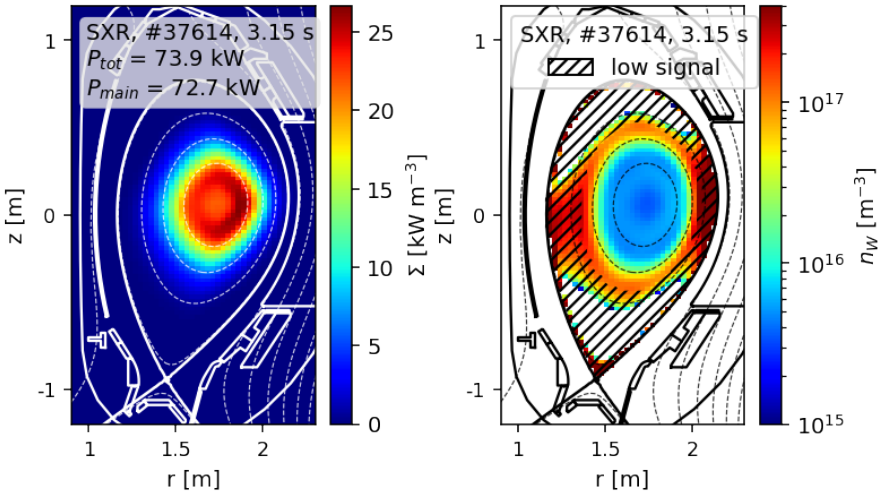

Figure 3.6: (a) example of tomographic reconstruction from soft X-ray cameras SXR for time 3.15 s of discharge #37614. (b) calculated W concentration based on tomography from (a) and Eq. 1.43.

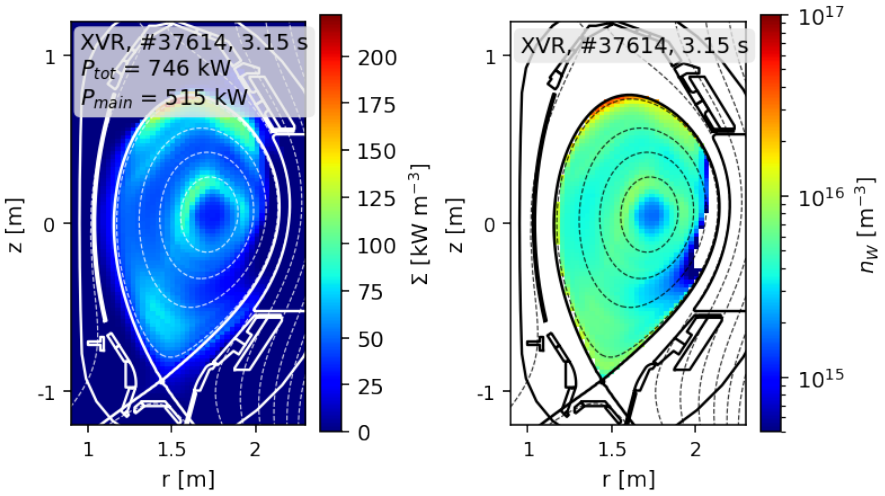

Figure 3.7: (a) example of tomographic reconstruction from AXUV diodes XVR for time 3.15 s of discharge #37614. (b) calculated W concentration based on tomography from (a) and Eq. 1.43.

For reasons previously outlined, the quality of the tomographic reconstructions may be insufficient. The high emissivity in the vicinity of the divertor causes a high absolute error in the plasma-centre region. From Fig. 2.20, the integral values of the retrofit appear to be in good agreement with the measured data. The SOL emission is probably not high enough to significantly affect the integral value, as shown in Fig. 2.23. The quality of the tomographic reconstruction cannot explain the difference of factor of two. The choice of the data set for calculating the cooling factor may also play a role. As can be seen in Fig. 2.17, and especially from Fig. 2.18, the difference in this region should again not be high enough to explain the difference. The braking radiation is included in the model and is not high enough to significantly affect the resulting concentration.

For verification of the method, a similar analysis was performed for discharges #36476 and #36486, which are presented in Figs. 30 and 31. For discharge #36476, the tungsten density values obtained using the same method are much more favourable. As can be seen in Fig. 34, the BLB and SXR values agree well for a large part of the profile (reconstruction in Figs. 32 and 33). The difference in the centre of the plasma can be explained by the hollow tungsten density profile. This can be seen in Fig. 30 on the GIW data from the signals evaluated from the quasi-continuum. There, an increase in time $t = 4$ s is seen, which accompanies an increase in ICRH power and a decrease in NBI power. The hollow profile probably causes the algorithm to fail to correctly evaluate the emissivity. At the point when the profile is more peaked, the BLB and SXR values are already in good agreement with each other. There is even agreement with the GIW and JOW diagnostics. Also, despite the large asymmetry at the edge, there is good agreement between the foil bolometer and the AXUV diodes. The asymmetry at the edge here is probably due to phantoms. These probably originate from channels with LOS directing to the divertor while passing through the plasma centre.

The second discharge mentioned is #36486, where the results are presented in Figs. 37 and 36. Approximately at time $t = 2.6$ s the tungsten density profile changes rapidly. The tungsten concentration profiles were analysed for times before and after this change. At time 2.2 s the agreement between the diagnostics is limited

by severe asymmetries. In the midplane region, there is reasonably good agreement between SXR and BLB in the regions $\rho = 0.3$ to 0.6. At time 3.2 s, the differences are already several orders of magnitude. Here, the tomographic reconstruction seems to fail, as can be seen, for example, from the BLB in the centre of the plasma.

3.2 Anisototropy analysis

The following section focusses on the modelling of radiation above the X-point. An analysis analogous to the one presented in the Ref. [42] is performed in this section. A cold region of high density is formed around the X-point. The energy is radiated here in a relatively small region. Thus, an asymmetry is created, which is the subject of the following analysis.

Similar to Ref. [42], a model that describes the radiated power P_x in the region of interest x in the vicinity of the X-point is presented:

$$P_x = L_W(n_{e,x}, T_{e,x}) \cdot n_{e,x}^2(T_{e,x}) \cdot c_{W,x} \cdot V_x, \tag{3.1}$$

where V_x is the volume of the area investigated. In this region, the uniform electron temperature $T_{e,x}$ and the density $n_{e,x}$ are considered. Since there is a constant pressure p_e along the magnetic field lines, the relation for $T_{e,x} n_{e,x} \approx \langle T_e \rangle_x \langle n_e \rangle_x$ is valid. The values of $\langle T_e \rangle_x$ and $\langle n_e \rangle_x$ are determined from integrated diagnostics (IDA) and represent the mean values for a given volume V_x. Here, it is assumed that the ion temperature T_i does not change much. To calculate $T_{e,x}$ and $n_{e,x}$, the parameter λ is introduced.

$$\begin{aligned} n_{e,x} &= \lambda \cdot \langle n_e \rangle_x \\ T_{e,x} &= \frac{\langle T_e \rangle_x}{\lambda} \end{aligned} \tag{3.2}$$

In the article Ref. [42] the constants $T_{e,x} = 7$ eV is taken. In this thesis, the parameter λ is left arbitrary and is expected to be between 1 and 10. The asymmetry in the 2D density profile of tungsten described by the parameter μ is also considered.

$$n_{W,x} = \mu \cdot \langle n_W^{BLB} \rangle_x \tag{3.3}$$

Thus, we can determine the density of tungsten $n_{W,x}$ in the vicinity of the X-point based on the density of $\langle n_W^{BLB} \rangle_x$ determined from the foil bolometer (BLB) from the region *main* only, which is plotted in Fig. 2.22. The tomographic reconstruction was then divided into several regions according to the degree of anisotropy α, defined as follows:

$$\alpha = \frac{\langle \Sigma_{BLB} \rangle_x}{\langle \Sigma_{BLB} \rangle_{FS,main}}, \tag{3.4}$$

where $\langle \Sigma_{BLB} \rangle_x$ is the mean value of the emissivity at a given node of the reconstruction and $\langle \Sigma_{BLB} \rangle_{FS,main}$ is the mean value in the *main* region along the flux surface that passes through the given node x. Regions defined by a given α value are created, for example, as in Fig. 3.8.

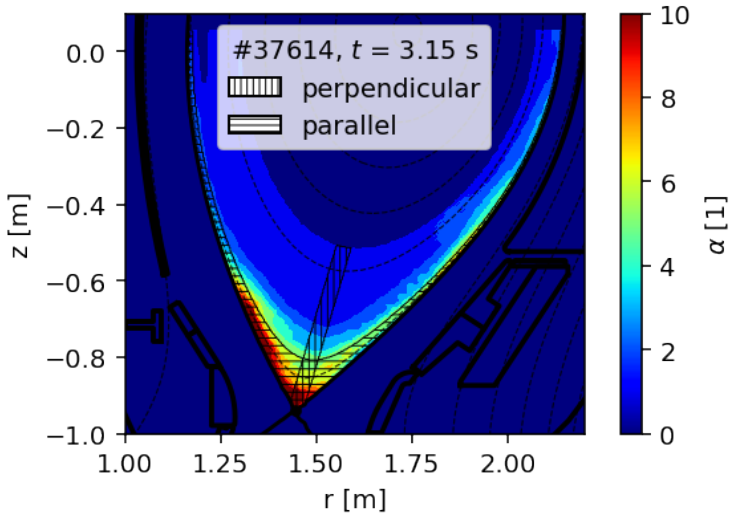

Figure 3.8: The regions with anisotropy from the foil bolometer tomographic reconstruction for time 3.15 s of discharge #37614 defined by the α coefficient from Eq. 3.4. Parallel and perpendicular masks are shown.

The regions for values in the range $\alpha = 1$ to 10 are defined. For each of these regions, a parameter scan of λ and μ is performed to produce a map as in Fig. 3.9. The map is composed of the values of the modelled radiated power P_x from the volume V_x for a given choice of the anisotropy parameters λ and μ. The contour of the radiated power of the volume V_x measured by the foil bolometers P_{BLB} is plotted in black on the map.

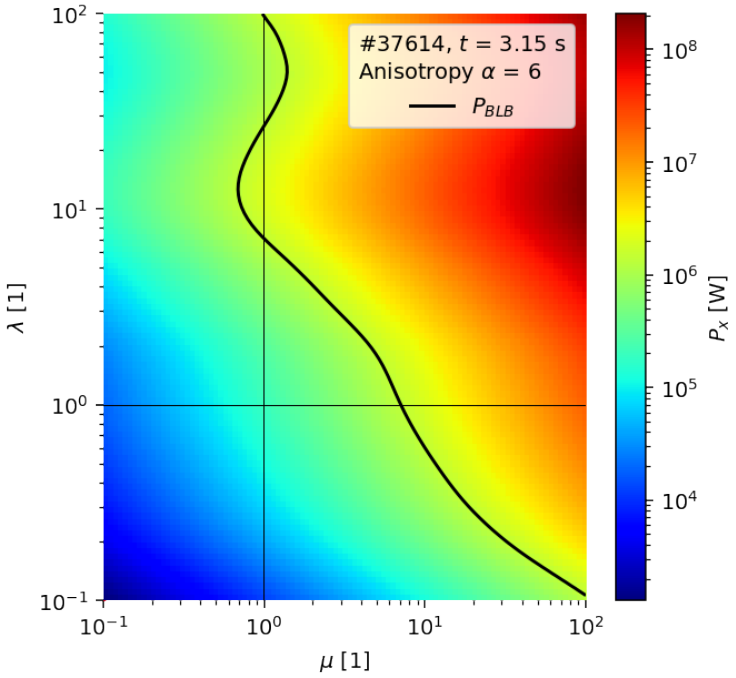

Figure 3.9: The values of the modelled radiated power P_x from the volume V_x for a given selection of the anisotropy parameters λ and μ. The contour with the value of the radiated power from the volume V_x measured from the foil bolometer tomography P_{BLB} is plotted in black.

From Fig. 3.9 it is clear that there is a whole set of points λ and μ for which the equivalence of the modelled and measured radiated power $P_x = P_{BLB}$ can be satisfied. An analogous analysis is performed for all regions in Fig. 3.8. In the parametric scan of Fig. 3.10, only the contours of the measured radiated power are plotted. Here, it can be seen that for low anisotropy of emissivity α the contours are near the point $(1; 1)$.

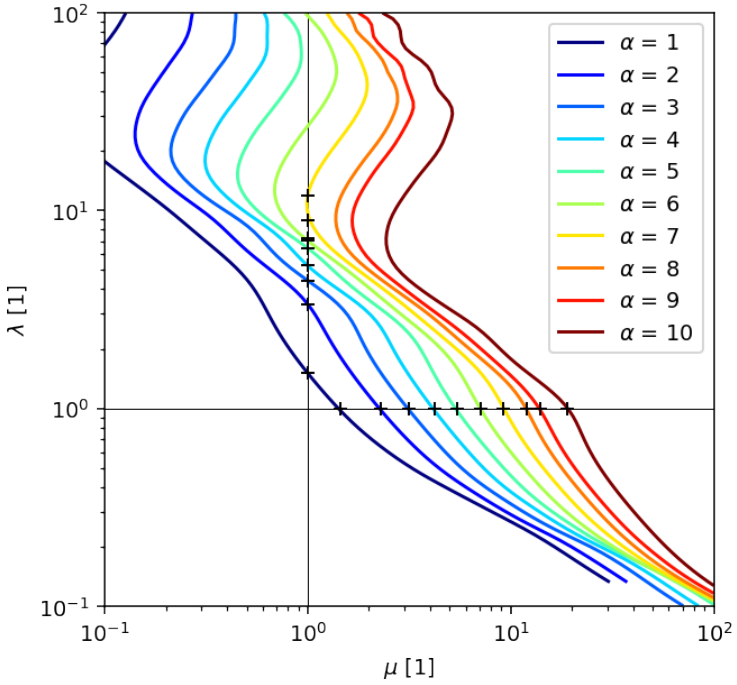

Figure 3.10: Contours of the measured radiated power for different values of the emissivity anisotropy coefficient α. The data are taken for a time step 3.15 s of the discharge #37614.

From the set of possible λ and μ, two hypotheses are investigated in detail. The first is the hypothesis $\lambda = 1$, which states that the anisotropy in the emissivity profile is purely due to the anisotropy of the tungsten density profile, which is given by the parameter μ. The intersection of the contours with $\lambda = 1$ gives the expected value of this parameter. The second hypothesis is that all anisotropy is caused by the electron temperature and density and that the tungsten density profile is uniform, that is, $\mu = 1$. Similarly, we can find the value of λ as an intersection.

These two hypotheses represent the most extreme cases, indicating the boundaries within which the true values are present. For both of these hypotheses, one can find the corresponding profiles of the electron density $n_{e,x}$, the temperature $T_{e,x}$ or the tungsten density $n_{W,x}$. Consequently, the data are shown in Figs. 3.11, 3.12, and 3.13.

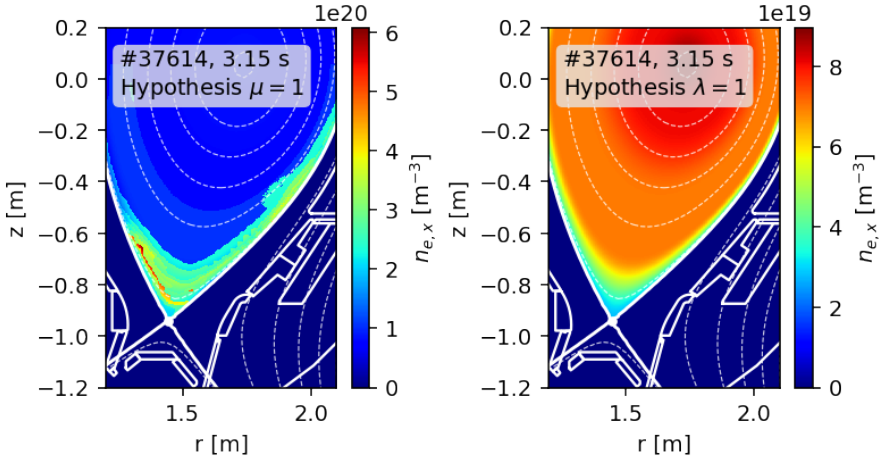

Figure 3.11: Electron density $n_{e,x}$ profile assuming the hypothesis for the anisotropy coefficients $\mu = 1$ and $\lambda = 1$.

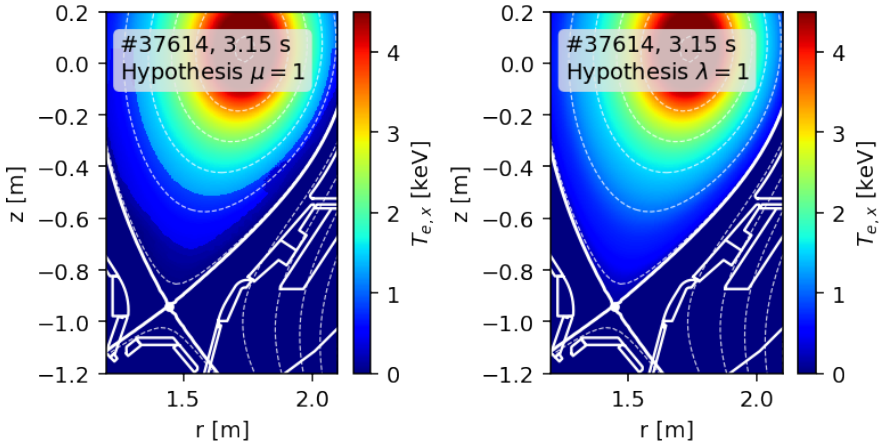

Figure 3.12: Electron temperature $T_{e,x}$ profile assuming the hypothesis for the anisotropy coefficients $\mu = 1$ and $\lambda = 1$.

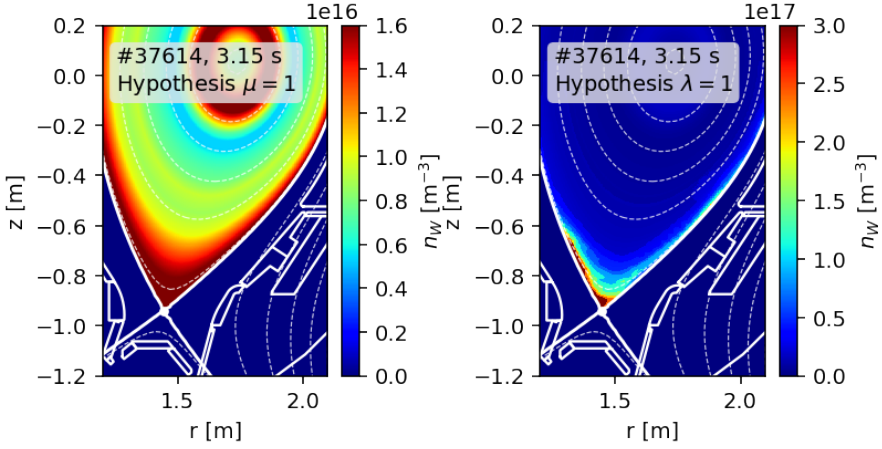

Figure 3.13: Tungsten density $n_{W,x}$ profile assuming the hypothesis for the anisotropy coefficients $\mu = 1$ and $\lambda = 1$.

The validity of these hypotheses can be verified in some way. A comparison with Divertor Thomson scattering (DTS) was considered. Unfortunately, the LOS of DTS in all discharges passes through the X-point and not through the core plasma. For comparison, Vertical Thomson Scattering (VTA) was chosen, with the LOS plotted in Fig. 3.14. This is divided into several core scattering volumes, which are also marked in this figure.

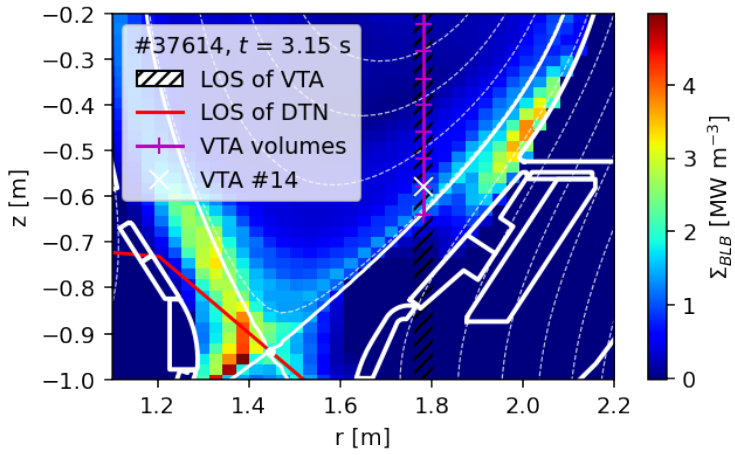

Figure 3.14: LOS of Vertical Thomson scattering (VTA) and Divertor Thomson scattering (DTS) highlighted in the tomographic reconstruction from foil bolometers for discharge #37614.

Along the LOS of the VTA diagnostics, a similar analysis was performed as for the α anisotropy coefficients. Again, two hypotheses were considered, that is, $\lambda = 1$ and that the anisotropy is due purely to the concentration of W, and a second hypothesis that $\mu = 1$ and that the anisotropy is due to density and temperature anisotropy. The profiles for both hypotheses are plotted in Figs. 3.15 and 3.16, where in the first plot a comparison with the vertical Thomson scattering is made.

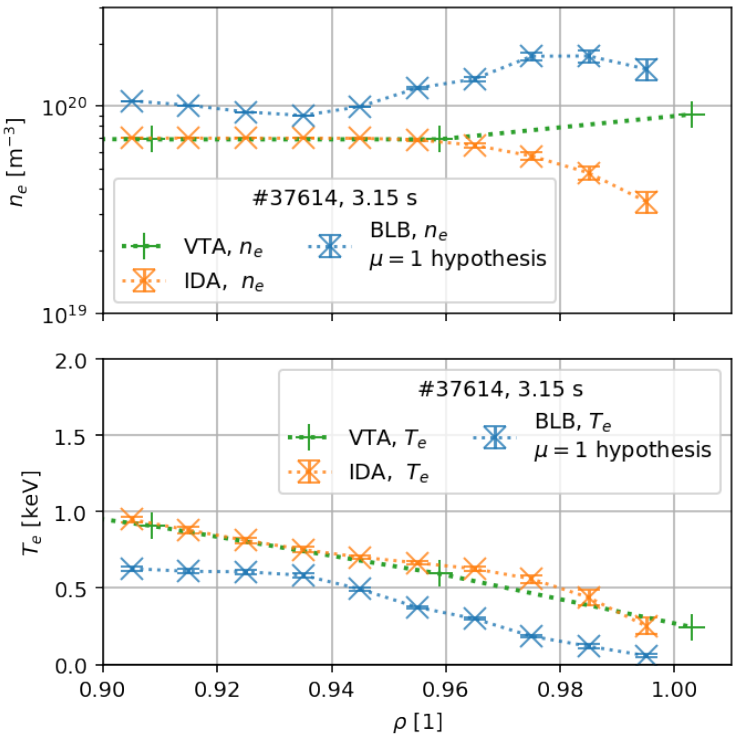

Figure 3.15: Electron density $n_{e,x}$ and temperature $T_{e,x}$ profile assuming the hypothesis for the anisotropy coefficients $\mu = 1$, for the IDA profile and from the vertical Thomson scattering for discharge #37614.

This asymmetry analysis is based on data obtained from integrated data analysis (IDA). This is based on data from lithium beam diagnostics (LIB), DCN interferometers, ECE, and Thomson scattering (VTA). For this reason, the comparison of IDA with VTA may not be relevant. However, from Fig. 3.15, it seems that the hypothesis of $\lambda = 1$ is more plausible.

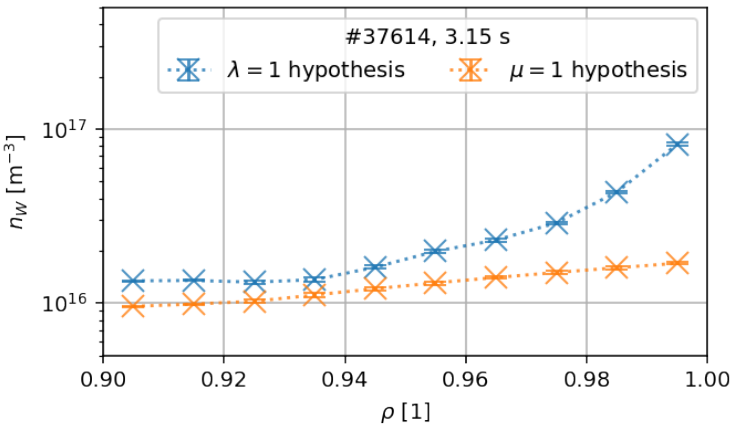

Figure 3.16: Tungsten density $n_{W,x}$ profile assuming the hypothesis for the anisotropy coefficients $\mu = 1$ and for $\lambda = 1$ for discharge #37614.

3.3 Transport analysis

The following section focusses on the calculation of transport coefficients, which are explained in Sect. 1.7. In the previous section, the procedure to obtain the tungsten density profile from computer tomography has already been described. Now, the transport coefficients D and V are obtained. A total of three LBO experiments are processed in discharges #37614 and #37639, which are summarised in Figs. 2.1 and 29. The analysis of these discharges is divided into two parts. The first part deals with the steady-state phase before the LBO, from which only a fraction of V/D can be obtained. In the second part, the exponential decays of the W concentration following the LBO are treated, which are driven by the outward flux. For these, it is already possible to separate and quantify the diffusion coefficient D and the drift velocity V.

The phase before the LBO is chosen as close as possible to the LBO itself, but in a way that is not affected by it. As already mentioned, this is a steady state phase in which we assume $\frac{\partial n_W}{\partial t} = 0$. At the same time, the source term $Q_W = 0$ is not assumed in this phase. Applying these observations to Eq. 1.61 the following is obtained:

$$0 = -\frac{1}{r}\frac{\partial}{\partial r}\left(r \cdot \Gamma_W\right), \tag{3.5}$$

where Γ_W is the flux density of tungsten. Since Γ_W cannot diverge at $r = 0$, it must be true that $\Gamma_W = 0$. From Eq. 1.7.3 then it is straightforward to deduce that:

$$\frac{V}{D} = \frac{\partial n_W}{\partial r} \cdot \frac{1}{n_W}. \tag{3.6}$$

In other words, from the measured W profile, this ratio of diffusion coefficients can be calculated. In the numerical calculation, the derivative on the right-hand side can be replaced as numerical differentiation and the central difference formula can be chosen:

$$\frac{\partial n_W}{\partial r}(t) \approx \frac{n_{t,r+1} - n_{t,r-1}}{2\Delta r}. \tag{3.7}$$

The method described was applied for the three LBOs mentioned above. In Fig. 3.17 the procedure is demonstrated for the first in discharge #37614 at time $t = 3.15$ s. For the analysis, 10 equally spaced time steps from 3.12 s to 3.18 s are selected. They are plotted by vertical lines on the graph. In this region, the temperature and density are nearly constant as for the rest of the LBO.

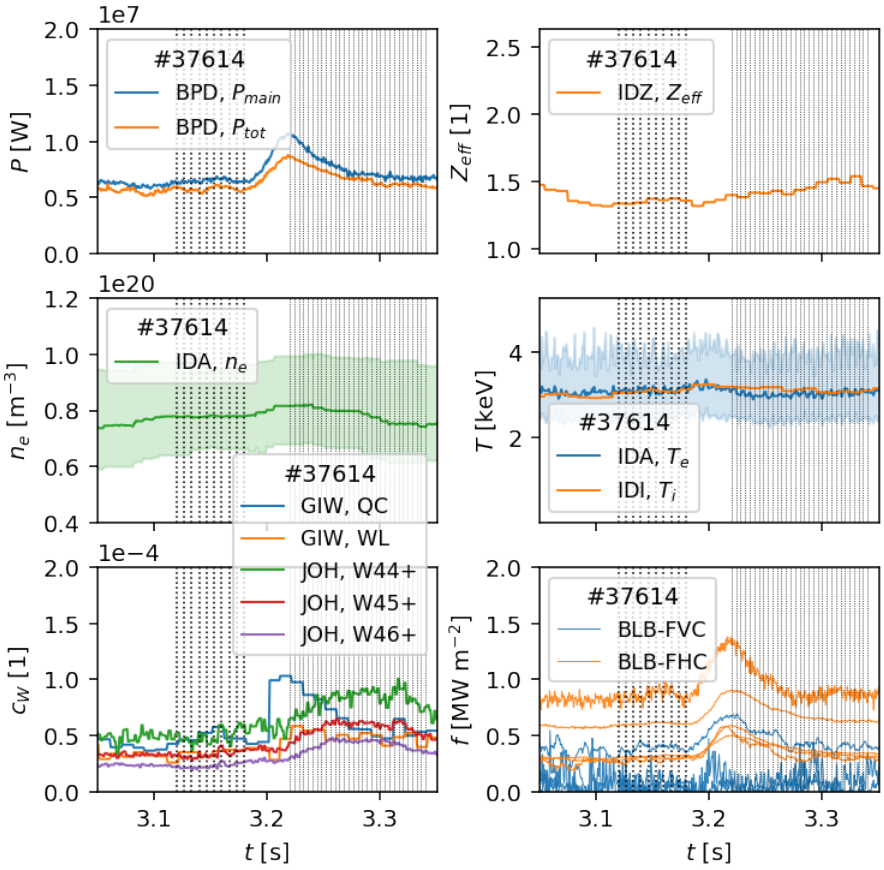

Figure 3.17: Overview of one of the three analysed LBOs in discharge #37614 at a time $t = 3.15$ s. (a) Total radiated power P_{tot} and radiated power P_{main} in main plasma from BPD. (d) Electron temperature T_e and (c) density n_e from IDA integrated data analysis and (d) ion profile T_i from IDI. (e) Tungsten concentration from Johann spectrometer JOW from single line diagnostics and the grazing incidence spectrometer GIW from quasicontinuum QC and line emission WL. (f) Selected channels from foil bolometers of vertical camera FVC and horizontal camera FHC.

The calculated tungsten profiles n_W including their approximation of the derivative $\mathrm{d}n_W/\mathrm{d}r$ are given in Fig. 3.18 for all time steps. The quantities are drawn as a function of the radial position $R - R_0$, not on the normalised radius ρ. The density profiles are not exactly constant in time as seen in the second plot. As discussed in Sect. 1.6, the selected algorithm for tomographic reconstruction may fail for hollow profiles and may incorrectly evaluate the concentration at the centre. An increase in density in the centre causes the profile to be less peaked, which flattens the density derivative. For the times mentioned, the V/D fraction is calculated and the values are averaged. The results for the first LBO are also shown in Fig. 3.18. A similar analysis is performed for the second LBO from discharge #37614 and the third LBO from #37639. The results are presented in Figs. 40 and 41, respectively.

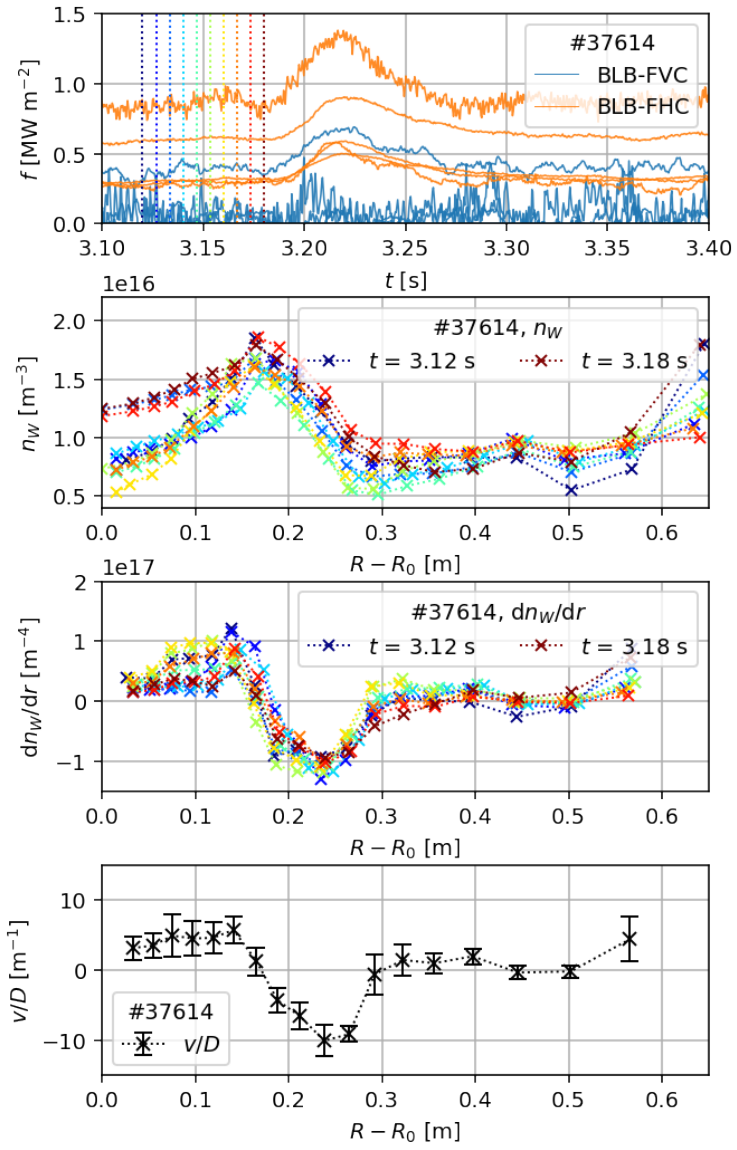

Figure 3.18: Analysis of the steady-state phase, with the resulting fraction V/D for the first LBO in #37614. The calculated tungsten profiles n_W including their approximation of the derivative $\mathrm{d}n_W/\mathrm{d}r$. The selected time steps are colored in the first graph.

The assumption that $\frac{\partial n_W}{\partial t} = 0$ is no longer valid for processing the LBO phase with exponential decay. In the plasma edge, the source term is neglected on these timescales and thus $Q_W = 0$ still holds. This means that the particle flux density Γ_W is no longer nonzero. This can be calculated, for example, from Eq. 1.61 with the introduction of the quantity $F_W = r\Gamma_W$:

$$\frac{\partial n_W}{\partial t} = -\frac{1}{r}\frac{\partial}{\partial r}F_W. \tag{3.8}$$

Numerically, the time derivative can be calculated similarly as follows:

$$\frac{\partial n_W}{\partial t}(r) \approx \frac{n_{t+1,r} - n_{t-1,r}}{2\Delta t}. \tag{3.9}$$

The W density evolution is illustrated in Fig. 3.19. It shows the transport of W towards the centre of the plasma out of the separatrix in time. The hatched areas

mark the regions that are not used for data processing. The profile is too flat in this area, or at the given time the tungsten has not yet penetrated to the centre. For the analysis of the discharge #37614, the frequency of the time steps is chosen so high that it is not possible to analyse out of individual ELMs. The SXR cameras are sensitive to plasma with an electron temperature of 2.5 keV and above.

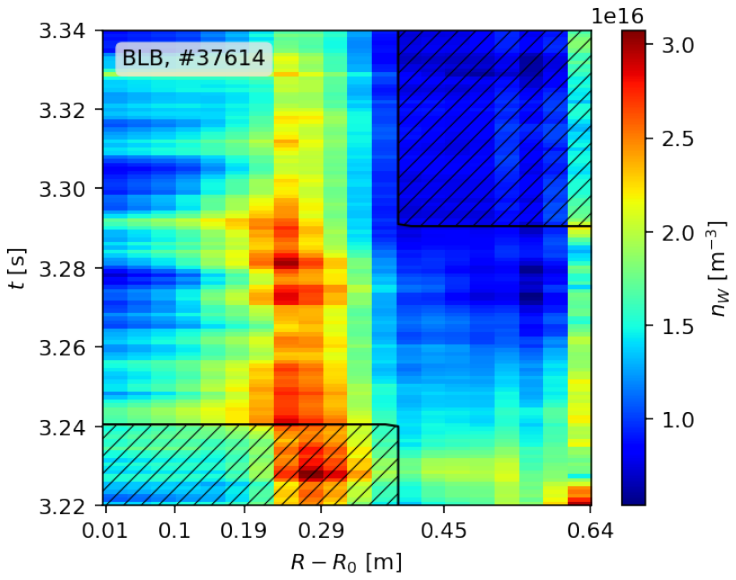

Figure 3.19: Time evolution of tungsten density profile obtained from tomography of foil bolometers. The hatched areas mark the regions that are not used for data processing.

The calculated tungsten profiles n_W, their derivative $\mathrm{d}n_W/\mathrm{d}r$, and the particle flux density Γ_W are plotted in Fig. 3.20. From Eq. 1.7.3 then it is straightforward to deduce that:

$$\frac{\Gamma_W}{n_W} = -D\left[\frac{\partial n_W}{\partial r}\frac{1}{n_W}\right] + V \tag{3.10}$$

The time range for the analysis was chosen to avoid interference with the first phase of the LBO with a rapid increase in the concentration of W. In Fig. 3.20 the selected time steps for which the values were calculated are highlighted. For a lower frequency of time steps, these are selected so that they are not influenced by the edge-localised mode, as shown in Fig. 39. This is motivated by the reduction of fluctuations in the density profile. Time evolutions were taken for each radial position, and a fit was performed according to Eq. 3.10 to obtain the diffusion coefficient D and the drift velocity V.

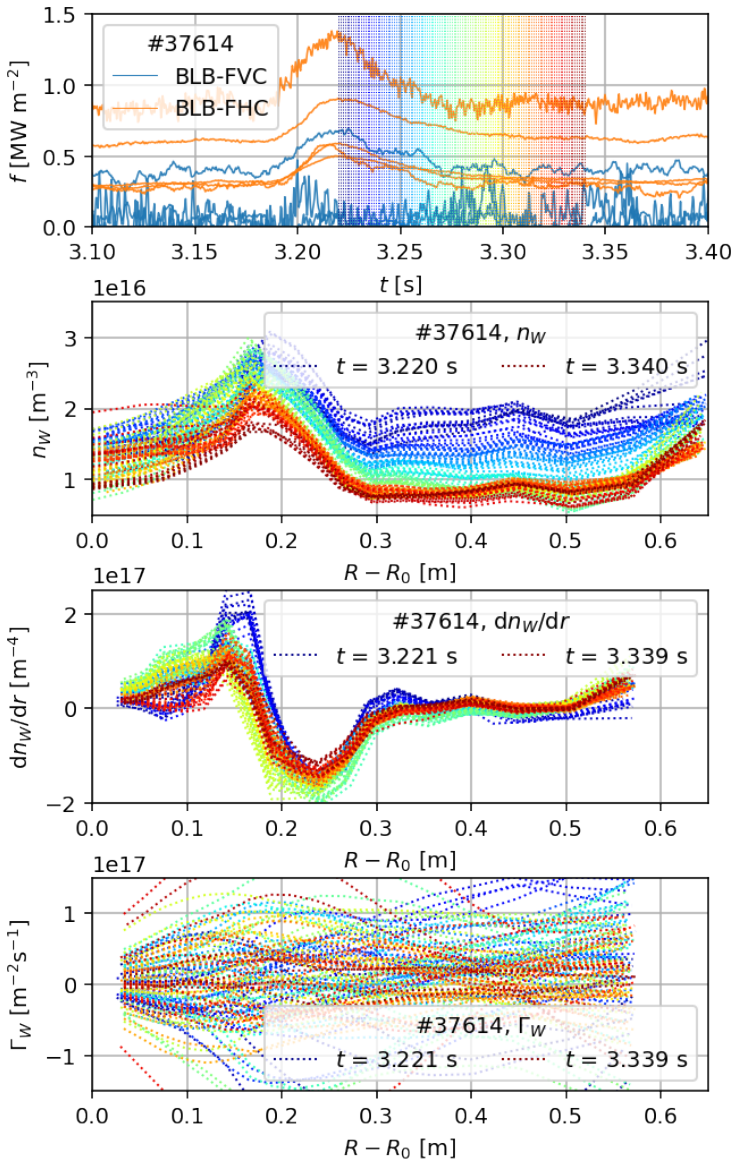

Figure 3.20: The calculated tungsten profiles n_W, their derivative $\mathrm{d}n_W/\mathrm{d}r$ and the particle flux density Γ_W for the LBO phase analysis. The selected time steps are colored in the first graph.

The results of the linear fit, that is, the transport coefficients obtained D and V, are plotted in Fig. 3.21. The V/D ratios are also calculated in order to make a comparison with the steady-state phase analysis before LBO. The results of both methods are in very good agreement with respect to fluctuations caused either by reconstruction quality or by changes in the plasma. An analogous analysis is performed for the second LBO from #37614 and the third LBO from #37639. The results are shown in Figs. 40 and 41, respectively.

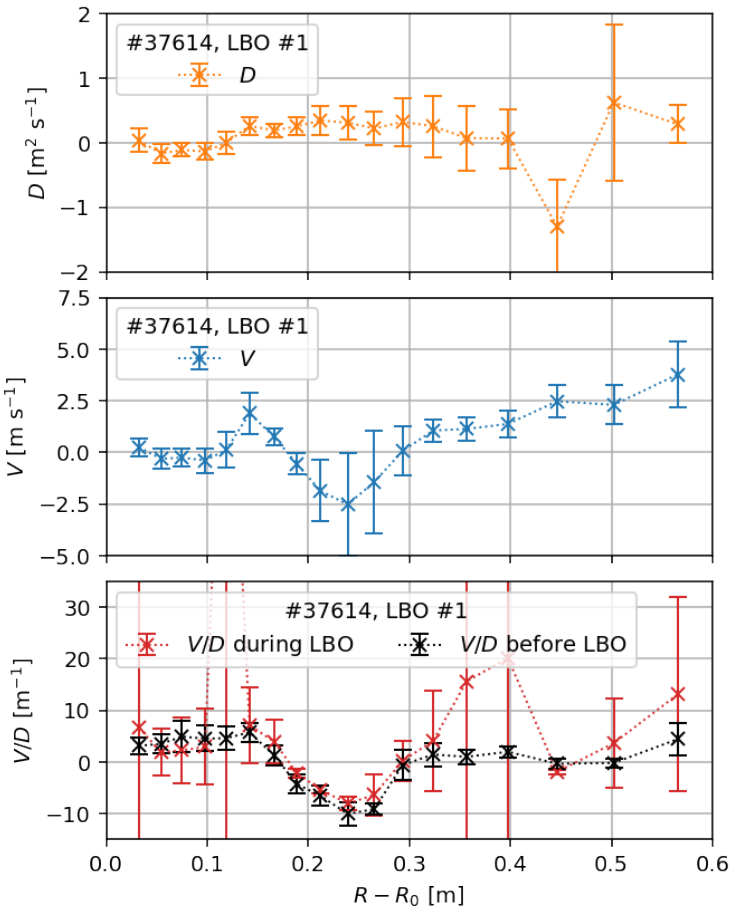

Figure 3.21: The diffusion coefficient D and drift velocity V obtained from the analysis during LBO of the discharge #37614. A comparison is made with the steady-state pre-LBO transport analysis using the V/D ratio.

The whole procedure is repeated for the phase before and during the LBO for the soft X-ray cameras. The temporal evolution of the W density profile is plotted in Fig. 3.22. Note that because of the spectral response of the SXR cameras, the measurement is not relevant for the pedestal.

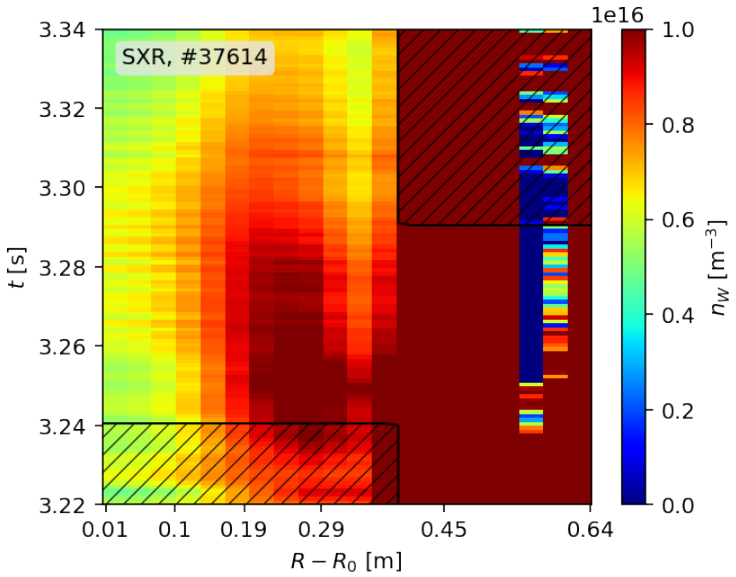

Figure 3.22: Time evolution of tungsten density profile obtained from tomography of soft X-ray cameras. The hatched areas mark the regions that are not used for data processing.

The transport coefficients D and V can then be obtained using the procedure described above. The results are plotted in Fig. 3.21 . Again, a very good agreement of the V/D measurements in both phases can be observed. The diffusion coefficient D seems to be higher in the centre for the SXR camera measurements than for the bolometers. For the convective velocity V, both diagnostics measure a similar trend.

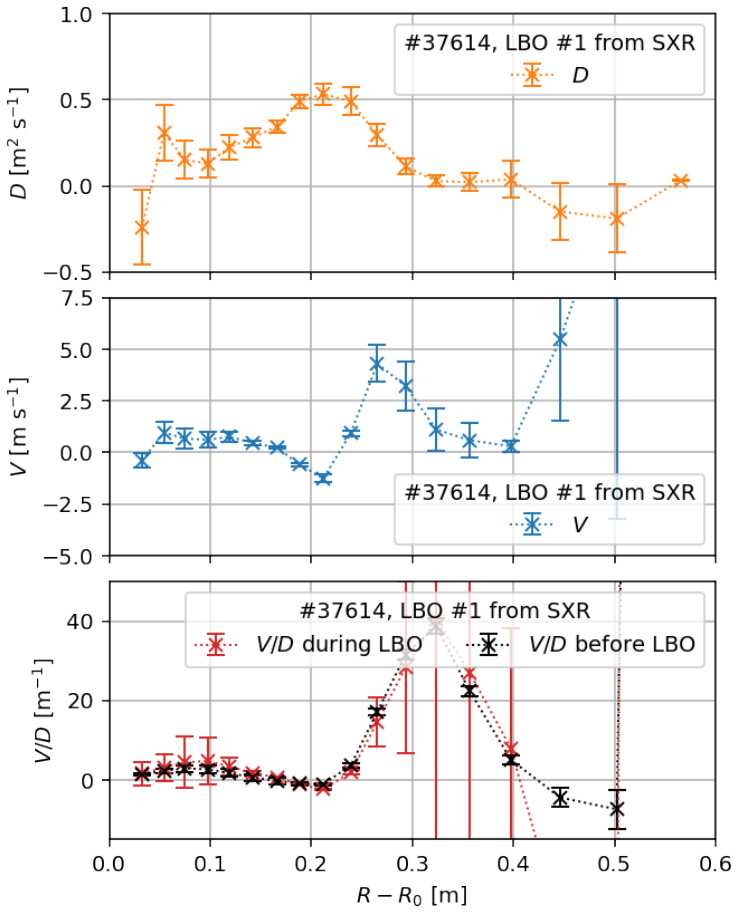

Figure 3.23: The diffusion coefficient D and velocity V obtained from the analysis during LBO of the discharge #37614. A comparison is made with the steady-state pre-LBO transport analysis using the V/D ratio.

3.4 Transport model

From the theory in Section 1.7, the collisionality for deuterium and tungsten is calculated in Fig. 3.24. According to the results plotted in this graph, tungsten is in the plateau regime for most of the profile, except for the pedestal. In most cases, tungsten should be present in the Pfirsch-Schlüter regime.

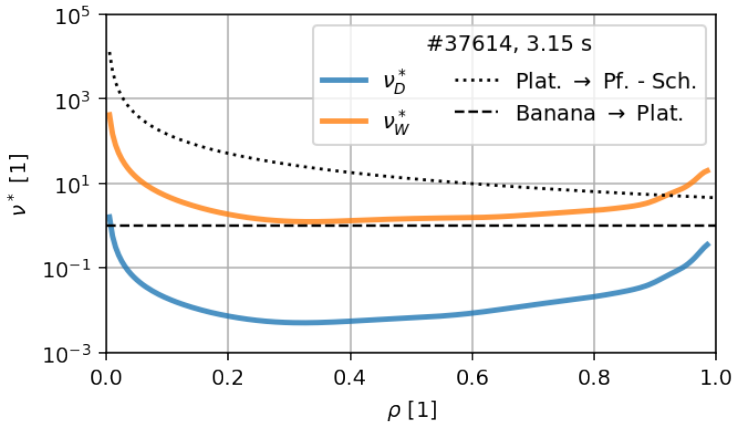

Figure 3.24: The calculated collisionnality for deuterium ν_D^* and tungsten ν_W^* for the discharge profile #37614 at time 3.15 s. The boundaries for the different collisionality regimes are also given, from the bottom: banana, plateau and Pfirsch-Schlüter regime.

From the theory in Section 1.7, the ratio of the transport coefficients V^{PS}/D^{PS} was obtained for the Pfirsch-Schlüter regime. These are calculated from Eq. 1.76 and shown in Fig. 3.25. The transport coefficients for banana-plateau could also be obtained from Ref. [32]. Since it is necessary to obtain the viscosity coefficients of the impurity to calculate them, it was more straightforward to use one of the transport codes, such as the Aurora package with its FACIT submodule.

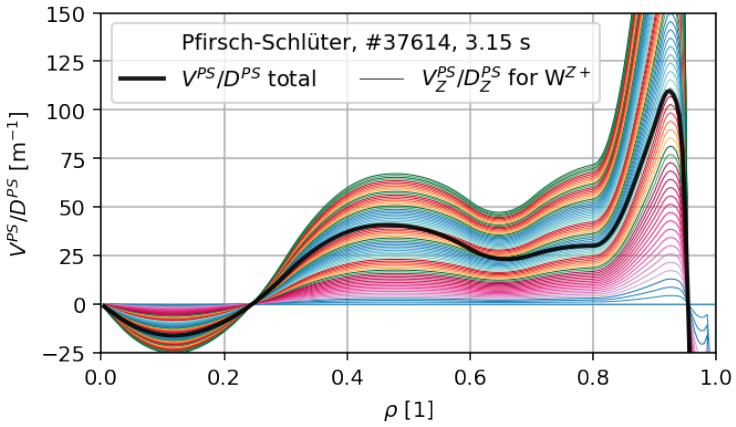

Figure 3.25: The calculated ratio of the transport coefficients V^{PS}/D^{PS} for the Pfirsch-Schlüter regime from Eq. 1.76.

The Aurora package was used to simulate heavy-ion transport and emission. It contains a 1.5D impurity transport forward model as well as the Fast and Accurate Collisional Impurity Transport (FACIT) package [43, 35, 44]. Using the FACIT model, it is possible to calculate the coefficients of neoclassical diffusion D^{neo} and convection V^{neo}, which can then be used to model transport. It also uses ADAS data to model the radiation.

The OMFIT tool, specifically the EQDSK, is used to load the equilibrium data. Data are loaded for discharge #37614 of the AUG tokamak as output from the numerical code METIS and as experimental data from the integrated diagnostics of IDA and IDI. All quantities are mapped to the normalised flux coordinates ρ_{pol}

from Eq. 1.17. Here, it must be taken into account that Aurora uses the CGS units for inputs, while FACIT uses the SI system.

The second step is the specification of the ion species for simulation. Only one impurity is used in the model, tungsten. An impurity source 0.1 cm away from the LCFS with a constant source rate of $3 \cdot 10^{17}$ s^{-1} is prescribed. In the future, it is also possible to prescribe a time-evolving source for laser blow-off. In this application, however, only the steady state is considered. For consistency with the rest of this thesis, the PEC40 ADAS data and the SCD50 and ACD50 data are also used to calculate the emission and ionisation balance, respectively.

Subsequently, the charge-dependent collisional transport coefficients were calculated using the FACIT model. These coefficients will then be used as input to the Aurora package to solve the transport. First, the neoclassical transport coefficients D_Z^{neo} and V_Z^{neo} in Fig. 3.26 for each ionisation state are calculated. The plasma rotation effect, taken from the IDI integrated diagnostics, is included in their calculation. The effect of rotation is dominant especially for heavy impurities. Based on the ionisation equilibrium, the total diffusion coefficient D^{neo} and the drift velocity V^{neo} are calculated.

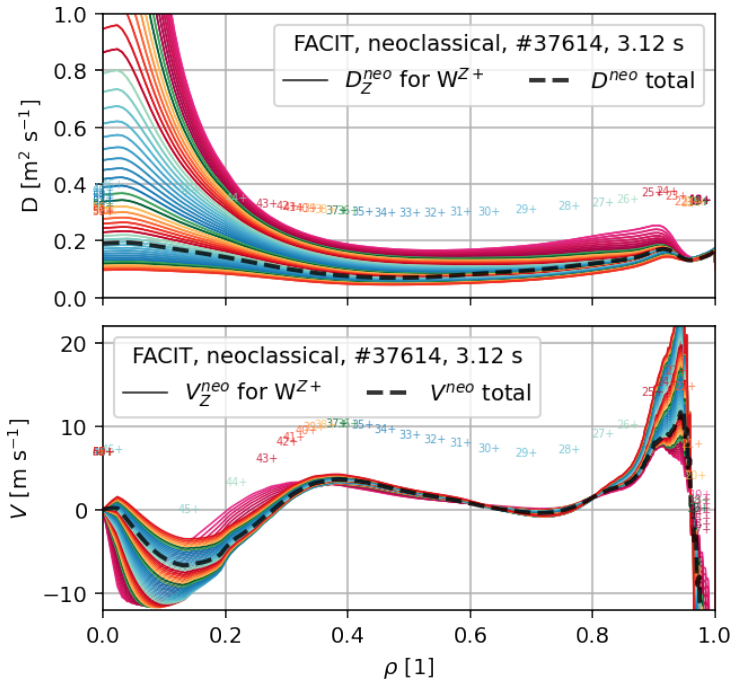

Figure 3.26: The neoclassical transport coefficients for the individual species D_Z^{neo} and V_Z^{neo} and the total D^{neo} and V^{neo} are calculated with FACIT based on the ionization equilibrium from Aurora.

Subsequently, anomalous transport due to turbulence in the plasma is added. The values of anomalous transport coefficients D^{an} and V^{an} were estimated by rescaling the output of the integrated tokamak modelling tool METIS. Original values are plotted separately in green in Fig. 3.27. The transport coefficient profile was slightly adjusted to shape the density profile. The original values for the pedestal have been kept. In the region from $\rho = 0.6$ to 0.95 the profile was flattened by its mean value. Up to $\rho = 0.6$ the original METIS values are again taken with an offset to ensure smoothness. Again, it is plotted in the graph in red. The total

transport coefficients were found by adding the neoclassical and modified anomalous coefficients $D^{neo}+D^{an}$ and $V^{neo}+V^{an}$. The resulting profiles are shown in Fig. 3.27. For comparison with the analytical formula for the Pfirsch-Schlüter regime, their ratios are also plotted. The model also describes the transport in SOL, where the coefficients $D^{SOL} = 0.8$ m^{2}s^{-1} and $V^{SOL} = 0$ ms^{-1} are chosen.

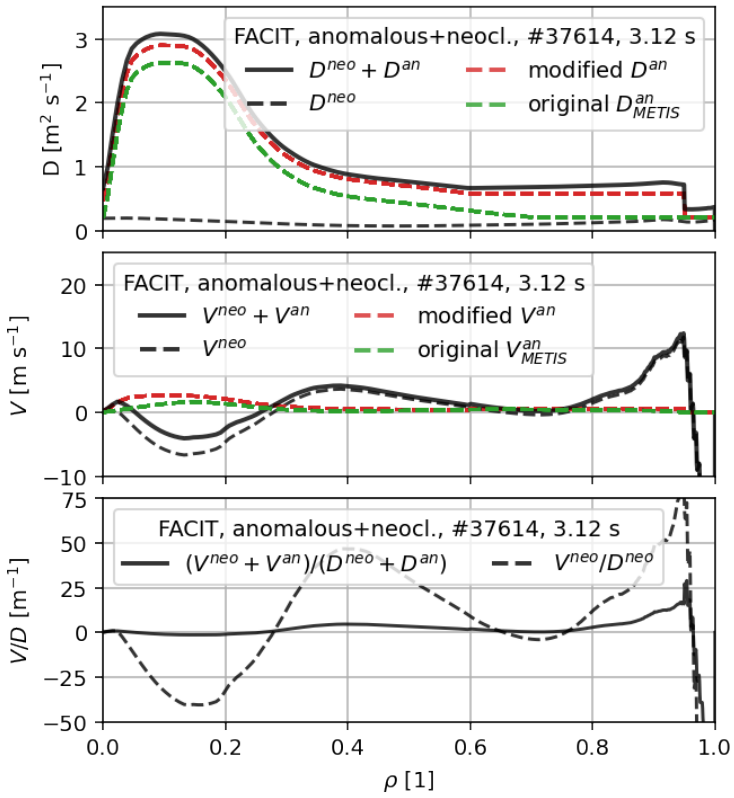

Figure 3.27: The anomalous transport coefficients D^{an} and V^{an} are estimated by rescaling the output of the integrated tokamak modelling tool METIS. This is then adjusted to shape the W density profile.

These are used as input to the Aurora transport model. The densities of each species are calculated in Fig. 3.28 for the scaling factor of the anomalous coefficients $\xi = 1$. The total density of tungsten n_W calculated with the code is compared at the same time with the density obtained from foil bolometry tomography and from soft X-ray cameras.

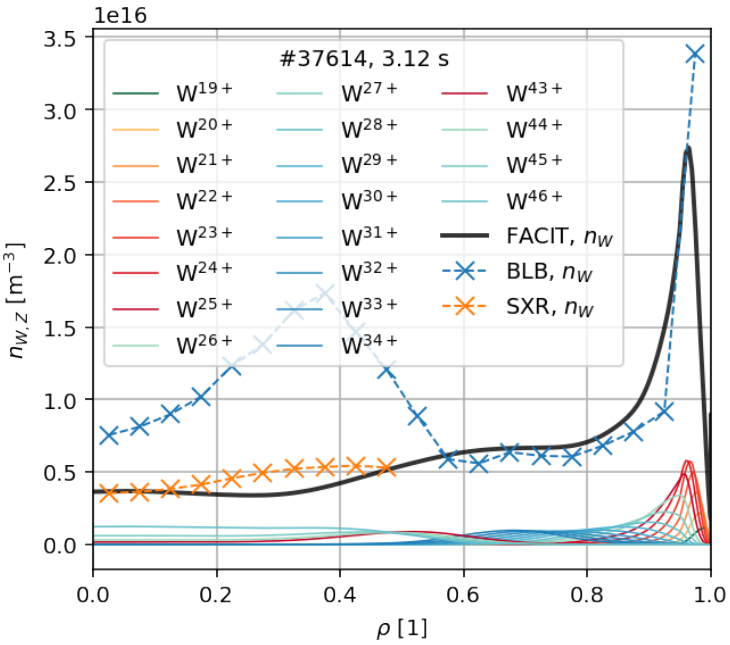

Figure 3.28: Tungsten density n_W and its individual charge states from the Aurora transport model and from tomography of the BLB and SXR diagnostics.

By adjusting the impurity source parameters and the anomalous transport scaling factor, a profile as close as possible to the one experimentally measured can be obtained. By changing the source rate, the entire resulting profile can be rescaled, although the pedestal is more sensitive to change than the centre. Adjusting the anomalous transport coefficients can make the profile more flat or, conversely, increase the peak in the pedestal. This is caused because of the inward flux due to the charge-dependent neoclassical transport in the pedestal. At the same time, there is an outward anomalous diffusion due to microinstabilities. Since the gradient is low in the central plasma, an outward neoclassical flux can occur. By varying the uniform parameters in the profile, it was not possible to achieve a hollow profile as measured by the foil bolometers BLB.

3.5 Summary

In Sect. 3.1, the 2D and 1D tungsten density profiles are calculated. This is done for foil bolometers, for soft X-ray cameras, and for AXUV diodes. A profile from the Johann spectrometer and the grazing incidence spectrometer data is also produced. A comparison of these profiles is made for different discharges and different time steps. In general, the W density is overestimated by foil bolometry. The quality of the results is strongly dependent on the quality of the tomographic reconstructions.

An analysis of the radiation asymmetry in the X-point region is performed in Sect. 3.2. The foil bolometry tomographic reconstruction is divided into regions according to the emissivity asymmetry. Two hypotheses are discussed. The first assumption assumes that all the emission asymmetry is due to the asymmetry of the electron density and temperature profile. The second hypothesis explains the asymmetry by the tungsten density asymmetry. A comparison with Vertical Thomson Scattering is made. Because of the application of the integrated data that

use VTA it is not possible to make a decision on the validity of the hypotheses.

In Sect. 3.3, an analysis of the transport of tungsten is provided. The transport coefficients are calculated from the steady state phase and subsequently from the laser blow-off experiment. Both methods are compared, and good agreement is found. The analysis is performed for foil bolometers and for soft X-ray cameras. The absolute magnitudes of the coefficients of the different diagnostics show good agreement.

The values of the transport coefficients are calculated from the neoclassical theory for the Pfirsch-Schlüter regime. The collisionality is calculated, and the tungsten is found to be in the plateau regime in most of the profile. The neoclassical coefficients are thus calculated from the FACIT submodule. The coefficients for anomalous transport are estimated with the output of the METIS code. The extracted coefficients are used for transport simulation in the Aurora package. By varying the impurity source parameters and scaling the anomalous transport, a density profile is found that matches the profile measured by tomography.

Conclusion

In this thesis, a new tool for data processing on the ASDEX Upgrade tokamak was created. Its aim is to obtain a 2D density profile of tungsten based on a plasma radiation model and computer tomography. The tool Tomotok [28] has been used to generate tomographic reconstructions from three different diagnostics. These include the foil bolometer BLB, the soft X-ray camera SXR and the fast AXUV diode XVR. The implementation of tomography from these diagnostics is discussed mainly in Sect. 2.2.

To obtain the density profile of tungsten, a model of high-temperature plasma emission is developed within the framework of the new tool. The modelled radiation is line emission and bremsstrahlung. Atomic data from different sources are compared and applied. In Sect. 2.1 the difference between the PEC40 and PEC50 datasets is discussed. The procedure for obtaining the cooling factors, which are essential for evaluating the tungsten concentration, is described in detail.

The developed tool allows to find the 2D tungsten density profile in total from three diagnostics. This is demonstrated in Sect. 3.1. The above-mentioned plasma radiation model is used to calculate the cooling factor filtered by the spectral response of a given diagnostic. The possible applications of different diagnostics and their advantages are also discussed in this section. In Sect. 3.2 the anisotropy in the plasma emissivity is discussed, similar to Ref. [42].

The developed tool is applied to discharges from the ASDEX Upgrade tokamak performed within MST1-Topic 10/WPTE-RT03. The analysis in this work focusses on the processing of data from laser blow-off experiments. In other words, the experimental part of this work deals with tungsten transport.

In total, three successful LBOs are selected from the available discharges. In Sect. 3.3 the method by which the transport coefficients are found is described and applied. Under certain assumptions, the steady-state phase before the LBO is analysed. Subsequently, the coefficients from the exponential decay of the LBO are also found. A comparison between these methods is made and good agreement across the profile is found.

In the last Sect. 3.4 a new Aurora Python package is implemented that allows to handle impurity transport. Using the FACIT submodule, neoclassical transport coefficients are found. The coefficients for anomalous transport are estimated with the output of the METIS code. The transport coefficients found are used as input to Aurora. By varying the impurity source parameters and scaling the anomalous transport, a density profile is found that matches the profile measured by tomography as shown in Fig. 3.27.

There are large discrepancies between the coefficients theoretically derived and experimentally measured D and V. In both methods, the values of the convective velocity V are found to be of the same order of magnitude. It appears that for

the bolometers in Fig. 3.21 the trend in the central plasma is exactly the opposite. For the pedestal region, the values of V for both cases increase as expected. In contrast, the results from the soft X-ray cameras in Fig. 3.23 show a consistent trend throughout the profile. For the diffusion coefficient D, the values found in the experiment are almost an order of magnitude lower than those from the theoretical model. In some cases, negative values of D are found from the foil bolometer data in the centre of the plasma, which is not easily explainable.

A next step in the analysis of these data could be to integrate some edge plasma diagnostics. Since there are high gradients in the pedestal, there is a large convective term. This, in fact, can be seen from the measurements in this thesis. It is also possible to extend the LBO analysis to other discharges and thus make comparisons for different heating or scenarios, for example. One also unrealized possibility is to select different regions of the 2D profile and evaluate the transport in them.

In Sect. 2.1 a model of plasma emission was presented. The difference between the PEC40 and PEC50 data and other references was discussed. Finally, the PEC40 data from Open ADAS was adopted for the calculation of the cooling factor. Simultaneously, the radiation via bremsstrahlung was added to the cooling factor. A component of radiation not discussed further in this thesis is recombination radiation. This can also be modelled as discussed in Sect. 1.4. The motivation for this should be that up to temperature ≈ 5 keV dielectronic recombination is the second largest source of radiation.

As mentioned in Sect. 1.3, the calculation of the ionisation balance neglects the flux of a given population by diffusion and convection. This may not be a correct assumption, and it is convenient to include this effect into the equilibrium. A future solution may be to utilise the Aurora package to calculate the ionisation equilibrium.

It turns out that the quality of tomographic reconstructions has a very important influence on subsequent processing. For example, the tomotok package repeatedly fails to correctly evaluate the radiation from the X-point vicinity. Quite a lot of effort is required to produce a decent reconstruction. One of the causes is the choice of the algorithm. In Tomotok, the Minimum Fisher regularisation algorithm is implemented, which is more suitable for reconstructing data from soft X-rays. The high emissivity differences between the X-point radiator and the bulk plasma cause large errors in the core plasma reconstruction. Since the absolute error is equally large for both regions, it fails to reconstruct the centre properly. These difficulties are typical for foil bolometers, which are, moreover, particularly sensitive to the edge-localised mode.

One solution to improve the quality of tomography in the future is to use a geometric matrix generated by ray tracing. The single-line approximation is particularly sensitive in the vicinity of the wall, which affects the result in the divertor area. The ray-tracing matrix more reliably reconstructs gradients and more complex structures.

Another solution on the AUG tokamak might be to use the pyTomo [29] tool. It includes a much larger variety of algorithms that are more or less suitable for reconstructing bolometric cameras. Alternatives and improvements are discussed in Sect. 1.6.

AXUV diodes can be used to analyse fast phenomena on tokamaks. Due to the scope of the thesis and the low priority, the diodes were not calibrated in this work. In the future, such calibration can be done using absolutely calibrated foil bolometers. One possibility could be to calibrate individual channels by adjacent

ones.

In this thesis, the idea of combining different diagnostics has not yet been exhausted. In addition to foil bolometers and soft X-ray cameras, AXUV diodes can be calibrated. One of the challenges to continue working on is the combination of the three diagnostics to create a single tungsten density profile. Bayesian probability theory could be used to develop such integrated diagnostics. However, an extended knowledge of the individual diagnostics including its uncertainty will be necessary to extract as much information as possible.

Bibliography

1. PÜTTERICH, T.; FABLE, E.; DUX, R.; O'MULLANE, M.; NEU, R.; SICCINIO, M. Determination of the tolerable impurity concentrations in a fusion reactor using a consistent set of cooling factors. *Nuclear Fusion*. 2019, vol. 59, no. 5, p. 056013. Available from DOI: 10.1088/1741-4326/ab0384.
2. ATZENI, S.; MEYER-TER-VEHN, J. *The Physics of Inertial Fusion: Beam Plasma Interaction, Hydrodynamics, Hot Dense Matter*. 1st ed. Clarendon Press, 2004. ISBN 0-19-856264-0.
3. FREIDBERG, J. P. *Plasma physics and fusion energy*. Cambridge University Press, 2007. ISBN 978-0-521-85107-7.
4. KIKUCHI, M.; LACKNER, K.; TRAN, M. Q. *Fusion physics*. International Atomic Energy Agency, 2012. ISBN 978–92–0–130410–0.
5. DOLAN, T. J. *Fusion research: Principles, experiments and Technology*. Pergamon Press, 1982. ISBN 0-08-025565-5.
6. WESSON, J.; CAMPBELL, D.J. *Tokamaks*. Amsterdam, Netherlands: Amsterdam University Press, 2004. ISBN 0-19-8509227.
7. MIYAMOTO, K. *Fundamentals of plasma physics and Controlled Fusion*. National Institute of Fusion Science, 2000. ISBN 4-900491-11.
8. WANG, H.; BARTON, J. E.; SCHUSTER, E. Poloidal Flux Profile Reconstruction from pointwise measurements via extended Kalman filtering in the DIII-D tokamak. *2015 IEEE Conference on Control Applications (CCA)*. 2015. Available from DOI: 10.1109/cca.2015.7320793.
9. BOOZER, A. H. Physics of magnetically confined plasmas. *Reviews of Modern Physics*. 2005, vol. 76, no. 4, pp. 1071–1141. Available from DOI: 10.1103/revmodphys.76.1071.
10. JAULMES, F.F.E. *Kinetic behaviour of ions in tokamak inductive scenarios*. 2016. PhD thesis. Technische Universiteit Eindhoven.
11. KUNZE, H. J. *Introduction to plasma spectroscopy*. Springer Berlin, 2013. ISBN 978-3-642-02232-6.
12. HUTCHINSON, I. H. *Principles of Plasma Diagnostics*. 2nd ed. Cambridge University Press, 2002. Available from DOI: 10.1017/CBO9780511613630.
13. SUMMERS, H. P. The ADAS User Manual, version 2.6. 2004. Available also from: http://www.adas.ac.uk.
14. FOSTER, A. *On the behaviour and radiating properties of heavy elements in Fusion Plasmas*. 2008. PhD thesis. University of Strathclyde.

15. JARDIN, A.; MAZON, D.; MALARD, P.; O'MULLANE, M.; CHERNYSHOVA, M.; CZARSKI, T.; MALINOWSKI, K.; KASPROWICZ, G.; WOJENSKI, A.; POZNIAK, K. On a gas electron multiplier based synthetic diagnostic for soft X-ray tomography on West with focus on impurity transport studies. *Journal of Instrumentation*. 2017, vol. 12, no. 08. Available from DOI: 10.1088/1748-0221/12/08/c08013.

16. PÜTTERICH, T.; NEU, R.; DUX, R.; WHITEFORD, A. D.; O'MULLANE, M. G. Modelling of measured tungsten spectra from ASDEX Upgrade and predictions for Iter. *Plasma Physics and Controlled Fusion*. 2008, vol. 50, no. 8, p. 085016. Available from DOI: 10.1088/0741-3335/50/8/085016.

17. AVILLEZ, M. A. de; BREITSCHWERDT, D. Temperature-averaged and total free-free gaunt factors for and Maxwellian distributions of electrons (Corrigendum). *Astronomy amp; Astrophysics*. 2015/2018, vol. 580. Available from DOI: 10.1051/0004-6361/201526104.

18. PÜTTERICH, T.; NEU, R.; DUX, R.; WHITEFORD, A.D.; O'MULLANE, M.G.; SUMMERS, H.P. Calculation and experimental test of the cooling factor of tungsten. *Nuclear Fusion*. 2010, vol. 50, no. 2, p. 025012. Available from DOI: 10.1088/0029-5515/50/2/025012.

19. POST, D.E.; JENSEN, R.V.; TARTER, C.B.; GRASBERGER, W.H.; LOKKE, W.A. Steady-state radiative cooling rates for low-density, high-temperature plasmas. *Atomic Data and Nuclear Data Tables*. 1977, vol. 20, no. 5, pp. 397–439. Available from DOI: 10.1016/0092-640x(77)90026-2.

20. BERNERT, M.; EICH, T.; BURCKHART, A.; FUCHS, J. C.; GIANNONE, L.; KALLENBACH, A.; MCDERMOTT, R. M.; SIEGLIN, B. Application of AXUV diode detectors at ASDEX upgrade. *Review of Scientific Instruments*. 2014, vol. 85, no. 3. Available from DOI: 10.1063/1.4867662.

21. MEISTER, H.; WILLMEROTH, M.; ZHANG, D.; GOTTWALD, A.; KRUMREY, M.; SCHOLZE, F. Broad-band efficiency calibration of ITER bolometer prototypes using PT absorbers on Sin Membranes. *Review of Scientific Instruments*. 2013, vol. 84, no. 12. Available from DOI: 10.1063/1.4834755.

22. LANG, P. T.; MAST, K. F. Photoresponse of a miniaturized ultrabroad-band low-noise metal-film Bolometer Detector array. *Journal of Optics*. 1996, vol. 27, no. 1, pp. 25–29. Available from DOI: 10.1088/0150-536x/27/1/004.

23. SHEIKH, U. A.; SIMONS, L.; DUVAL, B. P.; FÉVRIER, O.; MORET, D.; ALLEGRUCCI, A.; BERNERT, M.; CRISINEL, F.; TERSZTYÁNSZKY, T.; VILLINGER, O. RADCAM—a radiation camera system combining foil bolometers, AXUV diodes, and filtered soft X-ray diodes. *Review of Scientific Instruments*. 2022, vol. 93, no. 11. Available from DOI: 10.1063/5.0095907.

24. IGOCHINE, V.; GUDE, A.; MARASCHEK, M. Hotlink based Soft X-ray Diagnostic on ASDEX Upgrade. *IPP internal report*. 2010.

25. ANTON, M.; WEISEN, H.; DUTCH, M. J.; LINDEN. X-ray tomography on the TCV Tokamak. *Plasma Physics and Controlled Fusion*. 1996, vol. 38, no. 11, pp. 1849–1878. Available from DOI: 10.1088/0741-3335/38/11/001.

26. MLYNÁŘ, J.; CRACIUNESCU, T.; FERREIRA, D. R. Current Research into Applications of Tomography for Fusion Diagnostics. *Journal of Fusion Energy*. 2019, vol. 38, pp. 458–466. Available from DOI: https://doi.org/10.1007/s10894-018-0178-x.

27. INGESSON, L. C.; ALPER, B.; PETERSON, B. J.; VALLET, J.-C. Chapter 7: Tomography Diagnostics: Bolometry and Soft-X-Ray Detection. *Fusion Science and Technology*. 2008, vol. 53, no. 2, pp. 528–576. Available from DOI: 10.13182/FST53-528.

28. SVOBODA, J.; CAVALIER, J.; FICKER, O.; IMRÍŠEK, M.; MLYNÁŘ, J.; HRON, M. Tomotok: python package for tomography of tokamak plasma radiation. *Journal of Instrumentation*. 2021, vol. 16, no. 12, p. C12015. Available from DOI: 10.1088/1748-0221/16/12/C12015.

29. ODSTRČIL, T.; PÜTTERICH, T.; ODSTRČIL, M.; GUDE, A.; IGOCHINE, V.; STROTH, U. Optimized tomography methods for plasma emissivity reconstruction at the ASDEX upgrade Tokamak. *Review of Scientific Instruments*. 2016, vol. 87, no. 12. Available from DOI: 10.1063/1.4971367.

30. CARR, M.; MEAKINS, A.; BERNERT, M.; DAVID, P.; GIROUD, C.; HARRISON, J.; HENDERSON, S.; LIPSCHULTZ, B.; REIMOLD, F. Description of complex viewing geometries of fusion tomography diagnostics by Ray-Tracing. *Review of Scientific Instruments*. 2018, vol. 89, no. 8. Available from DOI: 10.1063/1.5031087.

31. DAVID, P.; BERNERT, M.; PÜTTERICH, T.; FUCHS, C.; GLÖGGLER, S.; EICH, T.; ASDEX UPGRADE TEAM, the. Optimization of the computation of total and local radiated power at ASDEX upgrade. *Nuclear Fusion*. 2021, vol. 61, no. 6, p. 066025. Available from DOI: 10.1088/1741-4326/abf2e1.

32. DUX, R. STRAHL User Manual (IPP 10/30). *Garching: Max-Planck-Institut für Plasmaphysik, IPP report*. 2006. Available also from: https://hdl.handle.net/11858/00-001M-0000-0027-0DB8-4.

33. FITZPATRICK, R. *Plasma physics: An introduction*. CRC Press, 2022. ISBN 9781032202518.

34. HUBA, J. D. *NRL Plasma Formulary*. 2013. Available from DOI: 10.21236/ada469421.

35. FAJARDO, D.; ANGIONI, C.; MAGET, P.; MANAS, P. Analytical model for collisional impurity transport in Tokamaks at arbitrary collisionality. *Plasma Physics and Controlled Fusion*. 2022, vol. 64, no. 5, p. 055017. Available from DOI: 10.1088/1361-6587/ac5b4d.

36. WADE, M. R.; HOULBERG, W. A.; BAYLOR, L. R. Experimental confirmation of impurity convection driven by the ion-temperature gradient in toroidal plasmas. *Physical Review Letters*. 2000, vol. 84, no. 2, pp. 282–285. Available from DOI: 10.1103/physrevlett.84.282.

37. ODSTRČIL, T.; HOWARD, N. T.; SCIORTINO, F.; CHRYSTAL, C.; HOLLAND, C.; HOLLMANN, E.; MCKEE, G.; THOME, K. E.; WILKS, T. M. Dependence of the impurity transport on the dominant turbulent regime in elm-y h-mode discharges on the DIII-D tokamak. *Physics of Plasmas*. 2020, vol. 27, no. 8. Available from DOI: 10.1063/5.0010725.

38. ODSTRČIL, T. *On the Origin, Properties, and Implications of Asymmetries in the Tungsten Impurity Density in Tokamak Plasmas*. 2017. PhD thesis. Technischen Universität München.

39. LUNT, T.; FENG, Y.; KRIEGER, K.; KALLENBACH, A.; NEU, R.; JANZER, A.; DUX, R.; COSTER, D.P.; WISCHMEIER, M.; HICKS, N.; AL., et. 3D modeling of the ASDEX upgrade edge plasma exposed to a localized tungsten source by means of emc3-eirene. *Journal of Nuclear Materials*. 2011, vol. 415, no. 1. Available from DOI: 10.1016/j.jnucmat.2010.11.009.

40. CHUNG, H.-K.; CHEN, M.H.; MORGAN, W.L.; RALCHENKO, Y.; LEE, R.W. FLYCHK: Generalized population kinetics and spectral model for rapid spectroscopic analysis for all elements. *High Energy Density Physics*. 2005, vol. 1, no. 1, pp. 3–12. Available from DOI: 10.1016/j.hedp.2005.07.001.

41. SUMMERS, H. P.; O'MULLANE, M. G. Atomic data and modelling for Fusion: The adas project. *AIP Conference Proceedings*. 2011. Available from DOI: 10.1063/1.3585817.

42. FAJARDO, D.; ANGIONI, C.; DUX, R.; FABLE, E.; PLANK, U.; SAMOYLOV, O.; TARDINI, G. Full-radius integrated modelling of ASDEX upgrade L-modes including impurity transport and radiation. *Nuclear Fusion*. 2024, vol. 64, no. 4, p. 046021. Available from DOI: 10.1088/1741-4326/ad29bd.

43. MAGET, P.; MANAS, P.; FRANK, J.; NICOLAS, T.; AGULLO, O.; GARBET, X. Corrigendum: An Analytic model for the collisional transport and poloidal asymmetry distribution of impurities in tokamak plasmas (2020 plasma phys. control. fusion 62 105001). *Plasma Physics and Controlled Fusion*. 2022, vol. 64, no. 6, p. 069501. Available from DOI: 10.1088/1361-6587/ac63e0.

44. FAJARDO, D; ANGIONI, C; CASSON, F J; FIELD, A R; MAGET, P; MANAS, P. Analytical model for the combined effects of rotation and collisionality on neoclassical impurity transport. *Plasma Physics and Controlled Fusion*. 2023, vol. 65, no. 3, p. 035021. Available from DOI: 10.1088/1361-6587/acb0fc.

Appendix

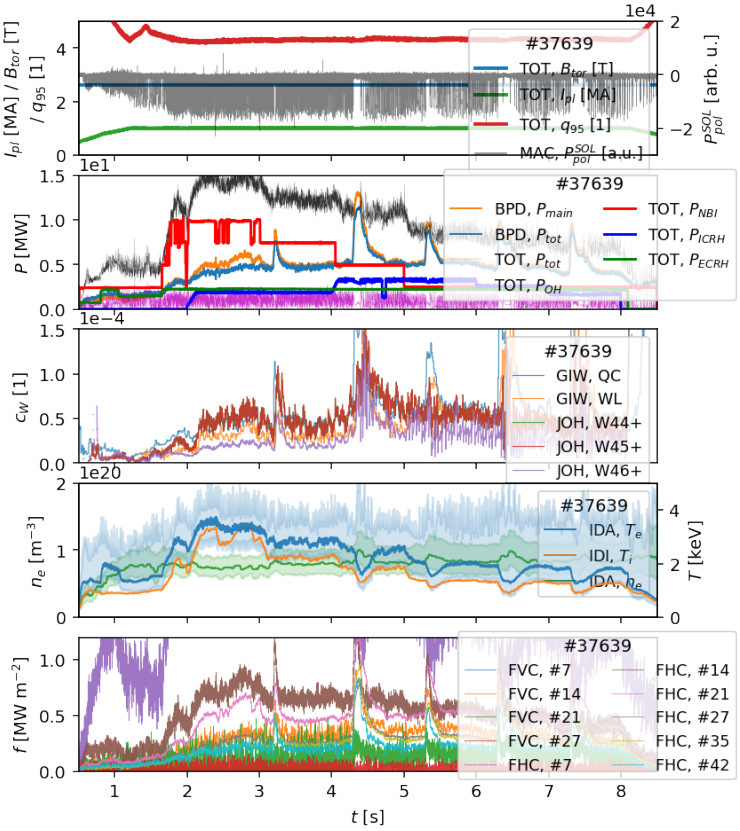

Figure 29: Overview of the discharge #37639. (a) toroidal magnetic field B_{tor}, plasma current I_{pl}, safety factor q_{95} and signal from RT diagnostics for halo current measurements P_{pol}^{SOL}. (b) total radiated power P_{tot} from BPB, radiated power P_{main} in main plasma from BPD, ECRH, NBI, ICRH and Ohmic power including total plasma power from TOT. (c) Tungsten concentration from Johann spectrometer JOW from single line diagnostics and the grazing incidence spectrometer GIW from quasicontinuum QC and line emission. (d) Electron temperature T_e and density n_e from IDA integrated data analysis and ion profile T_i from IDI. (e) Selected channels from foil bolometers of vertical camera FVC and horizontal camera FHC.

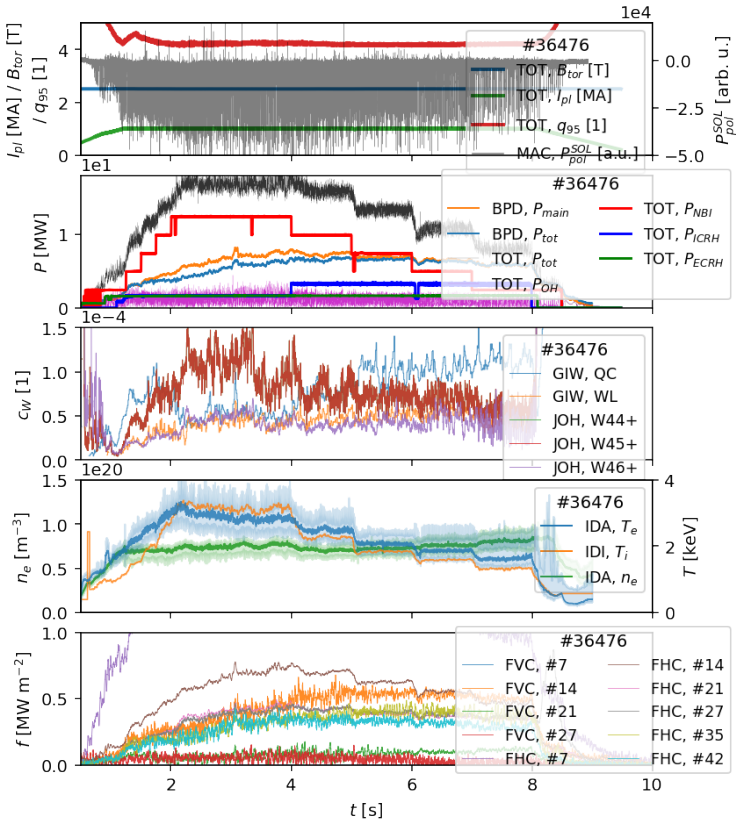

Figure 30: Overview of the discharge #36476. (a) toroidal magnetic field B_{tor}, plasma current I_{pl}, safety factor q_{95} and signal from RT diagnostics for halo current measurements P_{pol}^{SOL}. (b) total radiated power P_{tot} from BPB, radiated power P_{main} in main plasma from BPD, ECRH, NBI, ICRH and Ohmic power including total plasma power from TOT. (c) Tungsten concentration from Johann spectrometer JOW from single line diagnostics and the grazing incidence spectrometer GIW from quasicontinuum QC and line emission. (d) Electron temperature T_e and density n_e from IDA integrated data analysis and ion profile T_i from IDI. (e) Selected channels from foil bolometers of vertical camera FVC and horizontal camera FHC.

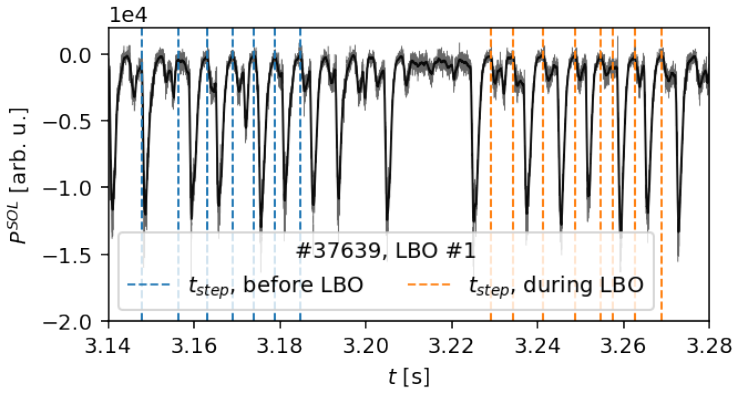

Figure 39: The time steps for the LBO analysis are chosen so that the density profile is not affected by the edge-localized mode. The ELM detection is done from RT diagnostics for halo current measurements P_{pol}^{SOL}.

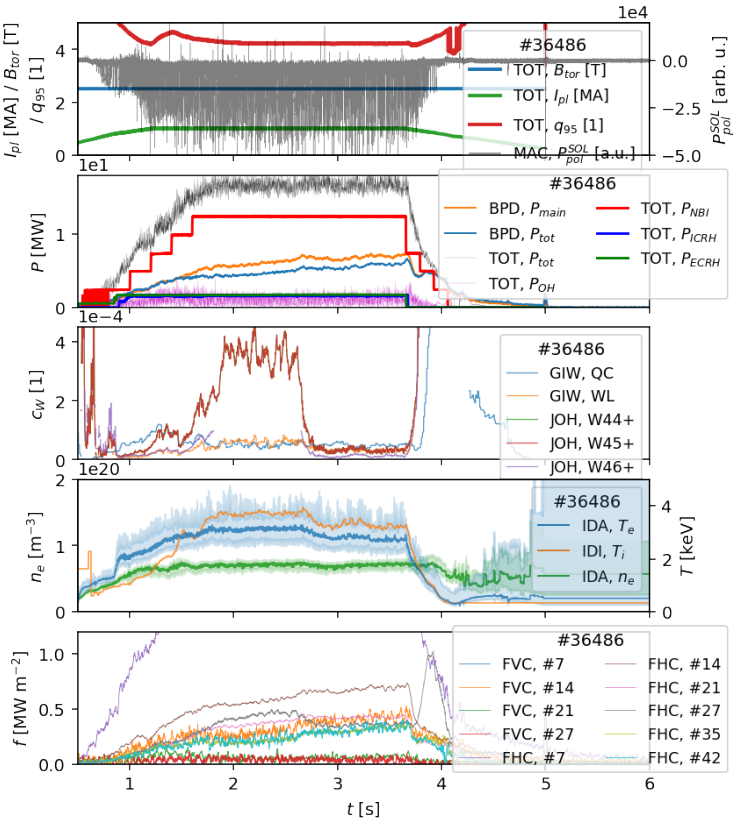

Figure 31: Overview of the discharge #36486. (a) toroidal magnetic field B_{tor}, plasma current I_{pl}, safety factor q_{95} and signal from RT diagnostics for halo current measurements P_{pol}^{SOL}. (b) total radiated power P_{tot} from BPB, radiated power P_{main} in main plasma from BPD, ECRH, NBI, ICRH and Ohmic power including total plasma power from TOT. (c) Tungsten concentration from Johann spectrometer JOW from single line diagnostics and the grazing incidence spectrometer GIW from quasicontinuum QC and line emission. (d) Electron temperature T_e and density n_e from IDA integrated data analysis and ion profile T_i from IDI. (e) Selected channels from foil bolometers of vertical camera FVC and horizontal camera FHC.

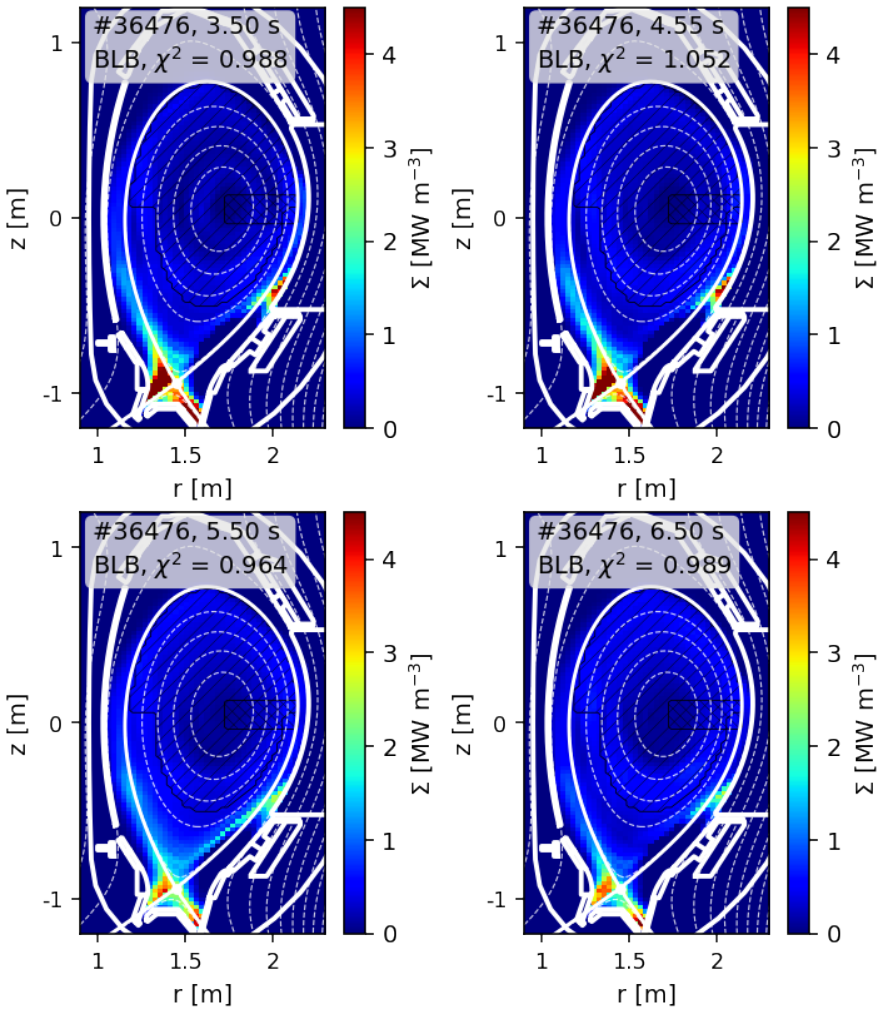

Figure 32: Selected tomographic reconstructions from the BLB bolometric cameras for different time steps of discharge #36476. The resulting tungsten density profiles are shown in Fig. 34.

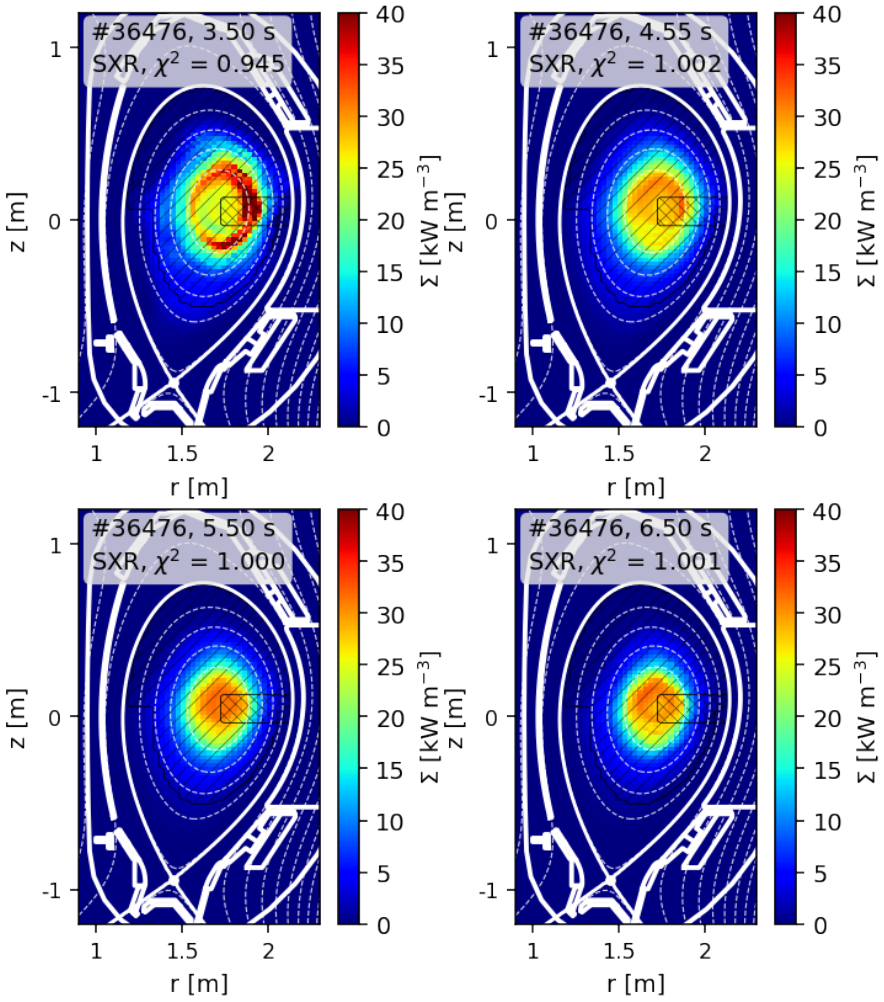

Figure 33: Selected tomographic reconstructions from the SXR cameras for different time steps of discharge #36476. The resulting tungsten density profiles are shown in Fig. 34.

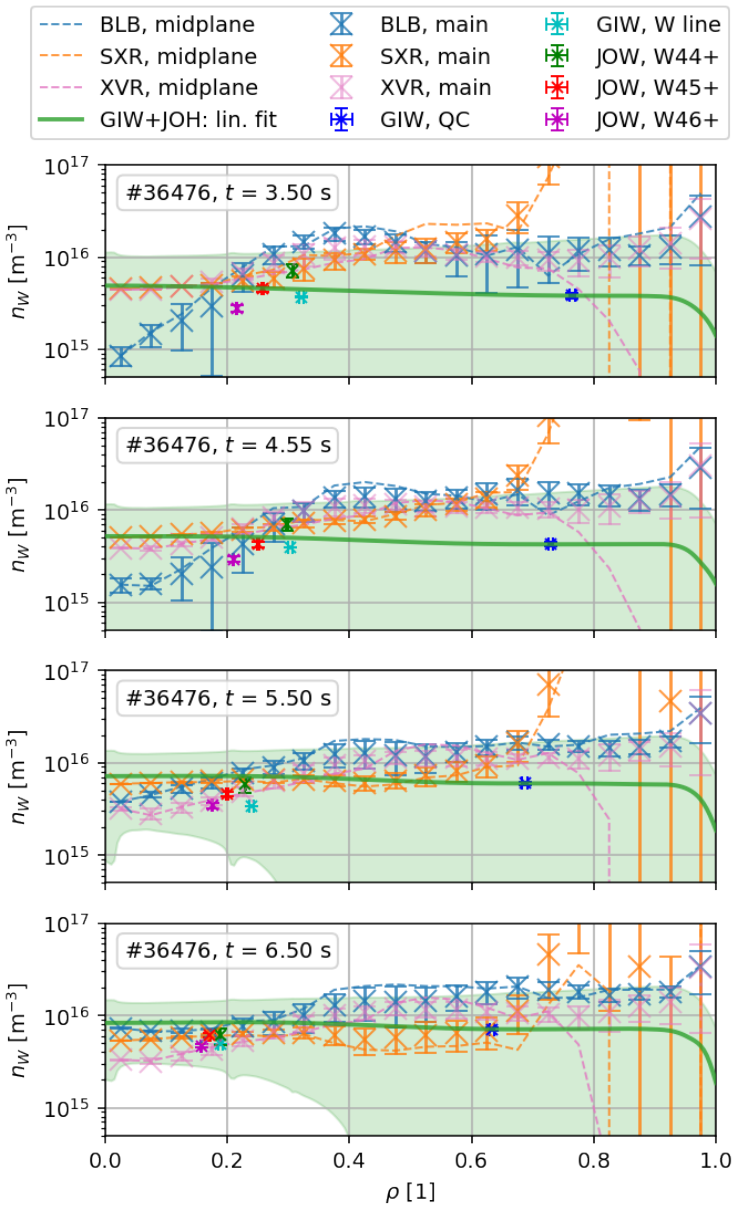

Figure 34: Tungsten density profile obtained from three different diagnostics: foil bolometers BLB, AXUV diodes XVR and SXR cameras. For different time steps of the discharge #36476, the profiles are calculated from the main and midplane regions shown in Fig. 32 and 33. A comparison is made with the results of the JOW and GIW diagnostics.

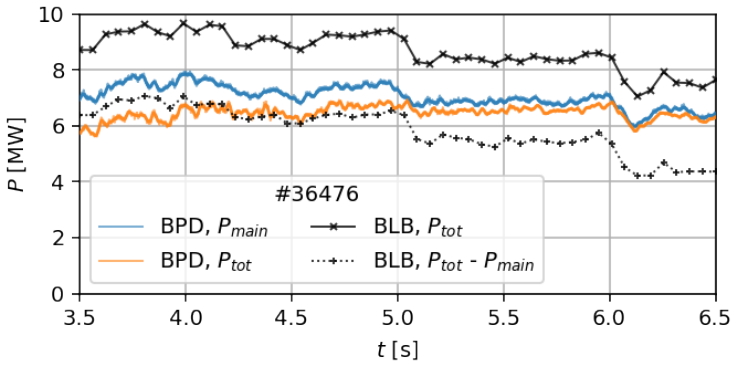

Figure 35: Total radiated power determined from tomography of bolometric cameras for different timesteps of the discharge #36476 compared with BPD diagnostics.

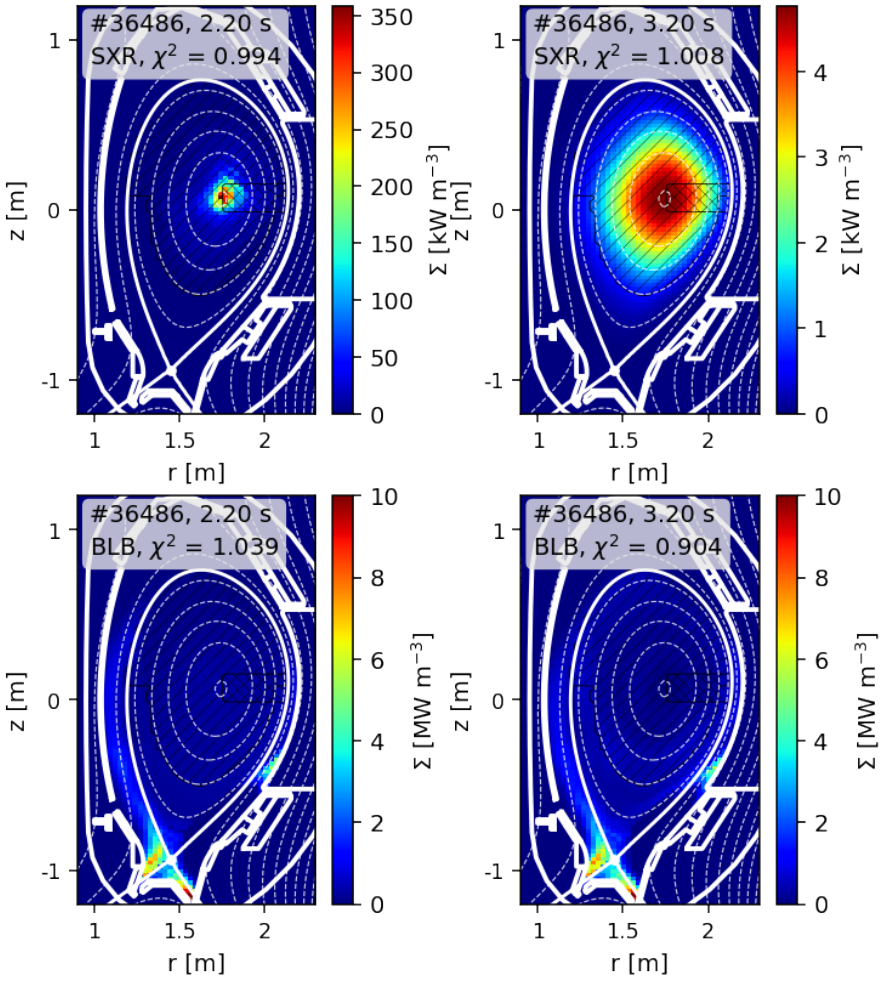

Figure 36: Selected tomographic reconstructions from the BLB bolometric cameras for different time steps of discharge #36486. The resulting tungsten density profiles are shown in Fig. 37.

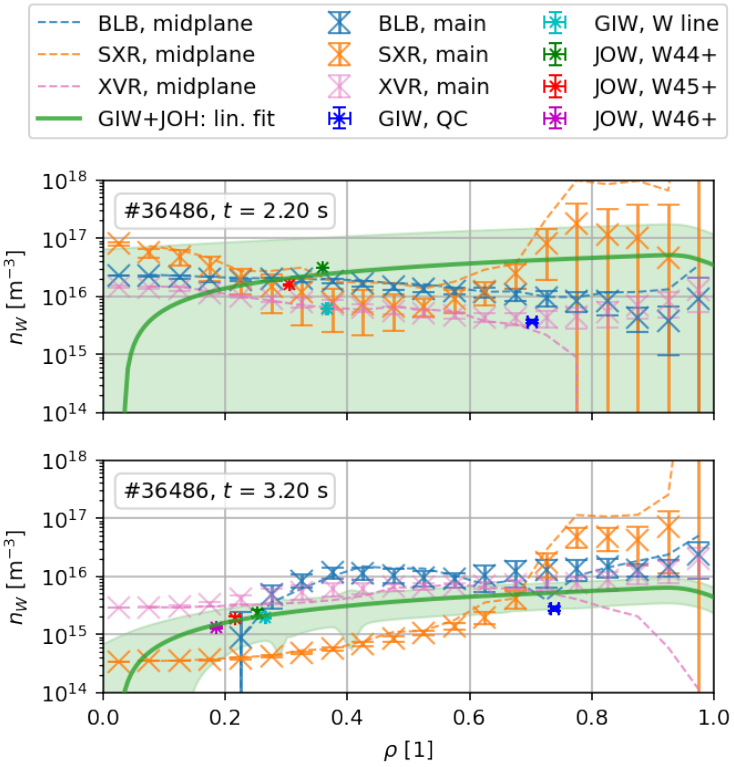

Figure 37: Tungsten density profile obtained from three different diagnostics: foil bolometers BLB, AXUV diodes XVR and SXR cameras. For different time steps of the discharge #36486, the profiles are calculated from the main and midplane regions shown in Fig. 36. A comparison is made with the results of the JOW and GIW diagnostics.

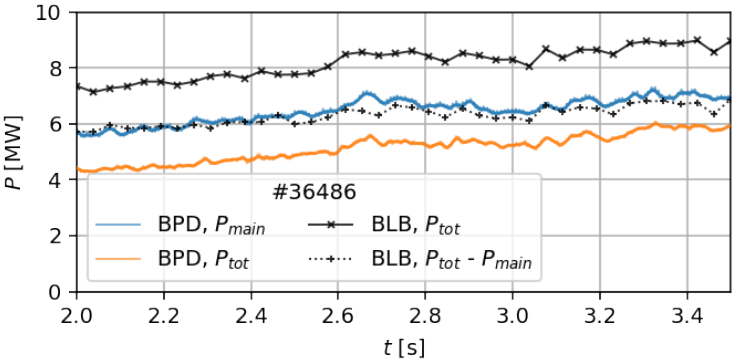

Figure 38: Total radiated power determined from tomography of bolometric cameras for different timesteps of the discharge #36486 compared with BPD diagnostics.

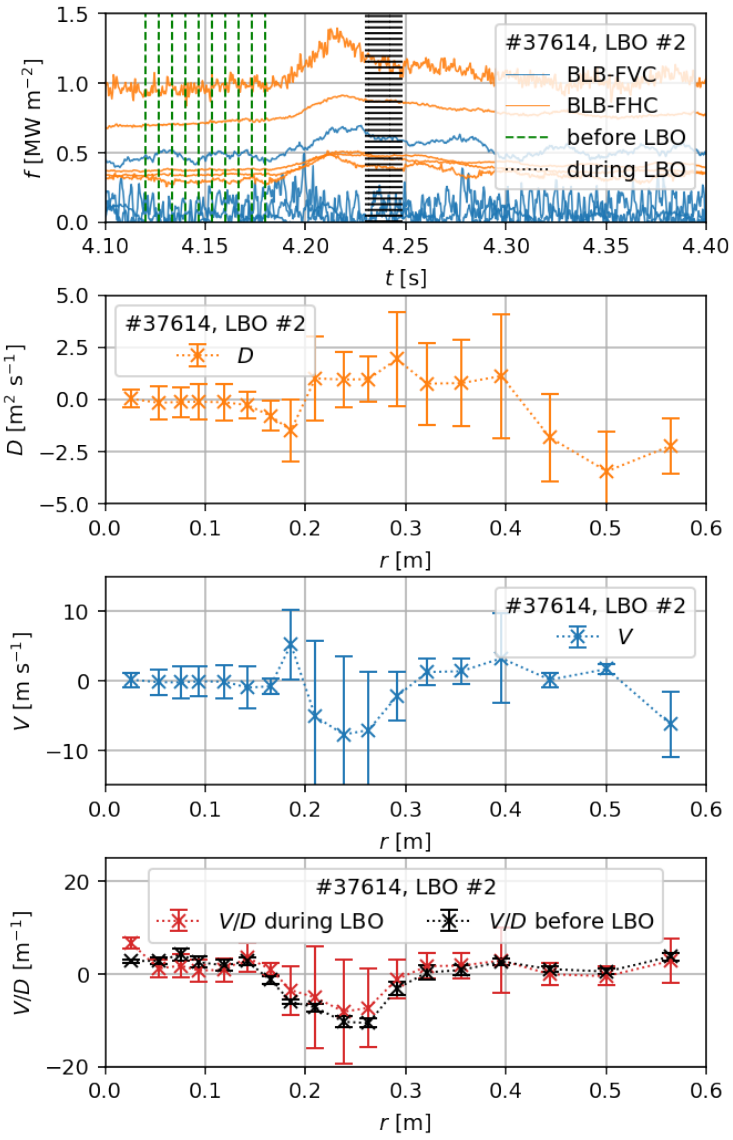

Figure 40: The diffusion coefficient D and drift velocity V obtained from the analysis during second LBO of the discharge #37614. A comparison is made with the steady-state pre-LBO transport analysis using the V/D ratio.

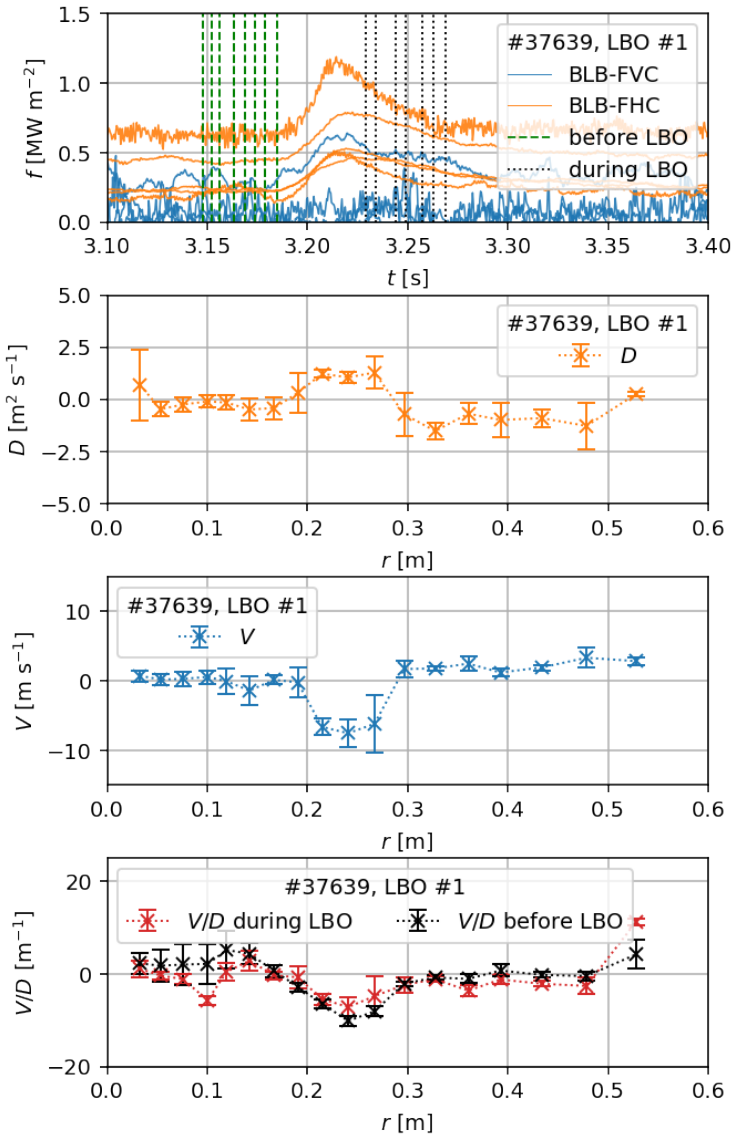

Figure 41: The diffusion coefficient D and drift velocity V obtained from the analysis during LBO of the discharge #37639. A comparison is made with the steady-state pre-LBO transport analysis using the V/D ratio.